Alma Mater Studiorum
Università di Bologna

Dipartimento di Fisica e Astronomia

Corso di Laurea Magistrale in Astrofisica e Cosmologia

Properties of the galactic-scale gas circulation generated by stellar feedback

Candidato:
Daniele Giarrusso

Relatore:
Dott. Federico Marinacci

Sessione I

Anno accademico 2019-2020

Contents

Abstract

The properties that characterize the gas cycle in galactic systems similar to the Milky Way include a multitude of processes and physical phenomena that are not completely understood. The interaction between the multi-phase gas components of the galactic disc and the gaseous material in the halo surrounding the galaxy appears to play key role supporting star formation in these structures throughout their whole lifetime. Indeed, observations confirm the idea that this class of galaxies has been able to form stars at a more or less constant rate ($\sim 2\,\mathrm{M_\odot\,yr^{-1}}$) for almost their entire life time. Generally speaking, the formation and evolution of galaxies is dictated by the environment surrounding them and by the various feedback channels (stellar, radiative, etc.) that have operated over time within these cosmic systems, contributing to or hindering the process of star formation. Numerical simulations can be used to construct galaxy models that allow us to test the different feedback processes that contribute to the expulsion or acquisition of gas, giving rise for instance to phenomena of galactic fountain or gas growth by the disk.

In this thesis work we analyzed *closed-box* simulation of an isolated galaxy similar to the Milky Way, placed inside a dark matter halo in the absence of a cosmological context and a hot gas atmosphere (the so-called galactic corona) surrounding it. In particular, we have focused on one of the main causes of the generation of gas ejection phenomena from the disc plane, which is also the supporting mechanism in the structuring of the gas in its different multiphase components, i.e. stellar feedback largely due to supernova explosions. The purpose of the thesis is to test the validity of the results obtained from this simulation (run with the recent stellar feedback model *SMUGGLE* implemented in the moving-mesh code *AREPO*), from the point of view of star formation, supernova events and gas expulsion/accretion phenomena during the time span of $\sim$ 1 Gyr. As a result of our study we have derived different evolutionary trends of the kinematic

properties of gas, the SF process and the efficiency of energy/momentum release by SN explosions, in order to look for possible relationships that would highlight the close connection between all these astrophysical processes.

The results obtained show that the simulation, from the point of view of the gas kinematics in its vertical motion with respect to the disc plane, was able to generate gas expulsion/accretion phenomena in a self-consistent way. This, also in combination with the gradual depletion of gas due to stellar formation, has led the galaxy to adjust its SF at a rate of $SFR \sim 2\,\mathrm{M}_\odot\,\mathrm{yr}^{-1}$ and a rate of supernova-type-II explosions of $SNR \sim 2$ events per century, according to current observational estimates for galaxies similar to the Milky Way. Further confirmation of the goodness of the model, with which the evolution of the galaxy was simulated, was obtained thanks to the fact that the simulation was able to reproduce the Kennicutt-Schmidt relation deduced from the observations. Finally, this thesis work investigated a possible connection between the variation of the star formation rate surface density and the amount of expelled gas mass from the disc contained within a certain height from the galactic plane as a function of time. This has been done in order to evaluate the existence of a possible critical value for Σ_{SFR} above which we can clearly identify phenomena of gas ejection on a galactic scale. The results obtained do not show evidence of the existence of such value. However, a more in depth analysis and further comparison to simulations and observations are necessary to corroborate these preliminary results.

Sommario

Le proprietà che caratterizzano il ciclo del gas nei sistemi galattici simili alla Via Lattea comprendono una moltitudine di processi e fenomeni fisici ancora ampiamente non ben compresi. L'interazione tra le componenti multifase del gas costituenti il disco galattico e il materiale gassoso nell'alone circondante la galassia sembrano essere elementi chiave a sostegno di una persistente formazione stellare dall'origine di queste strutture sino ad oggi. Le osservazioni confermano l'idea che questa classe di galassie sia stata in grado di formare stelle ad un ritmo più o meno costante ($\sim 2\,\mathrm{M}_\odot\,\mathrm{yr}^{-1}$) per quasi tutto il loro arco vitale. Più in generale, la formazione ed evoluzione delle galassie è dettata dall'ambiente che le circonda e dai vari canali di feedback (stellare, radiativo, ecc.) che nel tempo si sono susseguiti all'interno di questi sistemi cosmici contribuendo o ostacolando il processo di formazione stellare. Le simulazioni numeriche possono essere utilizzate per costruire modelli di galassie al fine di testare i differenti processi di feedback che concorrono all'espulsione o acquisizione di gas, dando origine ad esempio a fenomeni di fontana galattica o di accrescimento di gas da parte del disco.

In questo lavoro di tesi ci siamo occupati di analizzare una simulazione *closed-box* di una galassia isolata simile alla Via Lattea, posta all'interno di un alone di materia oscura in assenza di contesto cosmologico e di una atmosfera di gas caldo (la cosidetta corona galattica) che la circondasse. In particolare, ci siamo soffermati ad analizzare una delle principali cause della generazione di fenomeni di esplulsione di gas dal piano del disco, nonché meccanismo portante nella strutturazione del gas nelle sue diverse componenti multifase, ossia il feedback stellare dovuto in larga parte alle esplosioni di supernova. Scopo della tesi, infatti, è quello di testare la validità dei risultati ottenuti dalla simulazione (generata tramite l'implementazione del recente modello di feedback stellare *SMUGGLE* presente all'interno del codice a griglia mobile *AREPO*), dal punto di vista della formazione stellare, degli eventi di supernova e dei fenomeni di espul-

sione/accrescimento di gas durante l'evoluzione temporale del sistema per ~ 1 Gyr. A seguito del nostro studio abbiamo ricavato diversi andamenti evolutivi delle proprietà cinematiche del gas, della SF e dell'efficienza di rilascio di energia/impulso da parte delle esplosioni di SN, al fine di ricercare possibili relazioni che mettessero in luce la stretta connessione presente tra tutti questi processi astrofisici.

I risultati ottenuti mostrano che la simulazione, dal punto di vista della cinematica del gas nel suo moto verticale rispetto al piano del disco, è stata in grado di generare fenomeni di esplusione/accrescimento di gas in maniera auto-consistente. Ciò, in combinazione con il graduale esaurirsi del gas a causa della formazione stellare, ha condotto la galassia a regolare la sua SF ad un tasso di $SFR \sim 2\,\mathrm{M_{\odot}\,yr^{-1}}$ e a un tasso di esplosioni di supernove di tipo-II di $SNR \sim 2$ eventi per secolo in accordo con le osservazioni correnti per galassie simili alla Via Lattea. Ulteriori conferme della bontà del modello con cui è stata simulata l'evoluzione della galassia sono state ottenute grazie al fatto che la simulazione è stata in grado di riprodurre la relazione di Kennicutt-Schmidt dedotta dalle osservazioni. Infine, questo lavoro di tesi ha indagato una possibile connessione tra la variazione di densità superficiale del tasso di formazione stellare e l'ammontare di massa di gas esplusa dal disco contenuta entro una certa altezza dal piano galattico in funzione del tempo. Ciò è stato fatto al fine di valutare l'esistenza di un possibile valore critico per la Σ_{SFR} tale per cui, al di sopra di questa soglia, si possano delineare chiaramente fenomeni di espulsione di gas su scala galattica. I risultati ottenuti però non mostrano evidenze dell'esistenza di un tale valore e che ulteriori approfondimenti e simulazioni di confronto sono necessari per avvalorare questi risultati preliminari.

Chapter 1

Introduction

The current paradigm of cosmic structure formation is described by the Λ Cold Dark Matter (ΛCDM) model. Nowadays, this model has emerged as a concordance cosmological model that tries to explain the formation and evolution of cosmic structures in order to describe the Universe observed in its current state after an estimated age of ~ 13.8 Gyr (see [1], [2], [3]). The cosmological parameters predicted by ΛCDM consider the content of the Universe, with an expansion rate given by an Hubble constant of $H_0 \approx 68\,\mathrm{km\,s^{-1}\,Mpc^{-1}}$, constituted by a dominant component of dark energy $\Omega_\Lambda \approx 0.70$, which is attributed to a cosmological constant responsible for the accelerated expansion of the Universe, of a component of dark (non-baryonic) matter $\Omega_{DM} \approx 0.25$ responsible for the large-scale gravitational effects on cosmic structures, and a component of ordinary baryonic matter $\Omega_B \approx 0.05$ constituting the observable objects because of its own gravitational and electromagnetic interactions. In this scenario, dark matter decouples from the radiation field before the baryons, thus representing the dominant component from the point of view of gravitational instabilities. It is assembled in halos through gravitational collapse and generates sites in which the baryonic matter can in turn fall in the innermost regions. Once densities are high enough, baryonic matter undergo the process of gravitational collapses as well, thus creating the cosmic structures observable today. In particular, the assembly of cosmic structures proceeds in a hierarchical fashion, with small structures forming first and subsequently, as time progresses, increasingly large and massive objects (such as the first galaxies and galaxy clusters) will emerge as a result of the accretion of fresh cosmological gases and galactic merging phenomena (see [4], [5], [6], [7]). The majority of the aspects concerning the formation and evolution of cosmic structures, and in particular galaxies, in a cosmological context are still not well understood and most of the theoretical hypotheses are still awaiting observational confirmation. To model these systems in a detailed way, it is necessary to consider the synergy between physical phenomena operating on a very wide range of spatial and temporal scales. To get an idea of the very large range of spatial scales involved in the formation of cosmic structures it is sufficient to think of individual stars, whose dimensions are well below sub-pc scales. These in turn are the building blocks of galaxies, that have a typical dimension of tens of kpcs, and that can organize themselves in galaxy clusters extending on Mpc scales. The temporal span of the physical mechanisms processed by these cosmic objects also cover a wide range of time scales, from atomic physics (for example processes involved in gas cooling) to the interactions between intracluster medium and galaxy clusters on a time scale of the order of Gyr. Understanding and accurately describing all these physical phenomena concurring in shaping cosmic structures, is the key to validating current cosmological theories.

With the technological and mathematical development that has taken place over the last decades, numerical simulations represent one of the most used tools in the theoretical investigation of galaxy formation. In particular, modern numerical simulations can be employed to create virtual laboratories of portions of the Universe and to test the individual components that constitute it [8]. The challenges posed to modern simulations by the complex nature of galaxy formation are addressed with the use of parallel supercomputers, that have become increasingly faster in the processing and storage of data, and with the improvement of numerical algorithms that are able to meet the simultaneous demand between very high spatial, temporal, and mass resolution. In particular, problems arise in the conjunction of the physical processes that take place in the small spatial scales (often described by sub-resolution or sub-grid models[1]) and modelling large volumes of the Universe [32]. In other words, the desirable objective is to study galaxies in their fully dynamical cosmological environment, reducing as much as possible the limitations related to numerical resolution in order to obtain an increasingly accurate modeling of the physical phenomena involved.

One of the open problems about the formation and evolution of galaxies is certainly

---

[1] Sub-resolution models are basically an efficient implementation in simulations of all those physical phenomena that currently cannot be resolved, for instance turbulence in the interstellar medium (ISM), star formation, stellar and AGN feedback, to cite the most prominent.

related to the physics of gas permeating these systems and the environment that hosts them. By restricting the field of the discussion to the class of star-forming galaxies similar to the Milky Way, it appears by current observational data that they have been able to form stars at a roughly constant rate of $\sim 2\,\mathrm{M}_\odot\,\mathrm{yr}^{-1}$ for almost their entire lifetime (see for instance [85], [86]). This would seem to be an indication that these systems have been able to access to a supply of baryonic material (gas) to continuously create new stars. This material could have been acquired through efficient cooling processes, by gas circulation phenomena (inflow/outflow) in a region close to the star-forming disc [9], [10], [68], or thanks to the accretion of gas of still uncertain cosmic origin (see [11], [12] and references therein). A strong debate is still ongoing on the role of cosmological gas accretion and gas circulation in the evolution of galaxies. For instance, the presence of a cosmological inflow gas is considered to explain the observations of galaxies with a high star formation rate at a redshift $z \approx 2$ – which presumably follows an “explosive” feedback episode – to very efficiently supply fresh gas for star formation into the galactic system [13]. Another way for a galaxy of getting fresh gas for star formation involves a galactic fountain flow in which gas outflows (mostly powered by supernovae) from the galactic plane tend to remain confined in the region of the disc. The accretion of gas by the galaxy occurs via an interaction between such ejected gas and the hot gas surrounding the galaxy, which cools and eventually falls onto the disc forming new stars (see [14], [90]). An important aspect to consider in order to better understand the gas cycle, is that there are various pieces of evidence (gathered from observations and simulations) pointing to a multiphase nature of the gas both inside and outside galaxies (see e.g. [15], [97], [98]). Moreover, simulations also suggest that stellar feedback (in the form of SN explosions, stellar winds and radiation) is an important regulator of star formation and shapes the properties of the multiphase gas within and outside galaxies [18], [98]. Therefore, simulated models of galaxy formation are excellent laboratories in which the the different stellar feedback channels can be thoroughly tested.

In this thesis we have focused our attention on one of the major contributors to the injection of energy and momentum to the ISM present of an isolated MW-like galaxy simulation, i.e. the feedback channel related to SN explosions. Recent studies would seem to indicate that these characteristic galaxy events are the main responsible in structuring the gas in its multiphase components and in the generation of gas outflows phenomena

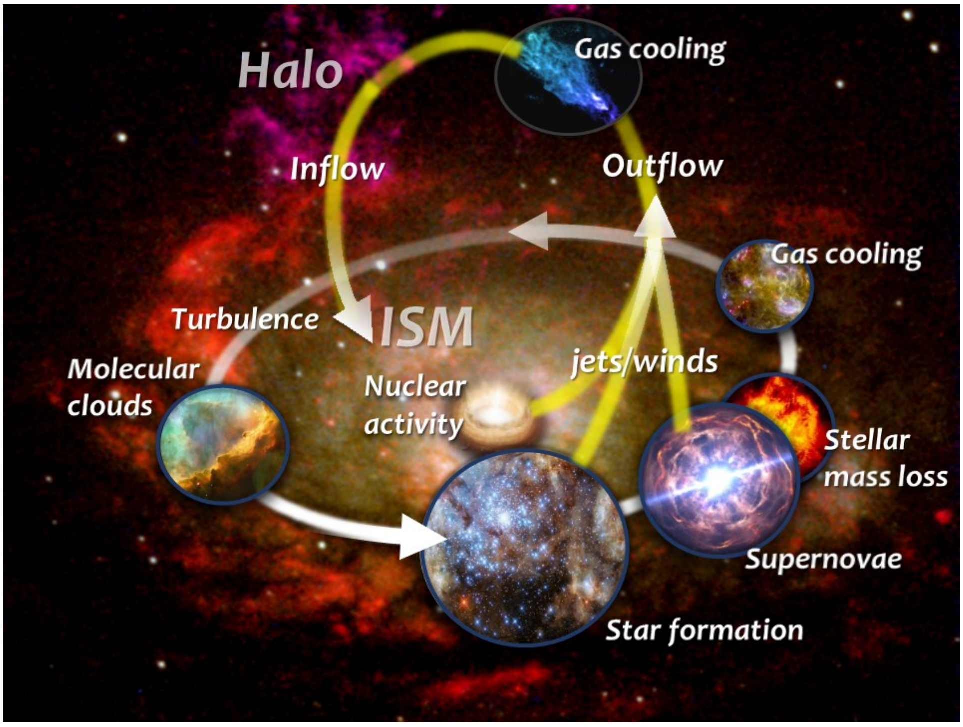

Figure 1.1: Schematic illustration of the main physical phenomena that lead to the circulation of gas in a star-forming galaxy. The cooling and reaching of high densities of molecular gas leads to the formation of stars in the galaxy and, as a result of their evolution, stars lose mass (stellar winds) and can explode as SNae, thus re-injecting gaseous material into the interstellar medium or even launching powerful gas outflows on a galactic scale. This expelled gas can then be lost by the system or can cool and accreted again by the galactic disc. Other physical mechanism phenomena can generate the expulsion of gas from the galactic plane such as radiation pressure, stellar jets or (if present) active galactic nucleus (AGN) feedback. Figure taken from the *SPICA* spacecraft mission website: https://spica-mission.org

on a galactic scale ([72], [84]). However, this is still an open issue as other theoretical works would seem to indicate others important feedback channel that are comparable with SNae from the point of view of the momentum imparted and the energy injected into the gas media, such as: the radiation pressure and photoionization of the young stars (see [99]), the dynamical impact of cosmic rays (see [55]), stellar jets and other processes (see Fig. 1.1 for a cartoon representation of this complex interplay).

One of the major current limitations in the modelling of these feedback components is related to the high computational cost required to handle an increasing number of gravitationally and hydrodynamically interacting elements of the galaxy system. In fact, with increasing numerical resolution elements previously neglected physical phenomena can become relevant (and thus have to be explicitly modeled) in the study of the gas properties in terms of temperature and density reached. Several strategies have been implemented in the codes for the treatment of physical processes affecting gas in galaxies in an attempt to best reconstruct its different phases, for example by using an effective equation of state (see [100]) or trying to adopt an increasingly accurate treatment in the modeling of feedback phenomena interacting with the gas media without resorting to an effective equation of state description (see e.g. [18]).

The isolated galaxy simulation we have analyzed in this thesis has been performed with the recent stellar feedback and ISM model *SMUGGLE* [18] implemented in the moving-mesh code *AREPO* [17]. The main goals of the thesis are verifying the validity of the model used to simulate the galaxy and looking for possible connections between the various processes (vertical dynamics of the gas with respect to the galactic plane, star formation activity, SN explosion and the generation of gas outflow/inflow on a galactic scale) that occur in the system on a time scale of ~ 1 Gyr, in order to better understand the complex interplay between the galaxy and its immediate surroundings.

Specifically, in chapter 2 of this thesis we present a brief review of numerical codes commonly used in astrophysics and cosmology for the gravitational (N-body codes) and hydrodynamic (Eulerian and Lagrangian codes) description of the elements constituting the simulated system. This was done to better understand the innovative *AREPO* code, which is able to combine the advantages of the standard approaches mentioned above, overcoming many of their limitations and increasing the simulation accuracy. In chapter 3, we discuss the initial conditions and the parameters that were set in the model and used to carry out the *closed-box* simulation of the galaxy which we have analyzed in this work. We focused on the *SMUGGLE* model implemented in *AREPO* for the treatment of the ISM and stellar feedback, describing in detail the feedback channel generated by the SN explosions, which will lead to a self-consistent generation of gas outflows on a galactic scale due to the injection of energy and momentum by these massive stars at the end of their life cycle. In chapter 4, we enter the heart of the thesis by reporting the analysis that we carried out, especially in terms of gas dynamics of the outflowing gas, star formation, SN explosions and their connection to outflow phenomena.

Finally, in chapter 5, we conclude the thesis discussion with a review of the work we have done, summarizing the results obtained and presenting possible lines of investigation that can be developed in future work.

Chapter 2

Numerical methods for astrophysics and cosmology

There are several kind of numerical simulation codes that have a large useful applications in astrophysical problems. They represent a powerful tool to model, with an excellent approximation, the physical processes observed in galaxies and to test theoretical models of galaxy formation and evolution.

There are two main families of codes typically used in computational astrophysics and cosmology: N-body codes and hydrodynamical codes [33]. These types of simulation codes allow to follow and understand the evolution of a physical system in terms of gravitational and fluid dynamics, respectively. In this chapter we present a brief review of how N-body and hydrodynamic codes work. In galaxy formation simulations the two approaches are often combined (see, e.g. [32], for a recent review on this topic). In particular, as an example of a code that combines the N-body and hydrodynamic approaches, we will introduce the moving-mesh code AREPO that has been used to perform the simulation analyzed in this work.

2.1 Numerical methods for non-collisional systems

2.1.1 N-body codes

The observed Universe is constituted by an incredibly large number of structures that characterize its content. Modelling gravitational effects among those structures from a theoretical point of view is very challenging. Numerical simulations represent a powerful tool to meet this challenge and to perform "experiments" that try to reproduce at best the real phenomena observed in the cosmos. In this regard, numerical codes implement concepts of modern physics using different strategies and algorithms to perform simulations which attempt to understand and compare physical behaviors otherwise difficult to study. These numerical codes are physically reliable, especially for N-Body simulations where the only physical interaction acting on a particles system is the gravity.

As far as gravity is concerned, gravitational interactions between a set of N particles of mass m_i, and position $\mathbf{x}_i$ are be described by two fundamental equations which are Newton's law of universal gravitation combined with Newton's second law

$$m_i\,\mathbf{a}_i = \mathbf{F}_i = -\nabla\phi = -\sum_{i,j\neq i} G\,m_i\,m_j\,\frac{\mathbf{x}_i - \mathbf{x}_j}{|\mathbf{x}_i - \mathbf{x}_j|^3} \tag{2.1}$$

and Poisson's equation:

$$\nabla^2\phi = 4\pi G\rho \tag{2.2}$$

where in equation (2.1) we have that $\mathbf{F}_i$ is the gravitational force acting on the i-th particle of the system, $\mathbf{a}_i$ represents the acceleration of the i-th particle and denoted by the letter G the universal gravitational constant, while in the equation (2.2) we have that ϕ is the gravitational potential and ρ represents the total density. In particular, in the isolated galaxy simulations that we are going to examine in chapter 3, the contributions to the total density are given by gas component ρ_{gas}, stellar disc and bulge ρ_* and the dark matter halo $\rho_{\mathrm{D}M}$, that is $\rho = \rho_{gas} + \rho_* + \rho_{DM}$.

Gravity codes numerically solve the system of differential equations (2.3) (see below) by discretizing the problem into N resolution elements, and for this reason they are called the N-body codes. The discretization procedure takes advantage of different strategies based on current technologies in order to reduce the computational costs and therefore to more efficiently manage the large number of elements, which need to be considered to model complex systems such as galaxies and dark matter halos. The aim of N-body codes is to follow step by step the temporal evolution of these N particles solving the equation of motion of each single particle of the system. This is possible if the chosen time step is small enough to follow the behaviour of each single particle during its motion. The equations typically to be solved in an N-body code are the following

$$\begin{cases} \mathbf{F}_i = G\, m_i \displaystyle\sum_{i \neq j} \frac{m_j}{r_{ij}^2} \\ \mathbf{a}_i = \dfrac{d\mathbf{v}_i}{dt} = \dfrac{\mathbf{F}_i}{m_i} \\ \mathbf{v}_i = \dfrac{d\mathbf{x}_i}{dt} \end{cases} \tag{2.3}$$

and which are: the equation of the gravitational force felt by the i-th particle and given by the contribution of all the other $N-1$ particles (where in particular r_{ij} represents the distance between the particles i and j), the equation that define acceleration (Newton's second law), and the equation that define velocity. The last two equations are nothing more than the equations of motion. The vast majority of N-body codes essentially calculate and update particle positions and velocities in the same way, but differ in the method used to calculate the gravitational force. The latter is the most expensive operation from the computational point of view, because at each time step of the simulation the code must calculate the sum of all the forces acting on each single particle by the other particles. Generally speaking, for a large number of particles, which might be needed for accuracy, N-body methods become computationally expensive[1] as we will see in the next section. Once the method to obtain the force $\mathbf{F}_i$ is chosen, this is used to update the velocity, then to update the position. In other words, to update velocity and position of the N particles, N-body codes proceed to a numerical integration over time of the last two equations (2.3). One of the possible approaches is the so-called leapfrog scheme, a second-order numerical integration method where the error introduced at each time step Δt is equal to $O(\Delta t^3)$, in which at each time step velocity and positions are updated in an alternating manner. Taking a particle at time t_n with position $\mathbf{x}_i(t_n)$ and velocity $\mathbf{v}_i(t_n)$, the leapfrog method uses three operations to find the new positions $\mathbf{x}_i(t_{n+1})$ and velocities $\mathbf{v}_i(t_{n+1})$ at time $t_{n+1} = t_n + \Delta t$. In particular, there are two formulations of the method with essentially share the same properties. These are the called drift-kick

---

[1] The number of gravitational interactions that follow from equation (2.3) is $O(N^2)$, where N is the number of particles. So an increase of 10 times the number of particles causes an increase of a factor of 100 in the number of gravitational interactions to be evaluated to compute the accelerations.

drift (DKD) leapfrog method

$$\mathbf{x}_i(t_{n+\frac{1}{2}}) = \mathbf{x}_i(t_n) + \frac{1}{2}\,\mathbf{v}_i(t_n)\,\Delta t \tag{2.4}$$

$$\mathbf{v}_i(t_{n+1}) = \mathbf{v}_i(t_n) - \nabla\phi\,[\mathbf{x}_i(t_{n+\frac{1}{2}})]\,\Delta t \tag{2.5}$$

$$\mathbf{x}_i(t_{n+1}) = \mathbf{x}_i(t_{n+\frac{1}{2}}) + \frac{1}{2}\,\mathbf{v}_i(t_{n+1})\,\Delta t\,, \tag{2.6}$$

in which positions are first computed (i.e., the particles are "drifted") at half the time step and these new values are used to compute the gravitational accelerations required to update particle velocities (the "kick" operation). With the new values of the velocity a finale drift operation is performed to update the particle positions to the final time. In the kick-drift-kick (KDK) leapfrog scheme

$$\mathbf{v}_i(t_{n+\frac{1}{2}}) = \mathbf{v}_i(t_n) - \frac{1}{2}\,\nabla\phi\,[\mathbf{x}_i(t_n)]\,\Delta t \tag{2.7}$$

$$\mathbf{x}_i(t_{n+1}) = \mathbf{x}_i(t_n) + \mathbf{v}_i(t_{n+\frac{1}{2}})\,\Delta t \tag{2.8}$$

$$\mathbf{v}_i(t_{n+1}) = \mathbf{v}_i(t_{n+\frac{1}{2}}) - \frac{1}{2}\,\nabla\phi\,[\mathbf{x}_i(t_{n+1})]\,\Delta t\,, \tag{2.9}$$

the order of the operations is reversed: first the particles are "kicked", that is their velocity is updated, for half a time step, then a drift operation for the whole time step is performed and the new positions are then used to compute the gravitational accelerations to perform the last update of the particle velocities. Please note that the KDK scheme involves two gravitational acceleration calculations per time step, whereas only one is performed the DKD scheme. Since computing gravitational accelerations is the most computationally intensive part of an N-body code, usually in the applications the DKD scheme is preferred over its KDK counterpart.

There are several gravity solver methods to calculate the gravitational acceleration needed to update particle velocities and positions, such as Particle-Particle (PP) method, grid methods such as Particle Mesh (PM) or Particle-Particle/Particle-Mesh (P3M), the so-called Hierarchical Tree (HT) algorithms and various other hybridizations of these methods. We will focus on this last method only, because, as we will see in section 2.5, this method used to compute the gravitational interactions in the simulations that we are going to analyze in this work. We refer the interested reader to [32] for an overview of other approaches to efficiently compute the gravitational force.

2.1.2 Hierarchical Tree methods

The method of hierarchical "multipole expansion" implemented in tree algorithms allows to compute more effectively the gravitational interactions between an ensemble of $N \gg 1$ particles [33] [34]. To illustrate this let us consider a system of N particles within a certain simulation volume and take into account a group of particles close to each other but relatively far from a generic i particle. Since the force is proportional to the inverse of the distance squared

$$\mathbf{F}_i \propto \frac{\mathbf{x}_i - \mathbf{x}_j}{|\mathbf{x}_i - \mathbf{x}_j|^3}\,, \tag{2.10}$$

instead of calculating all the distances that bind the i-th particle with each of the particles that make up the group, it is sufficient to calculate the distance between the particle in question and the barycentre of the particle group to get a sufficiently accurate estimation of the gravitational acceleration. In other words, the gravitational contributions exerted by the group of particles on the i-th particle can be considered as a single contribution of the force generated by a single object (of mass equal to the sum of the masses of the single particles) placed in the center of mass of the system composed by them. Therefore it is not necessary to calculate all the force pairs between the particles (which requires an order of N operations per particle), but the calculation of the force acting on each particle is done by direct summing only for the closest pairs of particles (similar to the particle-particle [PP] method that equation (2.3) defined). In this way, less operations are required to be performed by the code. It can be shown that this method reduces computational complexity to $N \log(N)$ unlike the PP method which, as mentioned above, requires N^2 opera

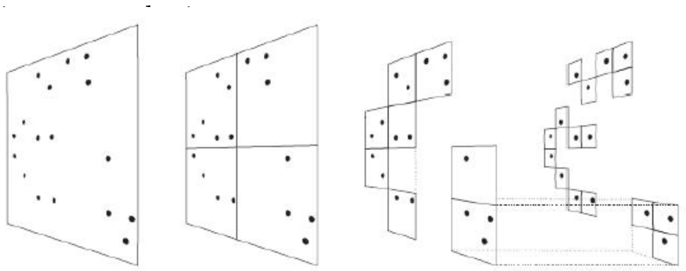

Figure 2.1: Scheme induced by a bi-dimensional particle distribution in which the decomposition into sub-cells follow the hierarchical tree method (that is an oct-tree [33]). The domain containing the particles is subdivided iteratively until each cell contains at most one particle inside it. Figure was taken from [35]).

The previous procedure is usually implemented by building a so-called hierarchical tree. The method used to construct a hierarchical tree consists of an iterative subdivision of the space (simulation volume) containing the N particles. In practice the simulation volume is split into 8 sub-volumes, and this procedure is repeated until the obtained sub-volumes contain at most a single particle. Each of these subdivisions can be considered as a branch (or node) of the tree generated by the subdivision of a previous cell (or root node). We report in Fig. 2.1 a bidimensional (2D) representation of such a tree.

To compute the gravitational acceleration, a reference angle is set whose underlying arc represents the threshold to determine whether a given group of particles is far enough to be considered as a single object from the i-th target particle (opening-angle criterion [34]). If the "multipole expansion" of the node (or sub-volume in which the particles are contained) does not provide an accurate approximation of the gravitational force, the algorithm "opens" the node and considers in turn each of the 8 sub-volumes contained in it. The operation is repeated recursively until the particles are far enough away from the i particle or until a sub-volume containing none or at most one particle is reached (in which case the acceleration is calculated directly).

The main advantages of HT methods are related to absence of a grid that limits the resolution returning very accurate results. They can be parallelized relatively easily and it is also possible to combine them with other N-body approached such as Particle Mesh codes (the so-called TreePM codes). However, they typically require a substantial amount of memory in computers in particular when the tree code is combined with other types of codes [57].

2.2 Numerical methods for fluid dynamics

Generally speaking, modelling the evolution of gas is more articulated because baryons do not feel only gravity, but are subject to many physical processes whose numerical treatment is complex due to the large dynamic range in scales and the intrinsic multi-physics problem of galaxy evolution. A prominent example is the modelling of the interstellar medium (ISM). Due to its complex multi-phase structure, *ab-initio* ISM simulations are still technically very challenging. Various physical processes have to be necessarily considered to accurately model the interstellar multi-phase structure in a direct way.

For instance, simulating dense phases such as cold gas requires very long and accurate calculation times, as well as considering very small time steps to reliably follow all the processes that influence the temporal evolution of this gaseous phase. In the simulations of this specific gas phase, it is in fact necessary to consider the interactions that take place between gas, radiation and interstellar dust or the various sources of feedback that inexorably and incisively characterize the structure of the ISM in a galaxy [32]. Moreover, also the forces at play together with gravity, such as thermal pressure, magnetic pressure and turbulent pressure support, are numerous and should all be considered in ISM simulations. We note that short timescales are associated with dense and cold gas, as it is closely related to the phenomenon of gravitational collapse within galactic Giant Molecular Clouds (GMCs). In fact, the cooling of the molecular gas (under proper conditions of density and gravitational collapse) leads to the formation of new stellar populations in a star-forming galaxy, affecting considerably the spectrophotometric and chemical evolution of the galaxy itself. For this reason, we need also to consider the standard stellar evolution models, which take into account the death of stars in the form of supernova explosions and the consequent release of energy and momentum to the interstellar medium. As a consequence, this phenomenon produces gas heating in the ISM, generating outflows, galactic fountains and more other feedback which, if inserted in the models, return numerical results ever more closer to what we really observe in the Universe.

All these mechanisms act on very different scales, consequently they will have to be dealt with at different scales of resolution. This is currently still a problem in numerical simulations whose requirement is to handle an increasing number of objects interacting at different scales, from the smallest (Dense Cores, GMCs, turbulent gas phases, etc.) to those on a large galactic scale (SN explosions, galactic fountain, outflow/inflow phenomena of gas). From the examples given, we can understand that modelling the hyrodynamical evolution of the gas is complex, not only because of hydro process but also because the gas "feels" other processes as well [8].

Finally, we also note that, unlike gravity, which is a long-range force scaling as r^{-2}, hydrodynamic effects have a rather limited range of action – they represent short-range effects – and as a consequence there will be a different behaviour of the fluid between small and large scales. For instance, there will be short-range effects due to the local interactions of the fluid, such as turbulence phenomena, which will not be visible on a large scale, where the global motion of the fluid will be mostly determined by gravitational and mechanical energy transfer effects (thermal, kinetic, etc.). In the hydrodynamic codes, that we are going to discuss, we will see that these considerations are important as the basis of the strategies used to delineate the exchange of conserved variables between particles or cells of the fluid which are locally in close interaction.

2.2.1 Basics of hydrodynamic methods

As far as hydrodynamics is concerned, the numerical methods that simulate the behaviour of the gas are typically divided in two different categories: the Lagrangian and Eulerian approaches. These numerical methods solve the same system of fundamental equations of fluid dynamics using different methods to follow the behaviour of fluid motion, as it will be clearer at the end of this chapter 2. Before discussing the Eulerian and Lagrangian methods, we briefly present the equations that these methods are attempting to solve and their main properties. These equations are known as Euler equations. They are a system of partial differential equations that written in conservative form (read [17])

$$\begin{cases} \dfrac{\partial \rho}{\partial t} + \nabla \cdot (\rho\, \mathbf{v}) = 0 & \text{Continuity equation (or mass conservation law)} \\ \dfrac{\partial (\rho\, \mathbf{v})}{\partial t} + \nabla \cdot (\rho\, \mathbf{v} \otimes \mathbf{v} + P\, \mathbf{I}) = 0 & \text{Euler equation (or momentum conservation law)} \\ \dfrac{\partial \epsilon_{tot}}{\partial t} + \nabla \cdot [(\epsilon_{tot} + P)\, \mathbf{v}] = 0 & \text{Energy conservation law} \end{cases} \tag{2.11}$$

The first equation, the continuity equation of mass, represents the first fundamental relation of fluid dynamics and yields the information that mass is not created or destroyed within the fluid. In particular, ρ is the density of the fluid and $\mathbf{v}$ is its velocity vector (with three components: u, v, w).

The Euler equation is the second fundamental conservation equation of fluid dynamics, also known as the force equation or momentum conservation equation. In this equation $\rho\, \mathbf{v}$ is the momentum (per unit volume) of the fluid, $\mathbf{v} \otimes \mathbf{v}$ is the product tensor given by

$$\mathbf{v} \otimes \mathbf{v} = \begin{pmatrix} u^2 & u\,v & u\,w \\ v\,u & v^2 & v\,w \\ w\,u & w\,v & w^2 \end{pmatrix}, \tag{2.12}$$

and the term $\rho\,\mathbf{v} \otimes \mathbf{v}$ is the momentum flux, while the quantity $P\,\mathbf{I}$ is the product of (thermal) pressure P exerted by the fluid and the unit tensor $\mathbf{I}$

$$\mathbf{I} = \begin{pmatrix} 1 & 0 & 0 \\ 0 & 1 & 0 \\ 0 & 0 & 1 \end{pmatrix}. \tag{2.13}$$

We remind that for a perfect fluid, the pressure is independent of the direction (isotropic case).

The physical meaning of the energy conservation law can be deduced by integrating both terms over a generic volume containing a portion of the fluid. By using the Gauss theorem for the divergence terms we obtain

$$\frac{\partial}{\partial t}\int\limits_V \epsilon_{tot}\,\mathrm{d}V + \int\limits_S \mathbf{n}\cdot\epsilon_{tot}\mathbf{v}\,\mathrm{d}S + \int\limits_S \mathbf{n}\cdot P\,\mathbf{v}\,\mathrm{d}S \;=\; 0\,, \tag{2.14}$$

in which the first term is the variation of the total energy over time, the second term shows that the variation of energy within an arbitrary volume is due either to energy entering (or leaving) that volume because of the fluid motion, and the third term is the work done per unit of time $\frac{dW}{dt}$ by pressure forces $\mathbf{F}_P$ on the fluid within that surface, that is

$$\frac{dW}{dt} = \mathbf{F}_P\cdot\mathbf{v} = -\int\limits_S \mathbf{n}\cdot P\,\mathbf{v}\,\mathrm{dS}\,. \tag{2.15}$$

Moreover,

$$\epsilon_{tot} = \epsilon_{kin} + \epsilon_{int} = \frac{1}{2}\,\rho\,\mathbf{v}^2 + \rho\,e = \frac{1}{2}\,\rho\,(u^2+v^2+w^2) + \rho\,e \tag{2.16}$$

where ϵ_{tot} is the total energy density with e being the specific internal energy of the fluid.

This system of conservative equations is complemented by an equation of state (the ideal gas law) of the form

$$P = (\gamma - 1)\,\rho\,e \qquad \text{Ideal gas law}, \tag{2.17}$$

which represents a closure relation between the internal energy e and the pressure P. We will assume that γ is the adiabatic index for a mono-atomic gas and therefore $\gamma = 5/3$.

We note that the above equations describe an ideal case and therefore do not take into account any dissipative terms (such as cooling/heating processes), gravitational interactions, transport phenomena such as viscosity or heat conduction.

This system of governing equations is non-linear and the analytical resolution is often arduous. The system (2.11) is composed of five equations (plus the equation of state), and six unknowns variables u, v, w, ρ, P, e. In their most general form, these conservation laws can be written as integrals over control volumes, then, exploiting certain assumptions about the smoothness of the variables, it is possible to recover the differential relations written in equation (2.11). Moreover, the integral form is often more convenient for a numerical approach: as a matter of fact the integral are evaluated over control volumes that naturally correspond with the computational cells used to discretize the flux quantities. This approach is also known as Finite Volume methods (see also [23]).

In order to understand the physics behind Euler equations and highlight the connection between the properties of the equations and the numerical methods used to solve them, we take as an example the continuity equation and derive it from its integral form. The others can be derived in a similar way (see e.g. [24]). Let us consider a Cartesian space and a fluid moving at $\mathbf{v}$ speed through it. Let us also consider a finite region of the flow (of reasonably large size) fixed in space with the movement of the fluid, as shown in Fig. 2.2. This region represents a finite volume V (which we will denote as control volume) delineated by the closed surface S (also named control surface area). Asserting that the mass is conserved means that net mass flow out of control volume V through control surface S is equal to the time rate of decrease of mass inside control volume, as we will show shortly.

The figure also shows an element of volume dV within V and a vector elemental surface area dS also crossed by the flow field (that is represented through the so-called streamlines, i.e. the tangents to the fluid velocity at each point). An elemental mass flow out of an element of volume trough the elemental surface is:

$$\rho\, v_{\mathbf{n}}\, dS = \mathbf{n} \cdot (\rho\, \mathbf{v})\, dS \tag{2.18}$$

where $\rho = \rho(x, y, z, t)$ is the scalar density field, $\mathbf{v} = u(x, y, z, t)\,\mathbf{i} + v(x, y, z, t)\,\mathbf{j} + w(x, y, z, t)\,\mathbf{k}$ is the vector velocity field (where the x, y and z components of the velocity are given by u, v and w and the unit vectors are $\mathbf{i}$, $\mathbf{j}$ and $\mathbf{k}$), and $\mathbf{n}$ is the normal vector

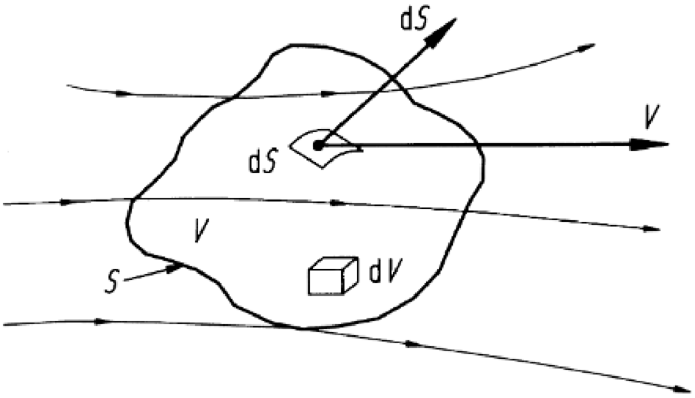

Figure 2.2: Finite control volume fixed in space approach. The governing equations obtained by applying this approach, in either integral or partial differential form, return a conservative form of these equations. The same figure is shown in [24].

at the surface always pointing outwards from the control volume. Taking into account that the summation over S of the elemental mass flows (the left side of the expression (2.18)) corresponds to the net mass out of the entire control volume trough the control S, then this leads to a boundary concept represented by a closed surface integral of the right side of the expression (2.18), i.e.

$$\iint\limits_{S} \mathbf{n} \cdot (\rho\, \mathbf{v})\, \mathrm{d}S \,. \tag{2.19}$$

In the above equation, we consider that the velocity vector $\mathbf{v}$ can point out or inside the control volume (as shown in the Fig. 2.2), then the product $\mathbf{n}. \cdot (\rho\, \mathbf{v}) dS$ will be positive when there is mass outflow from the volume considered and will be negative when the mass inflow is entering the control volume. On the other hand, the total mass contained within V is given by

$$\iiint\limits_{V} \rho\, \mathrm{d}V \,. \tag{2.20}$$

Therefore, the time rate of decrease mass inside the control volume is

$$-\frac{\partial}{\partial t} \iiint\limits_{V} \rho\, \mathrm{d}V \tag{2.21}$$

and by recalling (2.19) one gets

$$\iiint\limits_{V} \frac{\partial \rho}{\partial t}\, \mathrm{d}V + \iint\limits_{S} \mathbf{n} \cdot (\rho\, \mathbf{v})\, \mathrm{d}S \, = 0 \,. \tag{2.22}$$

In the previous equation the time derivative can be placed inside the volume integrals because V is fixed in space and hence the limits of integration of the integral are constant.

We now use Gauss' theorem (or the divergence theorem) to express the surface integral as a volume integral

$$\iint\limits_S \mathbf{n} \cdot (\rho\,\mathbf{v})\,\mathrm{d}S = \iiint\limits_V \nabla \cdot (\rho\,\mathbf{v})\,\mathrm{d}V\,, \tag{2.23}$$

and by substituting the equation (2.23) in the equation (2.22) and placing the terms under the same volume integral we obtain the integral form of the continuity equation or mass conservation

$$\iiint\limits_V \left[\frac{\partial\rho}{\partial t} + \nabla \cdot (\rho\,\mathbf{v})\right]\,\mathrm{d}V = 0\,. \tag{2.24}$$

The integral in equation (2.24) is equal to zero only if the integrand is null. This is because the chosen control volume is purely arbitrary. Hence, as we wanted to show, we obtain again the partial differential form of the continuity equation in conservative form

$$\left[\frac{\partial\rho}{\partial t} + \nabla \cdot (\rho\,\mathbf{v})\right] = 0\,. \tag{2.25}$$

All the equations of the hydrodynamics can be derived in their integral form by following a similar line of reasoning. We report such equation below for convenience. From these expression is trivial to recover the equation in their conservative (differential) form (2.11).

$$\begin{aligned}
&\iiint\limits_V \left[\frac{\partial\rho}{\partial t} + \nabla \cdot (\rho\,\mathbf{v})\right]\,\mathrm{d}V = 0 \\
&\iiint\limits_V \left[\frac{\partial(\rho\,\mathbf{v})}{\partial t} + \nabla \cdot (\rho\,\mathbf{v} \otimes \mathbf{v} + P\,\mathbf{I})\right]\,\mathrm{d}V = 0 \\
&\iiint\limits_V \left[\frac{\partial\epsilon_{tot}}{\partial t} + \nabla \cdot [(\epsilon_{tot} + P)\,\mathbf{v}]\right]\,\mathrm{d}V = 0
\end{aligned} \tag{2.26}$$

At the most fundamental level, as we will explain in section 2.3.1, an hydrodynamical solver basically calculates, at each time step, the divergence terms of these equations (representing the flux of the hydrodynamical quantity of interest) by employing different strategies depending on the type of approach used. These fluxes are then used to update the value fluid variables and get therefore a numerical approximation of the time evolution of the system.

In the following sections we will briefly describe the main features of the Eulerian (section 2.3.1) and Lagrangian (section 2.4.1) codes, which correspond to two different numerical implementations of hydrodynamics, highlighting their advantages and limits. We will then see, in section 2.5, how the Eulerian and Lagrangian approaches can be put together in order to exploit their strengths and minimizing their shortcomings. We will do so by discussing in more depth the code used for the numerical simulations analyzed in this work: the AREPO code [17].

2.3 Eulerian codes

2.3.1 Conservative Eulerian codes

The Eulerian hydrodynamic technique is a numerical approach for hydrodynamical simulations that typically implements one or more spatial structured or unstructured meshes fixed in space. The location of the centres of cells that form such meshes are then used to sample fluid variables and follow their evolution in time. More in general a mesh can be thought as a static (i.e. not moving) partition of the simulation volume.

A mesh (or grid) is constructed in such a way as to form a N-dimensional[2] tessellation of the simulation domain. This tessellation is composed of fixed cells that typically are of regular Cartesian shape, or in other words arranged in a N-dimensional lattice. As we will further discuss in section 2.5, this kind of regular grid is a particular case of a more general Voronoi tessellation of space, in which cells (depending on the dynamics of the fluid motion) can be distorted into irregular shapes.

Through the fundamental conservation laws of fluid dynamics (2.26) and by taking a volume-weighted average quantities of *conserved* hydrodynamic variables (ρ, $\rho\mathbf{v}$, and ϵ_{tot}), it is possible to follow at every temporal step the behavior of a fluid flowing within these cells. To illustrate this, let us consider the system of conservative equations (2.11) and discretize them on a 1D mesh in which cell centers are Δx apart

$$\frac{d\mathbf{u}_i}{dt} + \frac{\mathbf{f}_{i+1/2} - \mathbf{f}_{i-1/2}}{\Delta x} = 0\,. \tag{2.27}$$

In equation (2.27) where $\mathbf{u}_i$ is the volume-weighted value of the conserved variables $\mathbf{u} = (\rho,\, \rho\mathbf{v},\, \epsilon_{tot})$ within the cell i, and $\mathbf{f}_{i+1/2}$ is the flux vector at the interfaces $i+1/2$ between cells i and $i+1$. Moreover, as we will soon see during the discussion, also the

---

[2] N is the dimensionality of the simulation domain under examination.

so-called vector $\mathbf{w} = (\rho,\, \mathbf{v},\, P)$ of primitive variables will be used in order to calculate the intercell fluxes needed to update the values of conserved variables $\mathbf{u}_i$ over time.

The operations performed by an Eulerian code at each time step to evolve the system (2.27), under the assumption of knowing, at the beginning of a given time-step, the value of the primitive variables $\mathbf{w}_i$ at the center of each cell i are in general as follows:

- the values of the primitive variables at the cell centers $\mathbf{w_i}$ need to be extrapolated (at a given order of accuracy) at the cell interfaces $i + 1/2$; we do not discuss in detail here how this operation is performed and refer the reader to [37, 38] for some of the techniques used;
- after this phase, called *reconstruction*, primitive variables are available at the cell interfaces $i + 1/2$ and fluxes can be computed; usually two estimates, called respectively "left" $(\mathbf{w^L_{i+1/2}})$ and "right" $(\mathbf{w^R_{i+1/2}})$ [3], of the primitive variables at the inter-cell are available; thus, for each interface a Riemann problem is defined [40] and the solution of such problem yields the value of the fluxes; the algorithms solving (either exactly or approximately) Riemann problems are called Riemann solvers and are a key part of any modern Eulerian hydrodynamical code;
- once the inter-cell fluxes are obtained, equations (2.27) are evolved in time and the value of conserved variables at the cell centres $\mathbf{u_i}$ are updated accordingly.

Note that for simplicity we have only tackled the case of ideal hydrodynamics (i.e. we have not considered any source term) in the 1D case. If source terms are present, they can be added to the inter-cell fluxes before proceeding with the updates of the conserved variables. Moreover, the procedure can be extended to other spatial dimensions if necessary.

2.3.2 Advantages and limitations of Eulerian codes

There are several variants of Eulerian grid codes that follow different implementation with their associated advantages and limitations. Examples of widely-used grid codes in astrophysics and computational cosmology are: Athena [27], Ramses [28], ENZO [29] and so others.

---

[3] the name left and right derive from the fact that, for the extrapolation procedure, values biased at the left or at the right of the interface cab be used (see [37] for more details about this procedure).

An advantage common to all Eulerian codes approach is that the Eulerian approach allows a better description of gradients in the hydrodynamic variables. This in turn implies that discontinuous solutions of the Euler equations, e.g. shocks, are modelled rather sharply and with less numerical diffusivity. This might be important in problems where the correct modelling of such discontinuities is important [16]. Finally, integrating Eulerian codes with N-body methods using grids (such as PM and P3M) is fairly straightforward [39].

On the other hand, one of the main disadvantages of the Eulerian description is the inability to automatically adapt the number of resolution elements to the regions that have to be resolved most frequently. For example, in galaxy formation simulations one needs to have the bulk of resolution elements in the more dense regions (which roughly correspond to the locations were galaxies can be found), whereas low-densities can be modelled with less resolution elements. Eulerian codes are unable, in their most simple incarnation, to automatically adapt resolution to the clustering of matter, whereas the Lagrangian codes (see section 2.4.1) do that by construction. Methods such as Adaptive Mesh Refinement (AMR) have been developed to deal with this type of limitation as good as possible [36]. The AMR technique is currently the solution used to solve the problem of adapting the spatial resolution to the flow characteristics in Eulerian codes. The refining of the grid acts in such a way as to divide the cells into smaller sub-cells by adding resolution elements in high density regions. The price to pay is that the experimenter has to explicitly encode refinement criteria in the code, and the optimal refinement criterion might be simulation dependent.

2.4 Lagrangian codes

2.4.1 Smoothed Particle Hydrodynamics (SPH)

Lagrangian methods represent a different type of approach for hydrodynamics with respect to the Eulerian methods – that we recall discretize the volume of simulation domain – as these codes are particle-based (so the fluid is represented by a finite number of particles). There is not a mesh implemented in this approach: namely these codes assign to each gas particle (or fluid element) all the hydrodynamic variables whose evolution must be tracked. We will see during the discussion that one of the main problems of this method, from the point of view of calculation time, is the need to draw up lists of connected particles, i.e. it is necessary to find the N closest neighbours of a given gas particle on which to mediate the values to obtain the hydrodynamic quantities of interest. Implementations like this one have a wide use in astrophysics, because they make it simple to trace the path of gas particles and allow an easy combination with N-body codes [22].

As mentioned in the previous sections hydrodynamic forces are short-range. Therefore, it is possible to assume in the Lagrangian discretization that only neighbour particles affect the dynamics of the one under exam (also called target particle). Indeed, the contributions to hydrodynamic forces from distant particles become increasingly negligible (normally the most important contributions come from the region within a certain well-defined limit radius). Usually, a region around each particle within which the interactions are relevant is defined and historically many simulations were run with $32-64$ neighbour interacting particles, which are considered sufficient to obtain an accurate estimation of hydrodynamic quantities [41].

This is the strategy adopted by one of the classic Lagrangian methods Smoothed Particles Hydrodynamics (SPH) [42] [22]. The key idea behind the SPH method is the possibility to calculate the derivatives that appear in Euler equations (written in a non-conservative form (2.28)) in an effective way. Indeed, as we will soon show, it can be proved that the gradient operation become a simple sum operation exploiting the derivative of a W filter function (which can be previously calculated independently). As a consequence, the computational cost of the calculation is remarkably reduced. Before introducing the filter function W concept, we list the Euler's equations in the Lagrangian formalism (that are the equations that the SPH method integrates)

$$\begin{cases} \dfrac{D\rho}{Dt} + \rho\nabla \cdot \, \mathbf{v} = 0 & \text{Mass conservation law} \\ \rho\dfrac{D\mathbf{v}}{Dt} = -\nabla P & \text{Equation of motion} \\ \rho\dfrac{Ds}{Dt} = 0 & \text{Entropy equation} \end{cases} \tag{2.28}$$

where $\frac{D}{Dt} = \frac{\partial}{\partial t} + \mathbf{v} \cdot \nabla$ the is the Lagrangian derivative, which describes the variation of a quantity on a fluid element as the fluid moves, s is the entropy per unit mass and all the other symbols have the same meaning as in equation (2.11). The operator $\mathbf{v} \cdot \nabla$ is called advective operator and tells us that the physical quantities of the fluid elements vary (or are transported advectively) as a result of the fluid motion. Finally, we note that if equations (2.28) are discretized as a set discrete particles, both the mass conservation and the entropy equations are automatically satisfied. Therefore, only a strategy to integrate the equation of motions for each particle must be developed.

As mentioned above, SPH relies on the use of a filter function W filter also known as smoothing kernel to provide for a numerical approximantion of the pressure gradient present in the equation of motion. Typically in the context of simulations involving a high dynamic range, the smoothing kernel W is assumed to be non-zero only within a limited region bounded by a maximum distance h. In addition, to naturally preserve the total angular momentum, the kernel is usually an even function of the position:

$$W(r,h) = W(-r,h) \tag{2.29}$$

In practice, the kernel is required to be symmetric and sufficiently smooth to make it differentiable. Currently the most widely used kernels are the so-called cubic spline kernels [43], which in three dimension take the form [22]

$$W(r,h) = \frac{8}{\pi h^3} \begin{cases} 1 - 6\left(\frac{r}{h}\right)^2 + 6\left(\frac{r}{h}\right)^3 & \text{if } 0 \le \frac{r}{h} \le \frac{1}{2} \\ 2\left(1 - \frac{r}{h}\right)^3 & \text{if } \frac{1}{2} < \frac{r}{h} \le 1 \\ 0 & \text{if } \frac{r}{h} > 1 \end{cases} \tag{2.30}$$

The kernel itself, its first and second derivative are continuous (but not the third derivative) [44]. We note that this kind of kernel drops to zero at a distance of $r = h$, or in other words the most important contributions of interaction between particles come from the region within a radius of h. The latter is also called *smoothing length.* Once the kernel form has been fixed, the standard procedure of SPH is to estimate a generic gas property $A(\mathbf{r}_i) = A_i$ (for instance density, pressure gradients) at the location of the particle $\mathbf{r}_i$ as an average over the kernel in the following way

$$A_i = \sum_{j=1}^{N} \frac{m_j}{\rho_j} A_j \, W(\mathbf{r}_i - \mathbf{r}_j \, , h_i), \tag{2.31}$$

where h_i simply encodes the information that each particle has in principle its own smoothing length and $\mathbf{r_j}$ are the coordinates of the closest N neighbours of the target particle i.

Let us calculate a first fundamental property that is needed to integrate the equation of motion: the density. By placing $A = \rho$ in the previous equation, we obtain

$$\rho_i = \sum_{j=1}^{N} m_j \, W(\mathbf{r}_i - \mathbf{r}_j \,, h_i). \tag{2.32}$$

We can adopt the same technique to estimate the second property needed for the discretization of the equation of motion: the pressure gradient. In the SPH formalism this can be estimated as

$$(\nabla P)_i \; = \sum_{j=1}^{N} \frac{m_j}{\rho_j} \, P_j \, \nabla W(\mathbf{r}_i - \mathbf{r}_j \,, h_i). \tag{2.33}$$

This equation shows that it is possible to compute differential operators as a weighted sum over the derivative of the kernel function. It is now possible to evolve the system in time, provided that an estimate of the smoothing length h_i of each particle is available. This is defined implicitly by the relation

$$\frac{4\pi}{3} \rho_i h_i^3 = N\bar{m}, \tag{2.34}$$

where ρ_i is the density defined in equation (2.32), N is the number of neighbours (which can be freely chosen) and $\bar{m}$ is the average particle mass.

As a concluding remark, we would like to emphasize that in this section we have just given a rough introduction to the SPH technique. For a more extensive and rigorous derivation we refer the interested reader to [43].

2.4.2 Advantages and limitations of the standard SPH method

One of the major advantages of Lagrangian techniques is that they can fully adapt their resolution to the clustering of matter, which is a desirable properties in astrophysical applications where density contrast can be quite large. Indeed, exactly because the mass is described in terms of particles whose evolution is then followed, the bulk of resolution elements are to be found in the regions where the gas is denser automatically. As already mentioned, Eulerian codes cannot not do this automatically and the experimenter needs to set specific criteria through Adaptive Mesh Refinement techniques. Another advantage is that these methods are mesh-free and their geometric flexibility is therefore superior to codes using structured meshes. Finally, integrating a Lagrangian code with an N-body solver is easy and yields accurate results since the source of the gravitational forces correspond to the hydrodynamical resolution elements. This series of advantages explains why Lagrangian methods are so popular in Astrophysics [22] [58] [48].

On the other hand, Euler equations can produce discontinuous solution in the form of shock waves and contact discontinuities and SPH codes have difficulties in correctly describe these solutions. For examples, it can be shown that in shock waves the specific entropy of the gas always increases, whereas in the SPH formalism the entropy of a particle is kept constant. Introducing an artificial viscosity is one of the most used strategies strategies used so that shock conditions can be regularly resolved by the SPH [43] for details. However, artificial viscosity, although it helps reproducing discontinuous solutions, may be causing other issues in the modelling of contact instabilities (especially the Kelvin-Helmholtz instability, see [16]). Finally, it has also been shown that the convergence order of SPH schemes is in general lower than the Eulerian methods [16]. It is to cure these shortcomings that more sophisticated SPH techniques [48] [49] have been developed.

2.5 Combining Lagrangian and Eulerian approaches

2.5.1 The moving-mesh code AREPO

Even if they follow different approaches, Eulerian and Lagrangian methods should largely give the same results when applied to a particular problem, as the physics behind these codes remain the same. However, as highlighted in the previous sections, each one of these approaches is characterized by a particular set of advantages/disadvantages, and a peculiar type of approach can be is better suited than the other to model the specific problem at hand. Therefore, the use of a method instead of another depends essentially on the scientific problem that needs to be investigated. Indeed, the choice of a code inevitably influences the results obtained. A comparison between different approaches is very important to bring out any inaccuracies in the description of the fluid, the arising of non-physical processes due to improper modelling of the discontinuities (as evidenced in the past by works of [16] [52] [51]) and many other issues that may not best represent the real phenomena that occur in the most diverse astrophysical environments.

In the last decades different codes have been introduced to combine together the advantages of the two methods discussed and to reduce their application limits. A possible idea is to implement a new kind of unstructured and moving mesh in time, set in motion at the local velocity of the fluid flow that is able to best describe the hydrodynamic continuum of an ideal fluid. This has been done recently in some codes and generally take the name of ALE (Arbitrary Lagrangian-Eulerian) technique. One of these code is the so-called AREPO code [17] [59], which is the code used to perfom the simulations analyzed in this work in chapters 3 and 4 . We adopt this code because the moving-mesh code AREPO is able to overcome many of the weaknesses of the Lagrangian SPH method and AMR (adaptive mesh refinement) tool in the Eulerian's code that we have discussed in previous sections. These issues may negatively impact the accuracy of the results [17]. For example, from the comparison of the simulation results generated by several kind of codes, there was evidence of significant differences in the formation of cosmic structures as a result of different timescales in the cooling of the gas. This suggests that inaccuracies in hydrodynamic solvers can lead to relatively large systematic differences for the global state of cosmic structures in a simulated portion of the Universe [54].

The moving mesh approach in AREPO is defined by the Voronoi tessellation of the simulation domain that starts from a set of discrete points, the so-called "mesh-generating points" (MGP). This partition of the simulation volume provides a mesh, that is free to move according to the fluid flow and on which the Euler's equations are numerically solved via a standard, second-order Godunov's scheme [40]. To understand how the AREPO code works, it is necessary to get into details by providing generalities and basic concepts behind the idea of the moving mesh implemented in the model. In particular, it is informative to dwell on how the mesh is constructed starting from these particular MGPs, as it is from them that the grid will be built at each time step of the simulation.

As mentioned, the overall simulation volume is partitioned into sub-volumes which are structured like a Voronoi tessellation of an arbitrary set of MGPs. In particular, the Voronoi tessellation has been chosen because it has several mathematical properties useful to define how the grid can be deformed during the temporal evolution of the simulation, avoiding to generate topological defects in simulation volume. Without going into complex mathematical details, a Voronoi tessellation can be defined as that partition of the space that, for a given set of points (the MGPs), consists of non-overlapping cells around each of the points' locations such that each cell contains the region of space closer to that location than any of the other points [17]. As a direct consequence the cells thus defined are polygons in 2D and polyhedra in 3D, with faces that are equidistant to the mesh-generating points of each pair of neighbouring cells.

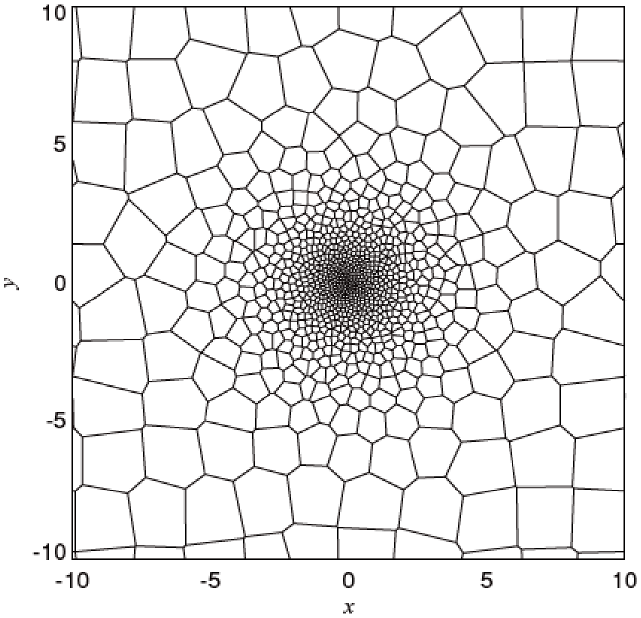

Figure 2.3: Voronoi mesh configuration once the initial conditions of a gaseous disc with an exponential gas surface density are given. The figure shows the resulting Voronoi mesh inside a periodic box of 20 units of length per side, once taken a distribution of 750 particles on a surface exponential profile placed in the center of the system and added an additional grid of 10×10 particles inside the simulation domain to represent the 'vacuum' outside the disk. In this way most of the resolution elements are placed in the exponential disk as an imposition of the initial configuration required by an experimenter. Figure was taken from [17].

In the volume that we want to simulate, the MGPs represent a distribution of points that may be purely random or may be points established by the initial conditions defined by a scientific problem. Sub-volumes (or cells) of the grid are then built starting from the distribution of these generator points into the simulated box. Indeed, the key point about a Voronoi tessellation of space is its flexibility. For example, it is possible to simulate a gaseous system that has uniform properties by distributing the MGPs on a Cartesian configuration similar to an Eulerian code. Such a configuration is actually a degenerate case of a Voronoi partition. Another example could be to define the initial configuration of a simulated disk galaxy by assuming that most of the MGPs are bound to be inside the disk, and that they will gradually decrease outside the galaxy. In Fig. 2.3 is shown a representation of how Voronoi tessellation can be configured when we want to set that most of the MGPs are placed in the center of the system, once we set an exponential profile for a disk. Other configurations are also possible (for instance simulating a representative volume of the Universe): it is sufficient to place the MGPs inside the simulation volume according to the key features of the system to be simulated.

Once a Voronoi tessellation, based on the coordinates $\mathbf{r}_i$ of the MGPs has been computed (see [17] for details), information on the centres-of-mass $\mathbf{s}_i$, on the areas of their faces $\mathbf{S}_{ij}$ (which describe the oriented area of the cell surface i which point to the adjacent cell j) and so the volumes $\mathbf{V}_{ij}$ of each cell is also available. This information, together with the fact that the simulation volume has been subdivided in a finite number of disjointed cells, can be used to discretize Euler equations (2.26) via the so-called finite volume method (see also section 2.3.1). This means that the dynamics of the fluid is described by the rate of change in time of the cell averages of conserved quantities (mass, momentum and energy) for each cell. In other words, integrating the fluid equations (2.26) over the volume V_i of cell i-th, we can calculate the total mass m_i, momentum p_i and energy E_i contained in the cell as

$$m_i = \int\limits_{V_i} \rho \, \mathrm{d}V \,, \tag{2.35}$$

$$p_i = \int\limits_{V_i} \rho \mathbf{v} \, \mathrm{d}V \,, \tag{2.36}$$

$$E_i = \int\limits_{V_i} \rho \epsilon_{tot} \, \mathrm{d}V \,. \tag{2.37}$$

From the above conserved fluid variables associated with each cell, it is possible to calculate the primitive variables $\mathbf{W}_i = (\rho_i, \, \mathbf{v}_i, \, P_i)$ of the fluid for each cell. Moreover, by using the Euler equations (2.26) and the Gauss's theorem to convert the volume integral over the flux divergence into a surface integral over the cell, it is possible to calculate the rate of change of conserved quantities in time, which is given by

$$\frac{dm_i}{dt} = -\int\limits_{S_i} \mathbf{n} \cdot [\rho\,\mathbf{v} - \rho\,\mathbf{w}]\ \mathrm{d}S\,, \tag{2.38}$$

$$\frac{dp_i}{dt} = -\int\limits_{S_i} \mathbf{n} \cdot [\rho\,\mathbf{v} \otimes \mathbf{v} + P\mathbf{I} - \rho\,\mathbf{v} \otimes \mathbf{w}]\ \mathrm{d}S\,, \tag{2.39}$$

$$\frac{dE_i}{dt} = -\int\limits_{S_i} \mathbf{n} \cdot [\rho\,\epsilon_{tot} + P\mathbf{I} - \rho\,\epsilon_{tot}\,\mathbf{w}]\ \mathrm{d}S\,. \tag{2.40}$$

The terms in square brackets are flux quantities and most of the nomenclature in these equations has already been described in section 2.2.1. Before discussing the above equations, we remember that the AREPO code implements a moving mesh, i.e. MGPs, and hence the mesh and in particular the interfaces between cells, are not fixed in time, but they can move from their initial position with velocity $\mathbf{w}_i$. As a result, the code recalculates the Voronoi cells (modifying their shapes) whenever these points move away from their position, thus also changing the orientation of the outward normal vector $\hat{n}$ of the cell surfaces and their positions. Because of the mesh motion, the hydrodynamics equations solved by AREPO differ from those used in standard Eulerian codes in the term containing the mesh velocity vector $\mathbf{w} = (w_x,\, w_y,\, w_z)$ (with which each point on the edge of the cell surface moves). Basically an additive term to the flux quantities is present in the case of mesh motion, which needs to be taken properly in account in order to correctly describe the variation of fluid dynamic quantities during the evolution of the system.

For each Voronoi cell surface, it is possible to compute the averaged flux across the face connecting cells i-j as

$$\mathbf{F}_{ij}(\rho) = \frac{1}{S_{ij}} \int\limits_{S_{ij}} \mathbf{n} \cdot [\rho\,\mathbf{v} - \rho\,\mathbf{w}]\ \mathrm{d}S_{ij}\,, \tag{2.41}$$

$$\mathbf{F}_{ij}(\rho\,\mathbf{v}) = \frac{1}{S_{ij}} \int\limits_{S_{ij}} \mathbf{n} \cdot [\rho\,\mathbf{v} \otimes \mathbf{v} + P\mathbf{I} - \rho\,\mathbf{v} \otimes \mathbf{w}]\ \mathrm{d}S_{ij}\,, \tag{2.42}$$

$$\mathbf{F}_{ij}(\rho\,\epsilon_{tot}) = \frac{1}{S_{ij}} \int\limits_{S_{ij}} \mathbf{n} \cdot [\rho\,\epsilon_{tot} + P\mathbf{I} - \rho\,\epsilon_{tot}\,\mathbf{w}]\ \mathrm{d}S_{ij}\,. \tag{2.43}$$

To evaluate the fluxes, a Godunov-like scheme is applied to obtain a second-order accuracy in space and time, and fluxes are calculated as the solutions of the Riemann

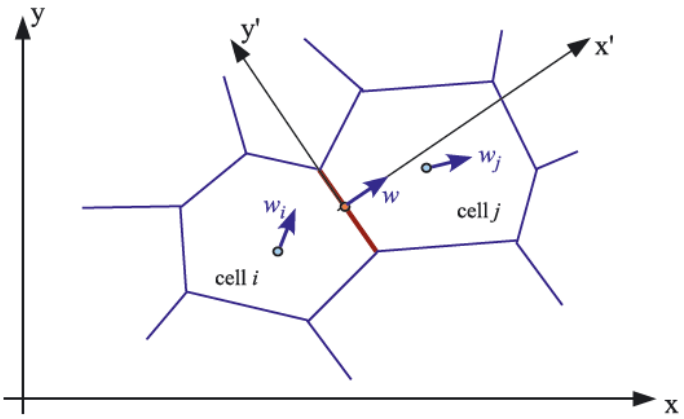

Figure 2.4: Illustrative scheme of the flux calculation between two adjacent cells whose surfaces are in contact and moves simultaneously at the velocity $\mathbf{w}$. The flux through each face is estimated on the basis of a 1D Riemann problem. The Riemann problem is solved in an appropriate reference system with the x'-axis normal to the cell surface in order to obtain a Galilean-invariant formulation, which is possible if the mesh motion is tied to the fluid flow motion. In particular, the motion of the interface $\mathbf{w}$ is specified by the velocities $\mathbf{w}_i$ and $\mathbf{w}_j$ of the MGPs within cells. Figure was taken from [17].

problem which occur at each cell interface. The code will calculate the flux for each face separately, treating it as a 1D problem, as show in Fig. 2.4. A convenient reference frame to solve 1D Riemann problem is to rotate the fluid state in a x', y', z' coordinate system, which brings with the normal velocity $\mathbf{w}$ of the cell interface in the x' direction, as show in Fig. 2.4. In particular, as explained in [17], the choice of this rotated reference frame (in which face moving with the flow) appears to be an appropriate choice to guarantee Galilean invariance, once the flux quantities have been calculated with the Riemann solver and are then converted into the lab's reference system without breaking this invariance. Finally, once the total fluxes over the cell surfaces are calculated, the conserved quantities are updated for each cell. In this way, the time step is finished and the MGPs (with their associated velocity) move in a new configuration and the iteration of the process starts again until the end of the simulation, thus describing the temporal evolution of the fluid dynamics system under study.

In addition to hydrodynamic interactions, the AREPO code is also able to calculate the gravitational force acting on a gas cell. Thanks to an hybrid tree-PM method, the gravity solver is implemented in AREPO to consider also the self-gravity of gas, which plays a key rule in galaxy formation and evolution simulations. Implementing gravity in finite-volume codes inevitably complicates computation and leads to new challenges for an accurate treatment of gas behavior during the temporal evolution of the simulation. Indeed, if we consider a gravitational field associated with gas, the conservation laws of momentum and energy in Euler's equations will be modified by considering an additive term given by $-\rho\nabla\phi$. Due to the presence of this gravitational source term, violations of energy conservation can arise when collapse problems involve gas [56]. However, an explicitly conservative formulation to include self-gravity is implemented in AREPO [17], which leads to very accurate results.

2.5.2 Advantages and disadvantages of the AREPO code

The most important concept to highlight in AREPO is the introduction of an unstructured moving mesh which is free to move with essentially the local fluid velocity during the time evolution. We have already described the numerical and algorithmic approaches implemented in the code, which exploits a combination of the Eulerian and Lagrangian approaches, thereby enhancing their advantages while at the same time reducing their limitations. For example, AREPO does not need the implementation of an artificial viscosity – as typically happens in Lagrangian SPH – and it avoids the Galilean non-invariance of the truncation error in Eulerian codes. Moreover, AREPO fully exploits both the SPH concept of points as carriers of hydrodynamic quantities (because of its moving mesh) and the concept, typical of the Eulerian approach, of a finite-volume Godunov-type discretization of Euler equations for a more accurate treatment of the conserved fluid quantities. On the contrary, since Voronoi cell are free to move, the change of shape associated to their motion can seed numerical noise (the so-called mesh noise), which, albeit small, can give rise to a loss of symmetry in test problems where such symmetry is expected (e.g. simulation of a Raleigh-Taylor instability; see [17]). However, compared to the current generation of SPH and AMR codes, AREPO is an excellent alternative numerical technique to deal with scientific problems related to astrophysics and computational cosmology.

Chapter 3

Simulating an isolated star-forming galaxy

In this chapter, we introduce the key properties of the simulation of a Milky Way-like galaxy that we have analyzed in this work. The simulated system represent a model for a galaxy evolving in isolation – i.e. no cosmological context is considered – similar to the Milky Way and has been evolved with the moving-mesh code AREPO discussed in section 2.5. The key physical processes shaping the evolution of the galaxy are star formation, which converts gas into stars and the associated feedback (mostly generated by supernova explosions), which is responsible for the ejection of gas from the main body of the galaxy into the galaxy halo, and ultimately regulates the process of star formation. In particular, we will focus on the description of the set-up (Sec. 3.1) and of the physical model for galaxy formation and evolution that has been used to perform the simulation (Sec. 3.2), motivating the choice of the initial conditions, the feedback processes considered and the assumptions made to set all the parameters of the system that characterize our simulation (Sec. 3.3). This idealized galaxy simulation is able to capture the properties of the outflow/inflow gas cycle at the interface between the galaxy and its halo during the temporal evolution of the galactic system (Sec. 3.4), which is the main topic of this thesis.

3.1 Numerical set-up of the simulated galaxy

The simulation analyzed in this work models the temporal evolution of the gravitational and hydrodynamic properties of an isolated late-type galaxy similar to the Milky Way within a Dark Matter (DM) halo. For efficiency reasons, the DM halo is represented as a static gravitational field that is not influenced by the dynamics of the galaxy system. It is worth mention that the choice of a static potential represents a limitation of this particular simulation, because the DM halo cannot respond to the presence of the other galactic components (and in particular to the variation of gas properties such as the mass contained in the central regions). However this would only marginally influence the properties of the gas in which we are interested in this work [18].

The DM gravitational influence is modelled by an Hernquist [60] potential of the form

$$\phi_{DM}(r) = -\frac{G\,M_{DM}}{r+a}\,, \tag{3.1}$$

where M_{DM} is the total mass of the DM halo and a is a characteristic scale length of the system. It can be easily shown that the potential $\phi(r)$ can be derived, and it is found by integrating Poisson's equation (2.2) considering the following density profile

$$\rho_{DM}(r) = \frac{M_{DM}}{2\pi}\frac{a}{r(r+a)^3}\,. \tag{3.2}$$

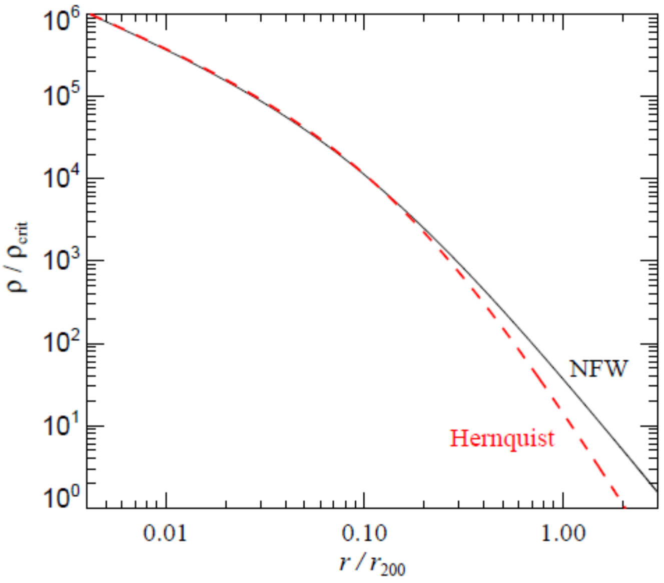

Figure 3.1: Trend of Hernquist and NFW density profiles for a DM halo with the same total mass within the virial radius r_{200} and the same concentration index $c = 10$, combined together as explained in the treatment of this thesis. In particular the choice of parameters reported in [19], is such as to return a scale length $a \simeq 1.73\, r_s$ so that the Hernquist model contains 99% of its total mass within $1.1\, r_{200}$. One can easily see that in the inner parts of the halo the two mass distributions coincide quite well, whereas in the outer regions the density profiles decline asymptotically as $\rho_{Hern} \propto r^{-4}$ and $\rho_{NFW} \propto r^{-3}$. Figure was taken from [19].

Although cosmological N-body simulations have convincingly shown that dark matter halos follow a Navarro, Frenk and White (NFW, [61]) profile, in many contexts it is convenient to use an Hernquist profile because, unlike the NFW, is characterized by components that have analytical distribution functions. In the case of our simulation, the Hernquist profile is connected to a NFW-halo with the same DM mass within a virial radius of r_{200}, or the radius within which the average density of dark matter is 200 times the critical density of the Universe. In fact, as shown in Fig. 3.1, the trend of these two density profiles agrees in the inner parts if we impose the condition $\rho_{DM} = \rho_{NFW}$ for small radii (or $r \ll r_{200}$). As a direct consequence there is the a relationship between the a scale length and the r_s scale length characteristic of the NFW profile

$$a = r_s \sqrt{2 \left[\ln(1+c) - \frac{c}{1+c} \right]} \tag{3.3}$$

where c is the halo concentration parameter commonly defined as $c = \frac{r_{200}}{r_s}$. We use this relationship to set the properties of the Hernquist DM halo adopted in the simulation given the virial mass and the concentration parameter of the corresponding NFW halo.

From the point of view of the baryonic matter, the galaxy model consists of the following components for stars and gas:

(I) A spherical stellar bulge, which is model with a Hernquist profile

$$\rho_b(r) = \frac{M_b}{2\pi} \frac{b}{(r\, +\, b)^3} \tag{3.4}$$

where the bulge scale length b is described as a free parameter in units of the disk scale length and the bulge mass $M_b = m_b\, M_{tot}$ as a fraction m_b (dimensionless) of the total mass of the galaxy. In particular, we note that the bulge is taken to be completely stellar.

(II) A stellar disk and a gaseous disk which follow different exponential surface density profiles along the radial direction as

$$\Sigma_{gas}(R) = \frac{M_{gas}}{2\pi\, r_g^2}\ \exp\left(-\frac{R}{r_g}\right)\,, \tag{3.5}$$

$$\Sigma_\star(R) = \frac{M_\star}{2\pi\, r_d^2}\ \exp\left(-\frac{R}{r_d}\right)\,, \tag{3.6}$$

where r_d (r_g) is a characteristic radial scale length of the stellar (gaseous) disk, $M_\star$ (M_{gas}) is the total mass of the stellar (gaseous) disk and $M_d = M_{gas} + M_\star = m_d\, M_{tot}$, with m_d a dimensionless number. The vertical density distribution of the stellar disk follows a hyperbolic secant distribution on the z direction, so that the volumetric stellar density of the disk is given by

$$\rho_\star(R,z) = \frac{M_\star}{4\pi z_0\, r_d^2}\ \mathrm{sech}^2\left(\frac{z}{z_0}\right) \exp\left(-\frac{R}{r_d}\right) \tag{3.7}$$

that is the profile of an isothermal sheet with radially constant scale height z_0 (see [19]). The latter is treated as a free parameter of the model since it directly determines the temperature of the galactic disk, setting the velocity distribution of the stars in a self-consistent manner. Typically one assumes that $z_0 = 0.1 - 0.2\, r_d$. On the other hand, the vertical profile of the gas is determined by imposing the hydrostatic equilibrium in the vertical direction and assuming an initial gas temperature of $10^4\,\mathrm{K}$

$$-\frac{1}{\rho_{gas}} \frac{\partial P}{\partial z} - \frac{\partial \phi_{tot}}{\partial z} = 0\,, \tag{3.8}$$

where ϕ is the total gravitational potential (stars, gas and DM), P is the gas pressure and ρ_{gas} the gas density. At each radius R the gas density must satisfy the requirement

$$\Sigma_{gas}(R) = \int_{-\infty}^{+\infty} \rho_{gas}(R,z)\,\mathrm{d}z\,, \tag{3.9}$$

where $\Sigma_{gas}(R)$ is given by equation (3.5). An expression for ϕ_{tot} is not known *a priori* because the gas distribution, and therefore its contribution to the total potential, is not available. For this reason, the equations (3.8) and (3.9) are solved by using an iterative method that seeks to determine the gravitational potential and a resulting vertical structure of gas self-consistently. We refer the interested reader to [19] for details on this procedure.

Finally, the density distributions of the stellar disk and the bulge (which are approximately in virial equilibrium with each other) are discretized by sampling their density distribution with a set of non-collisional particles whose dynamics is determined solely by gravity. We will refer to those as "star particles" (see also section 3.2). The evolution of the gas component (initially in hydrostatic equilibrium) instead, is simulated by the AREPO code with a moving mesh, as discussed in the section 2.5. Each cell composing the mesh will be referred to as a "gas cell".

3.2 Structural parameters of the model

The simulated galaxy and its dark matter halo are contained in a simulation domain represented by a cube of side length of about 600 kpc. More specifically, the stellar disc, the gaseous disc and the dark matter halo have a size (in diameter) of approximately 30 kpc, 60 kpc and 460 kpc, respectively[1]. Therefore the choice of a 600 kpc side box is a conservative one that comfortably fits all the components of the simulated system and also gives extra room to the gas leaving it enough space to expand, if need be, without losing any mass outside the simulation domain boundaries. From the point of view of the temporal evolution of the system, the simulations is run for a time interval of ~ 1 Gyr. The output is saved in 150 snapshots that are evenly spaced in time (namely, every snapshot covers ~ 7 Myrs of the simulation). The structural parameters of the galaxy model are: the halo concentration index $c = 12$, the bulge scale length $b = 1$ kpc, the stellar disk scale length $r_d = 3$ kpc, the stellar disk scale height $h_d = 0.3$ kpc and the gas disk scale length $r_g = 6$ kpc. To conclude the description of the initial conditions of the simulation, we note that the galaxy at the beginning of the simulation is composed, in terms of mass, by 90% of stars and the remaining 10% of

---

[1] The estimate for the diameter of the DM halo is derived using the value of its virial radius $r_{200} = 230$ kpc, whereas for the star and gas discs we considered 5 times their radial scale length.

$M_{tot}\,(M_\odot)$	$M_{halo}\,(M_\odot)$	$M_{bar}\,(M_\odot)$	$M_{bulge}\,(M_\odot)$	$M_{\star\,disk}\,(M_\odot)$	$M_{gas\,disk}\,(M_\odot)$
1.60×10^{12}	1.53×10^{12}	7.10×10^{10}	1.50×10^{10}	4.73×10^{10}	9×10^{9}

Table 3.1: The table shows a list of the MW-like mass components of the galaxy implemented at the beginning of the simulation that we used. In sequence order from left to right we have: the total mass of the galactic system (M_{tot}) including baryonic matter and dark matter, mass of the DM halo surrounding the galaxy (M_{halo}), baryonic mass (M_{bar}), bulge mass (M_b), stellar disk mass ($M_{\star\,disk}$), and gas disk mass ($M_{gas\,disk}$).

gas at an average temperature of $T = 10^4\,\mathrm{K}$. The galaxy is then surrounded by a very-low density ($\lesssim 10^{-3}\,cm^{-3}$) gaseous atmosphere (see [18]) at relatively high temperature ($\sim\, 10^5 - 10^6\,K$). However, this tenuous hot gas component has a negligible global contribution in terms of mass ($\simeq 0.1\%$). In particular, this phase component of gas is inserted in the initial configuration in order to avoid vacuum boundary conditions.

To better summarize the properties of the simulated galaxy that we analyze in this thesis, we report the values of all its mass components in Table 3.1. In particular, the simulation analyzed presents a mass resolution of $\sim\, 10^5 M_\odot$ and a maximum spatial resolution of approximately $\sim\, 20\,pc$. Therefore, it is not possible to resolve the individual stars of the galaxy system. This represents a limitation strictly related to the available spatial and mass resolution, which, however, requires a specific implementation of physical phenomena, such as star formation and feedback, that occurs below the resolution scale of the simulation (see section 3.3). Given the masses of the components that constitute the galaxy (see Table 3.1), the quoted value of mass resolution corresponds to $N_{bulge} = 8 \times 10^5$ star particles in the bulge, $N_{disc} = 3.2 \times 10^6$ stellar particles in the stellar disk and $N_{gas} = 8 \times 10^5$ for the gas cells in the gaseous disk. There are other two resolution levels available: a high resolution level that has a mass target for particles of a factor of 8 less than the resolution level that we considered and a low resolution level in which the target mass is 8 times larger (see for details [18]). We chose to work with the intermediate resolution level for practical purposes as it offers the best compromise between the speed of analysis and the physical fidelity of simulations. However, the same analysis pipeline that we have developed for this thesis can be applied also to the all resolution level. This is an avenue that we intend to pursue in future work.

Similarly to what is shown in Fig. 2.3, most of the resolution elements are present in the galactic disk, while the outer cells in the halo become progressively coarser, so that the resolution in these regions is inevitably lower. AREPO is a pseudo-Lagrangian code, which attempts to discretize the fluid in cells of approximately equal mass[2]. As a consequence the most dense regions are always better spatially resolved. Along the sides of the simulated box there are only 16 low-density gas cells per side [18].

As we will explain in detail later in the discussion (in particular in the next section 3.3), at the beginning of the simulation the gas in the disk is set to solar metallicity $Z_{\odot} = 0.0127$ (see [65]). Around the galactic disk, instead, gas is very tenuous ($\rho \lesssim 10^{-3}\, cm^{-3}$) and has zero metallicity. Therefore, during the temporal evolution of the system any phenomenon that generates a gas outflow from the galactic disk pushes this gas outside of the disk and the ejected gas meets with very little resistance from the surrounding medium. This is due to the fact that our simulation does basically not include any hot halo gas (also known as a galactic corona) in the initial conditions. This shortcoming of the simulation will be addressed in future work. Given the difference in metallicity, the release of this gas into the halo is similar to a "coloured smoke" that, when mixed with the surrounding medium, enriches it with metals that are present in the star-forming disc.

Starting from these initial conditions, the gas in the galaxy begins to cool down until stars are formed and those more massive than a specific threshold (established by the chosen IMF) explode as SNII (see section 3.3). These explosions generate a gas circulation between the disk and the halo. This gas cycle continues until the fuel for star formation is either completely exhausted or most of the gas is ejected from the disk plane.

We would like to note again that the initial conditions of the simulations are idealized and that, in particular, the galaxy employs a few some dynamical time before it settles to normal behaviour. Furthermore, the effects of SNII are visible only after about 40 Myrs from the beginning of the simulation, because the star particle that are present in initial condition are assumed to be a relatively "old" (age $\gg 40\,$Myrs) stellar population that does not contribute any supernova events. Therefore, new stars need to form and some times has to elapse before SN explosions are occurring. This is shown in Fig. 3.2. The image at time $t = 0.00$ Gyr (top left panel) of the simulation reflects the initial conditions discussed in this section and in section 3.1, and we highlight the exponential

---

[2] Because the flux exchange between cell, their mass cannot be kept at a constant value. However, AREPO has a refinement-derefinement procedure that splits (merges) cells if they are above (below) twice (half) a predetermined target mass value.

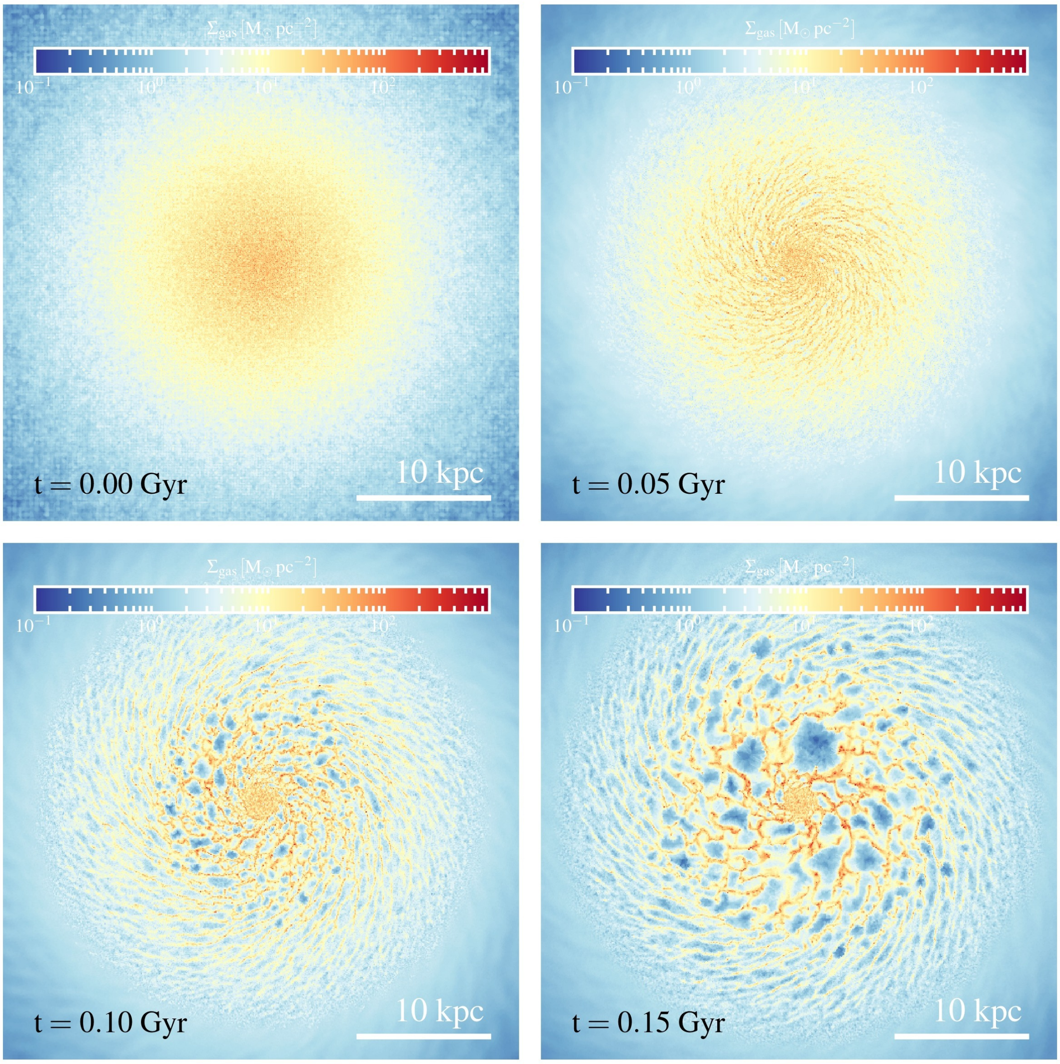

Figure 3.2: Projections of the gas column density Σ_{gas} (in units of $\mathrm{M}_\odot\,\mathrm{pc}^{-2}$) for the simulated MW-like galaxy in a face-on visualization. These projections, with an image size of to 40×40 kpc, have been computed at time $t = 0.00, 0.05, 0.10, 0.15$ Gyr. In particular, between one image and another (from left to right column) there is an interval of time of $\sim$ 0.05 Gyr. From the image on the top left to the last one on the bottom right, we can see how the gas distribution, after an initial cooling phase, varies as a consequence of the birth of the first stellar particles and the evident formation of cavities of low density gas "dug" by the SN explosions and the action of radiation feedback.

surface density profiles of the gaseous disk along the radial direction. As the simulation time progresses, the galaxy takes on a more spiral shape and the structure of the ISM becomes more complex. The spiral pattern of the gaseous disc, where the density is higher, represents the regions in which the generation of the first stars tends to occur. In fact, a denser gas network ($\Sigma_{gas} > 10$ M$_\odot$ pc^{-2}, colors tending to red) stands out over the entire diameter of the galaxy and less dense regions ($\Sigma_{gas} > 10$ M$_\odot$ pc^{-2}, colors tending to blue) become evident, indicating that several SN explosions occurred and swept away the gas (see also Fig. 3.3 for an edge-on visualization of the galaxy) generating cavities with the aid of radiative feedback action. We point out that the cold gas expelled from the disk by these combined mechanisms, requires a time of the order of 100 Myrs to exit and re-enter inside the galaxy (see [18]).

In the next section we will discuss in more detail the model used to describe the various physical processes occurring in the gaseous and stellar components of the galaxy. In particular, we will focus on the feedback channels implemented in the simulation and on the star formation treatment and the energy-momentum coupling between SN events and the ISM.

3.3 Galaxy formation physics: the SMUGGLE model

As previously mentioned, the simulation analyzed in this thesis models a galaxy similar to the Milky Way in isolation conditions, thus neglecting the cosmological context. This approximation was made in order to simplify the complex process of galaxy formation and evolution and make it possible to test the key components of the new local model for star formation and feedback channels developed for AREPO, the so-called SMUGGLE (Stars and MUltiphase Gas in GaLaxiEs) model presented in [18].

In fact, to describe the evolution of this isolated galaxy (and of galaxies in general), it is necessary to consider (in addition to implementations related to gravity and hydrodynamics) physical processes that play a major role in galaxy formation such as, for example, gas radiative cooling, star formation and the associated feedback effects that determine the evolutionary trend of the simulated galaxy.

These aspects are covered in depth by the SMUGGLE model, which numerically implements a number of key physical processes that actively participate in modeling the shape of the galaxy. This state-of-the-art model is able to treat stellar feedback at the local level, thus naturally and self-consistently generating gas outflow phenomena and producing a distinct multiphase structure in the ISM gas.

In particular, the SMUGGLE model adopts effective prescriptions for stellar feedback, such as SN explosions, AGB and OB stellar winds, and radiation pressure from young OB stars (copious sources of ionising radiation that are also important regulators of star formation and gas properties inside and outside the galaxy).
In the simulation that we consider in this thesis, we have that SN explosions represent the dominant feedback channel of energy and momentum injection to the ISM. For this reason, it is worth noting that SN explosions represent the primary sources of gas outflows on a galactic scale. Since the SMUGGLE model is quite articulated, in this section we will only discuss in depth the most important feedback channel – i.e. supernovae – and mention the other feedback channels only briefly. For a complete description of the model we refer the interested reader to [18].

In the configuration of the model used to perform the simulation that we investigate, also the feedback related to stellar winds has been taken into account. In particular, massive short-lived OB stars and older population as AGB stars are the two classes considered to contribute to the stellar wind feedback channel. This channel (and in particular OB stars) assumes the important function of pre-processing the gas around SN progenitors, thus increasing the overall SN feedback efficiency. In addition, the mass released by the winds returning to the ISM helps to fuel the galaxy for potential new star formation episodes.

Moreover, heating/cooling processes (which modify the thermal state of gas) are considered in SMUGGLE as well. These are phenomena generated by several sources[3] that are included in the model. In addition, the heating processes due to Cosmic Rays (CRs) and photoelectric effect (i.e. emission of electrons from dust grains interacting with the interstellar radiation field (see also [18], [93])) are also included, albeit in an approximated manner. These two heating processes regulate the thermal balance and

---

[3] In particular the model takes into account: collisional excitation, collisional ionization, dielectric recombination, free-free emission, Compton cooling off CMB photons, and photoionization from a spatial-uniform UV background, that is two-body processes related to hydrogen and helium interactions. Furthermore, metal cooling is added to the previous cooling network as a function of temperature and gas density as described in [64].

stability of the cold ($\sim$ 50 K) and warm ($\sim$ 8000 K) ISM phases. Finally, also the cooling processes for molecular gas phase, fine-structure, and low-temperature metal lines are considered. These processes are indeed necessary to obtain high density ($\sim 10^2 - 10^3\,\mathrm{cm}^{-3}$) and low-temperature ($\sim$ 10 K) gas that has the right physical conditions to be eligible to form stars (see equation (3.10) below).

To efficiently simulate this idealized galaxy, keeping the implemented parameters under control as much as possible, our simulation do not include some physical phenomena that might be relevant for the dynamics of the ISM interactions (see [18]). In particular, the model does not include: a treatement for magnetic fields, the photoionization of gas by old stars, the dynamic cosmic rays (CRs) and its effects on the gas. Also, the resolution achieved in the simulations is not suitable to model the Sedov-Taylor phase of supernova explosions, which therefore has to be modelled in a sub-grid fashion (more details are given toward the end of the section). Moreover, the SMUGGLE model does not also include a self-consistent treatment of radiation transport and dust physics. In particular, to capture the global evolution of these phenomena, the code does not solve the equation of radiative transport, but its effects are inserted in a stochastic or approximated manner. We do not give details on the approximate treatment of radiation transport (see [18] for details), as the focus of this thesis is on the study of the effects of SN feedback.

We point out that, in the simulation analyzed in this thesis consider, SN feedback release into the ISM an amount of momentum that is $\gtrsim 10$ times greater than the other two feedback channels (stellar winds and radiative feedback) which, on the contrary, have a comparable efficiency. In other words, although all feedback channels considered in the SMUGGLE model are included and play a role in the regulation of important phenomena such as the star formation within the galaxy, the dominant channel for the injection of momentum and responsible for generation of gas outflows – the key focus of this thesis – is SN feedback.

To better understand how the SMUGGLE model simulate the different components of the galaxy system, we introduce the definitions of gas cell and star particle:

1. A gas cell represent a volume element of the Voronoi tesselation (see section 2.5) that identifies the temporal evolution of the physical properties of a gas distribution (with a given mass, density, temperature, etc.). All the gas cells constitute

the unstructured moving mesh implemented in the AREPO code to describe the hydrodynamic continuum of gas. The cell surfaces are placed in contact and can be deformed by the movement of the "mesh generating points", which also change the physical properties of gas. Moreover (under certain specific conditions that will be discussed later) some cold dense gas cells can be converted by a probabilistic approach into new star particles during the temporal evolution of the system.

2. A single star particle, because of the mass resolution that can be achieved in this galactic-scale simulations, represent a cluster of discrete stars all born at the same instant of time t_0, that is a single-age stellar population or a so-called Simple Stellar Population (SSP). The physical variables attached at these new stellar population evolve over time, according to the standard models of stellar evolution. They may be implemented at the beginning of the simulation to describe the gravitational component of bulge and disk (the ones implemented in this way are simply collisionless particles that only feel gravity and, as such, will not evolve from the point of view of stellar evolution and therefore not produce any SN events or mass return to the ISM) or rather they may arise from a stochastic process related to the conversion of a gas cell into a star particle. The particles generated in this way represent a new stellar population born entirely in the same burst and are described by a Chabrier [21] Initial Mass Function (IMF). As we will show shortly these particles, following their stellar evolutionary path, are a source of mass, metals, energy, and momentum for the ISM (especially via SN explosions).

This distinction is important because star particles and gas cells represent the key components of the simulation analyzed in this work. These components interact via different physical mechanisms – including the possible conversion of a gas cell (at high density and low temperatures) into a new star particle– that will be detailed in the remaining part of this section. Indeed, it is their mutual interaction that determines the evolution of the properties of the simulated galaxy.

In the SMUGGLE model, these new star particles are generated stochastically according to the probability deduced from the star formation rate $dM_\star/dt$ of each gas cell calculated as

$$\frac{dM_\star}{dt} = \begin{cases} 0 & \text{if } \rho < \rho_{th} \\ \epsilon \, \dfrac{M_{gas}}{t_{dyn}} & \text{if } \rho \geq \rho_{th} \end{cases} \tag{3.10}$$

where ϵ is a factor related to the stellar mass gas to stellar mass conversion efficiency set at 0.01 (according to observational studies of [63]), ρ_{th} represents the threshold value of the gas density above which gravitational collapse is allowed set to $100\,\mathrm{cm}^{-3}$, and M_{gas} is the gas mass, while on the other side t_{dyn} is the gravitational dynamical time associated with each gas cell in the system expressed as

$$t_{dyn} = \sqrt{\frac{3\pi}{32\,G\rho_{gas}}}\,, \tag{3.11}$$

where G and ρ_{gas} indicating the universal gravitation constant and the gas density, respectively. In addition, as described in [18], a specific criterion is used to limit stellar formation only in those regions of gas that are gravitationally bound. Basically the conversion of gas cells into stellar particles occurs only when the virial parameter of a given gas cell $\alpha < 1$, i.e. when gravity prevails over the stabilizing effect of gas pressure and turbulence.

Once $dM_\star/dt$ has been determined via equation (3.10), the star mass that would be resulted in a specific time-step Δt by the cell i is given by

$$M_{\star,i} = M_{gas,i}\left[\exp\left(-\frac{\dot{M}_\star\,\Delta t}{M_{gas,i}}\right)\right]\,, \tag{3.12}$$

in which $M_{gas,i}$ is the gas mass in the cell i and the term within square brackets $p = \left[\exp\left(-\frac{\dot{M}_\star\,\Delta t}{M_{gas,i}}\right)\right]$, represents the gas mass fraction of the i cell that would be converted into a collisionless star particle. The previous equation would lead to a continuous stellar mass formation, but to regulate this conversion, a probabilistic approach (consistent with the local SFR) is used. A uniformly distributed (pseudo-)random deviate $p^\star$ in a range $[0, 1]$ is extracted and compared with the term p, so that a cell is converted into a particle if the $p < p^\star$ condition is satisfied. This procedure (which is the standard approach in AREPO [64]) ensures that all new stellar particles inherit the mass and the phase-space variables of the converted gas cell.

Once the conversion from cell to particle has occurred, these newly-formed stars evolve as a simple stellar population described by a specific IMF (a Chabrier IMF in our case), with a certain probability of type-II explosions associated to each of them. In other words, another stochastic approach is used to determine the SN explosion rates of these stellar particles.

The explosion rate is determined by our choices of: the IMF, the average life time of these stars (as predicted by the standard models of stellar evolution) and last but not least, that only stars above the $8\,\mathrm{M}_\odot$ explode as SNII core-collapse. We point out that other choices of these parameters are possible and this has a direct consequence on: the number of SNs that can explode in a star particle, the total mass returned to the ISM [69] through the relative fraction of stars at the high and low mass ends, and therefore on the energy input released into the ISM which in turn influence the star formation rate. However, a different choice of the IMF can be trivially accommodated by the model [64]. Finally, the new stellar particles also incorporate rarer events such as SNIa that will add to the effects generated by SNII.

In practice, to determine the expected number of supernova II events in a given time step, we integrate the Chabrier (2001) IMF $\mathbf{\Phi}(M)$ over a chosen range of masses between 8 $\mathrm{M}_\odot$ and 100 $\mathrm{M}_\odot$ as

$$N_{SNII}(t, \Delta t) = M_\star \int_{M(t+\Delta t)}^{M(t)} \mathbf{\Phi}(m)\,\mathrm{d}m \;=\; M_\star \int_{8M_\odot}^{100M_\odot} \mathbf{\Phi}(m)\,\mathrm{d}m\,, \tag{3.13}$$

where $M_\star$ represents the mass of the star particle at birth (as shown in equation 3.12) and $M(t)$ is the mass of a star that exits the main sequence phase at an age t (as determined by stellar evolutionary models of [66]).

The same reasoning cannot be followed for the calculation of the number of SNIa events, as currently there is no model able to accurately predict the eventuality associated with a progenitor star of such event. Moreover, the time delay between the birth of a star in an SSP and its possible eventual explosion as SNIa remains highly uncertain. However, a temporal parametrization of the SNIa distribution is possible using a Delay Time Distribution (DTD) to determine the expected number of SNIa explosion over a time step Δt for a generic age $t > t_0$ of a star particle, as

$$N_{SNIa}(t, \Delta t) = \int_{t}^{t+\Delta t} DTD(t')\,\mathrm{d}t'\,. \tag{3.14}$$

The choice of the form of the DTD adopted in our simulation is explained in [18] (see also [70]). In particular, the DTD specifies that for stellar ages less than $t_0 \sim 40$ Myrs there are no type-Ia SN events, whereas once a SSP particle is born, all the stars above the $8\,\mathrm{M}_\odot$ explode as SNII in a time less than 40 Myrs. The temporal separation between the two possible SN channels is an important distinction that discriminates between the two types of supernova events. Equations (3.13) and (3.14) represent the expected number of SNII and SNIa over a time step, and are used to sample the number of SN explosions in a discrete way as follows. In particular, it is assumed that SN events follow a Poisson distribution

$$p\,(n;\lambda) = \frac{\lambda^n e^{-\lambda}}{n!}\,, \tag{3.15}$$

in which p represents the probability distribution of obtaining n SN events given an expected value λ of SNII (equation (3.13)) or SNIa (equation (3.14)) in a time-step Δt. In particular, the number of SNe of both types is determined by chosen the stellar evolutionary model and sampling the Poisson distribution (equation (3.15); see [18] for details) stochastically.

A key element of the SMUGGLE model is certainly how the energy and momentum released by the SNs are coupled to the ISM. Indeed, in SMUGGLE this source of energy and momentum represents the most influential feedback channel in the simulated galaxy, as a fundamental regulator of star formation, of the resulting ISM structure [99], and of the generation of gas outflows on a galactic-scale [72]. To model this feedback channel in SMUGGLE it is assumed that the total energy injected into the ISM from a single SN explosion (E_{SN}) is a fraction f_{SN} of the canonical value ($E_{51} = 10^{51}$ erg), that is

$$E_{SN} = f_{SN}\,E_{51}\,, \tag{3.16}$$

where the default value of the $f_{SN} = 1$. Furthermore, the momentum p_{SN} released into the ISM through the blast wave at explosion is given by

$$p_{SN} = M_{SN}\,v_{SN} = M_{SN}\sqrt{\frac{2E_{SN}}{M_{SN}}} = \sqrt{2E_{SN}M_{SN}}\,, \tag{3.17}$$

where v_{SN} is the blast wave velocity at the moment of the explosion, and M_{SN} represent the mass ejected per SN event. We point out that for each time step Δt of the simulation, multiple SN explosions may occur in the same stellar particle, albeit at the resolution of the simulations that we analyze in this work this is a rare occurrence. However, to trace the correct amount of energy and momentum injected overall at each time step Δt by each star particles, the total energy ($E_{SN,tot}$) and momentum ($p_{SN,tot}$) are defined as

$$E_{SN,tot} = f_{SN}\,E_{51}\,(N_{SNII} + N_{SNIa})\,, \tag{3.18}$$

and

$$\begin{aligned} p_{SN,tot} &= p_{SNII,tot} + p_{SNIa,tot} = \\ &= \sqrt{2\, N_{SNII}\, E_{SN}\, M_{SNII,tot}} + \sqrt{2\, N_{SNIa}\, E_{SN}\, M_{SNIa,tot}}\,, \end{aligned} \tag{3.19}$$

where the expected number of type-II SN events (N_{SNII}) and type-Ia (N_{SNIa}) events per time-step were previously expressed by equations (3.13) and (3.14), whereas the actual number is found by sampling the Poissonian distribution in equation (3.15), since SNe are sampled as generating from this kind of distribution in SMUGGLE model (see [18]). In equation (3.19), $M_{SNII,tot}$ and $M_{SNIa,tot}$ represent the total ejected mass associated with these SN events. The expected value of the SN ejecta mass and is found by integrating over the chosen IMF $\boldsymbol{\Phi(M)}$, i.e.

$$M_{SNII,tot} = M_\star \int_{M(t+\Delta t)}^{M(t)} M(t)\, f_{rec}(m, Z)\, \boldsymbol{\Phi}(m)\, \mathrm{d}m\,, \tag{3.20}$$

while the expected value of the SN ejecta mass is

$$M_{SNIa,tot} = M_{SNIa}\, N_{SNIa}\,. \tag{3.21}$$

In equation (3.20), $M_\star$ is the mass of the star particle at birth (see equation 3.12), $M(t)$ represents the mass of a star leaving the main sequence phase at an age t, and $f_{rec}(M, Z)$ is the the amount of mass returned to the ISM by stellar evolution. In particular $f_{rec}(M, Z)$ strictly depends on stellar mass and associated metallicity, as discussed in [66]. Instead, in equation (3.21) we have that M_{SNIa} is the ejected mass of each SNIa, which is assumed to be same for each type Ia event ($\simeq 1.37\,\mathrm{M}_\odot\,\mathrm{SN}^{-1}$) [67]. These expected values for the mass return are then divided by the expected value of supernova events for each type given by equations (3.13) and (3.14), and again multiplied by the *actual* value of SN events determined by stochastically sampling the Poisson distribution (3.15) as described above.

The key difficulty related to modelling SN feedback, in simulations where only limited spatial resolution is affordable, is to properly estimate the amount of energy that gets radiated away from this channel (and the associated momentum that will be released into the ISM) as kinetic energy during the SuperNova Remanant (SNR) expansion phase. This energy subdivision is roughly set stage at the end of the so-called Sedov-Taylor phase, in which the supernova remnant transition from an energy conserving to a momentum conserving phase in its evolution. In particular, the final amount of momentum (which is in the end responsible for the generation of galactic outflows) that is imparted to the gas is set once this transition occurs. To give an idea of the spatial scales that need to be resolved to properly model SNR evolution, we remind that the age and radius typically reached by the total lifetime of a SNR expansion are of the order of $\sim 10^6$ yr and ≤ 100 pc, respectively. However, the Sedov-Taylor phase ends in a shorter timescale, which is of the order of $\sim 10^4$ yr with a typical (so-called) cooling radius of ~ 28 pc (see [73] and [74]).

As mentioned at the beginning of this section, the SMUGGLE model does not explicitly resolve this characteristic expansion phase of the SNR, i.e. the Sedov-Taylor phase. To overcome this limitation the model implements a local treatment of energy and momentum injection in the ISM gas by feedback from SN, in such a way to generate gas outflows in a self-consistent manner. The Sedov-Taylor phase (from now on STp) implies an adiabatic evolution in which the energy released by the supernova ($\simeq 10^{51}$ erg) is approximately in equi-partition between the kinetic and internal energy of the ISM affected by the explosion. This energy-conserving expansion phase ends when the gas temperature reaches $\sim 10^6$ K and radiative losses cannot anymore be neglected. At this stage the expected radius r_{cool} reached by the SN remnant is (see [75])

$$r_{cool} = 28.4 \; E_{51}^{\frac{2}{7}} \; \langle n \rangle^{-\frac{3}{7}} \, f(Z) \;\; \text{pc} \, , \tag{3.22}$$

where n represent the average gas density within r_{cool} in units of cm^{-3}, E_{51} has been defined in equation (3.16), and $f(Z)$ is a function of the metallicity of the gas and is defined as

$$f(Z) \; = \; \min \left[\left(\frac{\langle Z \rangle}{Z_{\odot}} \right)^{-0.14} \; , \; 2 \right] \; = \; \min \left[\left(\frac{\langle Z \rangle}{0.0127} \right)^{-0.14} \; , \; 2 \right] . \tag{3.23}$$

In the previous equation $\langle Z \rangle$ is the average gas metallicity around the star particle and a value $Z_{\odot} = 0.0127$ has been used for solar metallicity [18]. For typical value of gas properties in the ISM $r_{cool} \sim 10$ pc and it is therefore very close to the resolution limit of the simulation. In other words, the mass/energy of the SN is usually injected into the ISM on scales bigger than the characteristic cooling radius of STp. Then, it is necessary to consider the amount of momentum generated by the hot ($\sim 10^6$ K) post-shocked ISM gas at the end of this adiabatic expansion phase in order to inject the correct amount of momentum in the ISM gas.

To understand how to explicitly account for this momentum, which represents one of the most important key concept of the model, it is necessary to explain how SN energy and momentum are imparted to nearest gas cells. In the SMUGGLE model this is accomplished by computing the momentum given to each gas cell (i) involved by a SN event as

$$\Delta p_i \,=\, \tilde{w}_i \,\min\left[p_{SN,tot}\sqrt{1+\frac{m_i}{\Delta m_i}}\;,\; p_t\right]\,, \tag{3.24}$$

in which $\tilde{w}_i$ is a weight function partitioning the energy and momentum released among gaseous cells, m_i represents the gas mass of the i cell, $\Delta m_i = \tilde{w}_i\,(M_{SNII,tot} + M_{SNIa,tot})$ (see equation (3.20) and (3.21)), and p_t is called terminal momentum value and represent the maximum amount of the momentum imparted to the gas by the SN shock wave at the radius r_{cool} (see equation (3.22)), or, in other words, when the transition among the STp (energy-conserving phase) and the radiative phase (momentum-conserving phase) for the blast wave occurs. In particular, p_t for each individual SN blast event is defined as (see also [89])

$$p_t \,=\, 4.8\times 10^5\; E_{SN,tot}^{0.92}\left(\frac{\langle n_H\rangle}{1\,\mathrm{cm}^{-3}}\right)^{-\frac{1}{7}} f(Z)^{\frac{3}{2}}\;\;\mathrm{M}_{\odot}\,\mathrm{km\,s}^{-1}. \tag{3.25}$$

In the above equation, $E_{SN,tot}$ is the total SN energy (as defined in equation (3.18)), $f(Z)$ is the metallicity function defined in equation (3.23), and $\langle n_H\rangle$ is the local gas hydrogen number density around the star particle. This quantity is determined in a SPH-like fashion as discussed in section 2.4.1.

The smoothing length (i.e. the feedback coupling radius, see below) of each star particle is determined by computing an effective number of neighbouring gas cells N_{ngb} that is given by

$$N_{ngb} \,=\, \frac{4\pi}{3}\,h^3\sum_i W(|r_i - r_s|\,,\,h)\,. \tag{3.26}$$

In equation (3.26) $N_{ngb} = 64$ is a pre-set (in principle arbitrary) value for the number of neighbours within the search (or coupling) radius h, W represents the cubic spline kernel (as defined in section 2.4.1), r_i is the position vector of i-th gas neighbour cell, and r_s the position vector of the referred star particle. Equation (3.26) is iteratively solved until the established value of N_{ngb} is found. Basically all gas cells that are located within a distance h (the coupling radius) from a given star particles are influenced by feedback originating from that star particle. To avoid numerical artefacts, h is limited to a maximum value of 0.86 kpc [18].

Finally, the weights $\tilde{w}_i$, appearing in equation (3.24) and that are needed to determine the correct amount of feedback energy and momentum injected into each gas cell i, are defined as

$$\tilde{w}_i \equiv \frac{w_i}{\sum_i w_i} \,. \tag{3.27}$$

In the previous equation w_i is computed as

$$w_i \equiv \frac{\Delta\Omega_i}{4\pi} = \frac{1}{2}\left[1 - \frac{1}{[\,1 + A_i\,/\,(\,\pi|\mathbf{r}_i - \mathbf{r}_s|^2\,)\,]^{\frac{1}{2}}}\right] \tag{3.28}$$

in which $\Delta\Omega_i/4\pi$ is essentially the fraction of solid angle at the position of the star particle $\mathbf{r}_s$ covered by the gas cell i, $A_i \equiv \pi\,\Delta x_i^2$ (with Δx_i the size of the cell i) is the area of the gas cell, $|\mathbf{r}_i - \mathbf{r}_s|$ represent the distance between the gas cell and the star particle. The energy and momentum feedback values are first computed relative to the star particle rest frame and then are converted to the values associated with the reference frame used in the simulation run upon injection into the gas.

We conclude by emphasizing that it is this implementation of the stellar feedback in the SMUGGLE model that makes it effective. As a consequence SMUGGLE is able to generate gas outflows on a galactic scale in a natural way. These outflows are thus strongly connected to the local phenomenon of star formation within the galaxy disk and the associated feedback processes mostly related to supernova events.

3.4 A glimpse of the simulated galaxy

The aspects discussed in the previous sections highlight the complexity of modelling a MW-type galaxy through a numerical approach that takes into account the most important phycical processes of galaxy evolution. In particular, during the evolution of the system, remarkable changes are expected to be seen within the galaxy and in its immediate surroundings in terms of: shaping of a multi-phase gas structure in the ISM, gas outflow phenomena caused by the various feedback channels (and chiefly by SN explosions), the possible gas re-accretion on to the disc plane through the establishment of a galactic fountain circulation between the star-forming disc and the halo just to name a few. To illustrate the complexity of these phenomena we now present edge-on and face-on projections of gas density, temperature and vertical velocity (with respect to the galactic plane) for the MW-like galaxy modelled in the simulation. We will see that it is

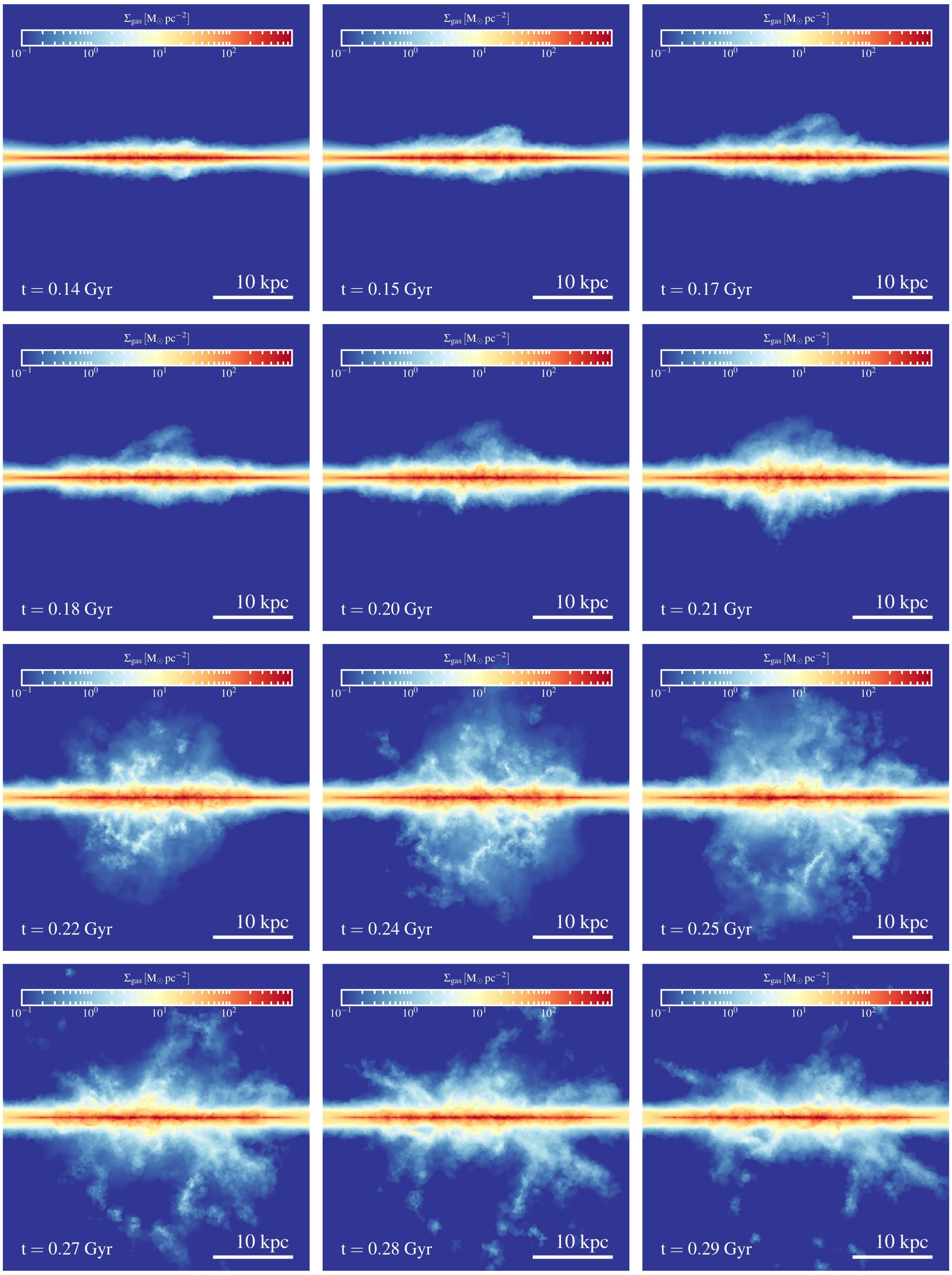

Figure 3.3: Projections of the gas column density Σ_{gas} (in units of $M_\odot$ pc^{-2}) for the simulated MW-like galaxy in a edge-on visualization. These projections, where the image size corresponds to 40×40 kpc, show an evolutionary time sequence of the galaxy that has been computed from a time of $t = 140$ Myrs to $t = 294$ Myrs. In particular, between one image and another (from left to right column) there is an interval of time of ~ 14 Myrs. By looking at the panels the presence of gas outflows/inflows on a galactic-scale as a result of the feedback is evident. In particular it can be easily seen that multiple SN explosions alter the distribution of gas in the disk, also producing a galactic fountain cycle and more articulated structures in the ISM.

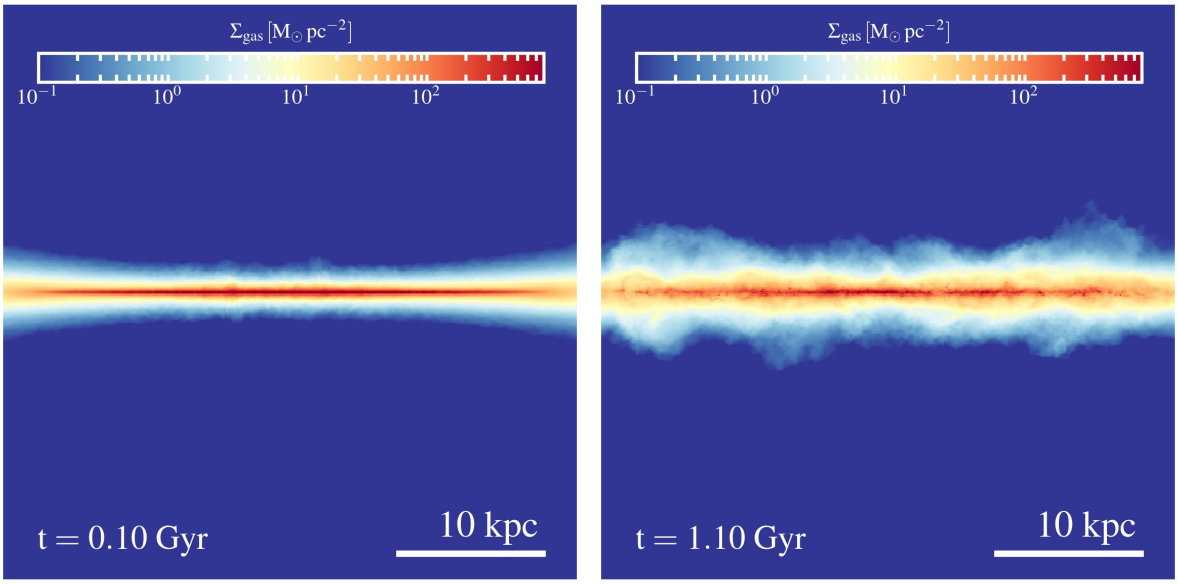

Figure 3.4: As in Fig. 3.3, but for two different time instants separated by $\simeq$ 1 Gyr. The two gas column density edge-on projections illustrate how the thickness of the disk increased along the axis perpendicular to the galactic plane as a consequence of the establishment of a galactic fountain cycle generated by stellar feedback.

possible to show in a qualitative way from these visualizations (focusing mainly on the images that better than others characterize the interaction between galaxy and its halo), the effects of the feedback generated by SNs on the ISM and the subsequent generation of gas outflow/inflow phenomena. The same phenomena will be discussed in a more quantitative way in Chapter 4.

In Fig. 3.3 we present a time evolution of edge-on density projections of the simulated galaxy are shown (see also Fig. 3.2 for a face-on visualization). From this figure it is particularly appreciable the growth of gas scale height in the vertical direction as a function of time, as a result of the ejection of gas due to stellar feedback. Because not all the gas ejected outside the disk plane is able to escape from the gravitational attraction field of the galaxy, some of the ejected gas rains back down on the disc starting igniting again star formation and the associated feedback causing further ejection of material in the galactic halo.

Looking at the first projection at the time t = 140 Myrs, one notices that the gas distribution is tendentially concentrated in the disk of the galaxy, whereas with the progress of time in the other projections an increasing modification of the gas structure above and below the disk plane is more and more evident, mainly caused by the fervent

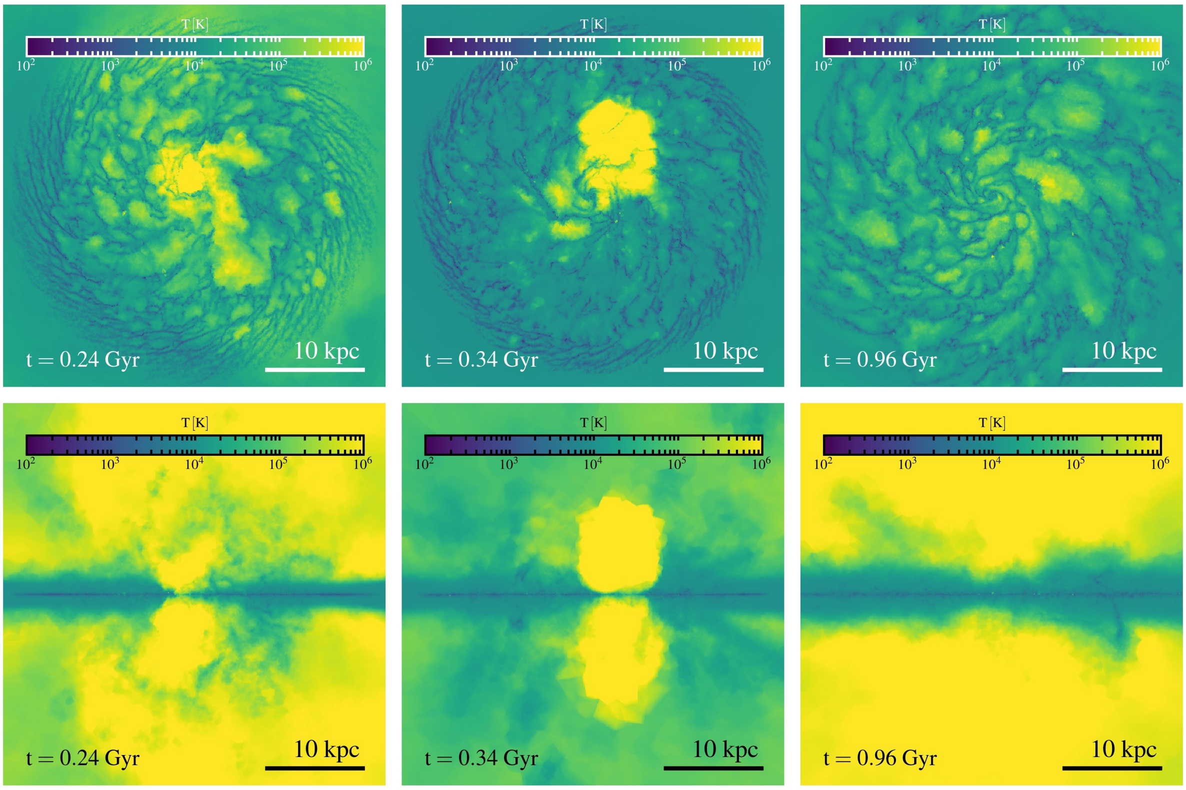

Figure 3.5: Projections of density-weighted gas temperature T (in units of K) for the simulated MW-like galaxy in a face-on (top row) and edge-on (down row) visualization. These projections, where the image size corresponds to 40×40 kpc, show an evolutionary time sequence of the galaxy that have been computed at time $t = 0.24, 0.34, 0.96$ Gyr. By looking at the panels of the first two columns (from the left to the right), it is clearly evident the effect generated by feedback on the ISM gas structure. This is characterized by high-temperature regions (highlighted in yellow) where the activity by SNs explosions produces hot cavities from which gas outflows are ejected from the galaxy. In the last column, the panels instead show a configuration of the galaxy where SN activity is less present, indicating that in ~ 1 Gyr most the star formation activity in the galaxy has reached a state of self-regulation. Also at this evolutionary stage a significant fraction of the gas has been consumed by the stellar formation and few violent events disturb the structure of the multiphase ISM.

activity of SNs. This feedback is the main channel that drives outflows of gas from the star-forming disk into the halo region and, as is evident in Fig. 3.3 and Fig. 3.4, these outflow phenomena are particularly intense near the galactic centre where the star formation activity is more intense.

A galactic fountain cycle is established between the galactic disk and the halo, in which the gas can flow away and, eventually, fall back into a new region of the disk. As time progresses, the gas distribution around the disk becomes increasingly thicker. In other words the disk thickness increases with respect to the one of the initial distribution (as shown in Fig. 3.4). The amount of material that is present in the halo region of the galaxy however depends on the level of star formation (and therefore of SN) activity at any given time in the simulation. This circulation of gas over time has also an important impact on the abundance of metals present in the ISM (see [68]) and more in general in redistributing the re-accreted gas within the star-forming disc to sustain new episodes of star formation.

In terms of the evolution of (density-weighted) gas temperature, it is possible to notice in the temperature plots (shown in Fig. 3.5) how the gas temperature is consistent with the density panels presented above. In particular in the face-on projections (top row), the lowest gas temperatures ($T < 10^3$ K, colors tending to blue) typically correspond to the densest gas regions ($\Sigma > 10\,\mathrm{M_\odot\,pc^{-2}}$, colors tending to red) that characterize the spiral pattern of the galaxy (see the face-on visualization in Fig. 3.2), and the hot cavities dug by stellar feedback correspond to the regions where the shocked-gas reaches high temperature ($T \sim 10^6$ K, colors tends to yellow). The temperature edge-on visualizations (bottom row) highlight the connection between high temperature and the ejection of high velocity gas (even at great distance from the disc plane) generated by SN explosions.

To better illustrate this point, in Fig. 3.6 we report face-on (top panels) and edge-on (bottom panels) kinematic maps of the gas (namely its velocity perpendicular to the disc plane v_z) considering a very short temporal sequence in which the presence of very high-velocities gas leaving the disk plane ($|v_z| \geq 150\,\mathrm{km\,s^{-1}}$), becomes (from the left to right) more and more accentuated as a consequence of a major episode of stellar feedback (i.e. the explosions of SNae). In particular, the face-on maps (top row) show that in the regions of the disc where very high vertical velocities are reached correspond to both

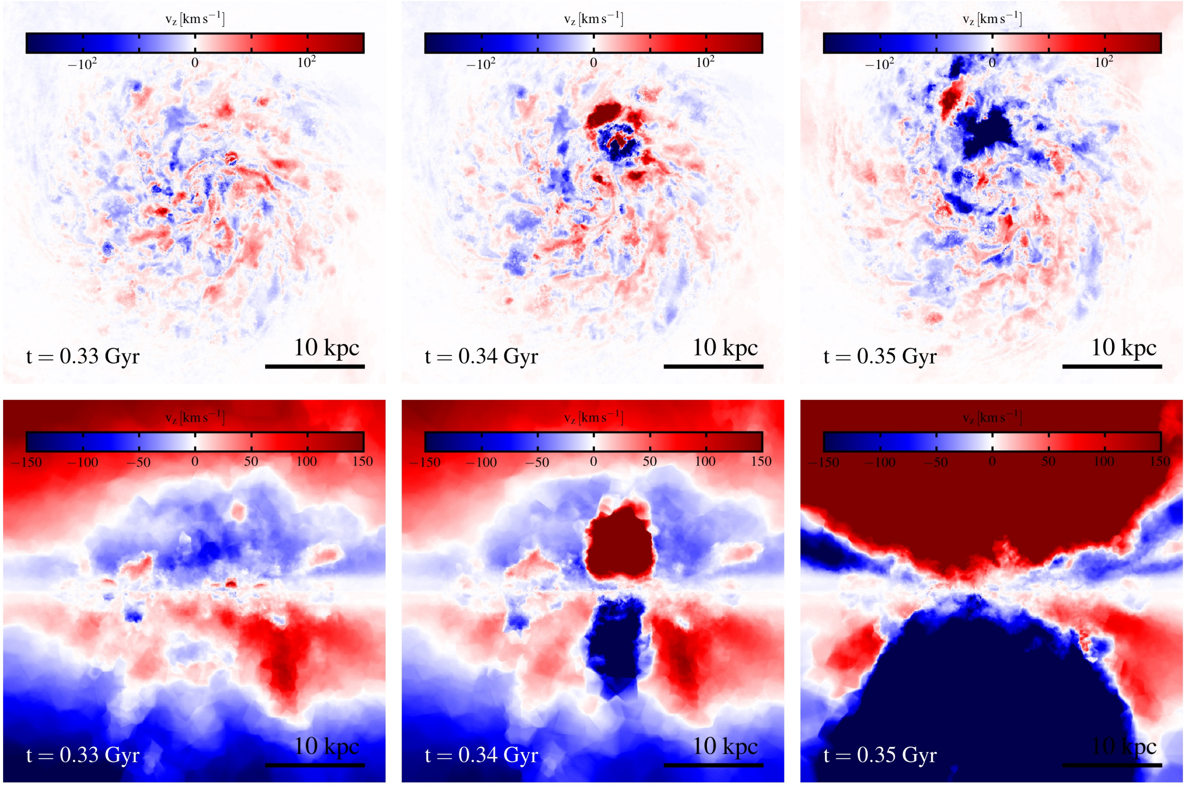

Figure 3.6: Projections of density-weighted gas velocity perpendicular to the galactic disc v_z (in units of km s^{-1}) for the simulated MW-like galaxy in a face-on (top row) and edge-on (down row) visualization. These projections, where the image size corresponds to 40×40 kpc, show an evolutionary time sequence of the galaxy that have been computed at time $t = 0.33$, 0.34, 0.35 Gyr. Note that the white color in the snapshots indicates that the gas is essentially at rest (or at very low velocities), whereas the gas at higher velocities is indicated with progressively redder (positive values of the velocities along the z axis) or bluer shades (negative values of the velocities along the z axis). Gas in red color is an outflow (inflow) if located above (below) the disc plane. Whereas for the gas in blue color the opposite occurs. These three consecutive time-steps of the simulation show the vertical velocities of gas on a very short time scale and near the galactic centre it is clearly visible the evolution of the gas expelled at highest velocities above and below the disc plane following a superbubble blowout.

SN-generated cavities (i.e. the lowest density regions) and high temperature regions. This is clearly visible if the maps of the galaxy taken at $t = 0.34$ Gyr in the edge-on panels of the Fig. 3.5 and Fig. 3.6 are compared.

Finally, we would like to note that the gas inflow is also visible in the kinematic maps discussed so far, in particular in the first column of the Fig. 3.6. Indeed, as the edge-on projection clearly shows that the gas located at a few kpc around the star-forming disc it assumes negative values of the vertical velocities above the plane of the disc (colors tending to blue) and positive values under the disc plane (colors tending to red). This means that before the superbubble formation at $t = 0.35$ Gyr not all the gas ejected by the previous SN feedback can escape away from the galaxy, but rather that a (substantial) fraction of it was re-accreted by the disc and recycled as a new fuel to support star formation. In the next chapter we will analyze in more detail the main properties of the gas circulation that we have introduced in this section.

Chapter 4

Results of the analysis

The main purpose of this work is to study the phenomena of gas outflows on a galactic scales caused by stellar feedback largely due to SN explosions in order to find a link between the properties of the gas cycle and the influence that it generates on the supply of fuel that can sustain star formation in an isolated galaxy for time longer than a few dynamical times.
In particular, we investigate the properties related to the gas cycle in star forming galaxies and how the hydrodynamic processes affect certain quantities such as the SFR, the rate of SN explosions and the energy-momentum eventually released into the interstellar medium by SNae.

After a brief discussion of the work that we carried out in preparation of the analysis of the simulation output (Sec. 4.1), we mainly focus on the kinematic and thermal properties of the gas outflow/inflow from/to the galaxy system, characterizing its vertical motion at various heights from the galactic plane and differentiating in temperature the various phases of the ejected gas (Sec. 4.2). We then examine various evolutionary trends related to the star formation phenomenon reconstructing the variation in radius within which a certain percentage of SFR occurs over time, the variation of the amount of mass of outflowing gas from the galaxy as a function of the star formation rate and star formation rate density, and by comparing the results obtained from the simulations and the trends obtained from the observations – as for instance in the analysis of the Kennicutt-Schmidt relation – (Sec. 4.3). Finally, we have also investigated the effects generated by SN explosions from the point of view of energy and momentum input released into the gas and in the production of gas outflows (Sec. 4.4).

4.1 Preparation for the analysis performed

Before starting the analysis of the results concerning the gas cycle in our simulated galaxy obtained in this work, we would like to briefly discuss what are the preparatory steps that we have taken in order to perform such analysis.

Let us start by pointing out that all the information related to the properties of the various components that constitute the galactic system are contained within the so-called snapshots. These files represent the output saved by the simulation. Each snapshot is basically a picture of the system at a given time and contains all the information needed for our analysis. Specifically, the simulation stores these snapshots – that are separated by approximately 7 Myrs in time – in computer as HDF5 (Hierarchical Data Format) binary data format, a file format designed to contain and organize substantial amounts of numerical data. The information needed for our analysis are stored in HDF5 because it is an open source, standardized format that makes it easy to support, retrieve and elaborate complex data. In particular, it makes convenient the use of the Python language for the analysis performed in this thesis because there exists handy libraries (such as H5PY [79], NUMPY [80], and MATPLOTLIB [81]) to easily manipulate that data format and produce the relevant plots. Indeed, all the results presented in this thesis have been processed with Python scripts that were specifically developed for this work.

The datasets on which we have focused our attention contain information about: the properties attached to the gas cells (including their star formation rates), the phase space variables of the existing initial star particles within the stellar disk and the bulge, and all the information related to the new star particles created during the evolution of the simulation. The latter dataset specifically contains information such as position, velocity, mass at the birth of the star, and the cumulative number of SNs (type II and type Ia) exploded from the beginning of the simulation to the snapshot being analysed. All these pieces of information are of crucial importance for the analysis of the properties of gas outflows and their connection to the star forming disk that has been carried out in this thesis.

Before moving on with the presentation of the results obtained in this work, we would like to discuss how we defined the reference frame used in the analysis. We recall that the simulation is performed over a cubical computational domain of side ~ 600 kpc and the main body of the galaxy is located at the center of such cube. For computational reasons,

linked to the generation of the Voronoi mesh, the origin of the axes is initially located in the one of the corners of the cube. However this choice of the coordinates is not very suitable to the type of the analysis on the properties of gas inflows and outflows that has to be performed in this work. Therefore, in order to better visualize the outgoing and incoming components in our galactic system we have chosen for simplicity to put the origin of the axes in the center of the galaxy.
This allows us to identify more easily the ISM, which is located in the galaxy mid-plane, and the distribution of the gas ejected by supernova events, which is located outside the galactic plane. In particular, we will assume that the plane of the disc lies in the xy-plane and the spin axis of the galaxy coincides with the z-axis. We then fix the origin of the axis taking the center of mass (CM) of the galaxy. We stress that this choice for the reference frame was applied to produce all the plots that will be discussed in the following sections.

In principle, the reference frame thus determined should be not evolving in time. In other words, we expect that the reference frame is static since the simulation model represent an isolated galaxy with no net (external) force acting on the system. This would imply that reference frame centered on the CM is an inertial frame and in particular the CM stays at rest because of the way initial conditions are built. In practice, this is not the case and the operation of determining the reference frame must be repeated for every snapshot. This is due to the adoption of the tree algorithm for the estimation of the gravitational force acting on each "particle" in the simulation, which breaks momentum conservation.

To understand why this is the case we note that the system is isolated, and therefore we expect that the gravitational interaction with each of these particles is (anti)symmetrical because of action-reaction principle. This anti-symmetry, in turn, implies momentum conservation. If we were to use a direct summation approach (that is compute the gravitational force acting on a particle as the sum of all gravitational forces due to all other particles) to compute the gravitational force of the system, the anti-symmetry would be preserved and momentum conservation would naturally follow. However, direct summation is a very inefficient method when it comes to practical numerical applications as it scales quadratically with the number of particle in the system. It is for this reason that in our simulations, a tree gravity algorithm (discussed in section 2.1.2) is adopted.

The algorithm represents a good way to speed up the calculation processes in terms of gravitational force estimation (calculations that are typically expensive from a computational point of view in the classic N-body codes, especially when the number of particles on the simulation increases [62]), because the scaling reduces to $N \log N$. However, there is a price to pay for this better scaling: a tree code does not conserve momentum to machine precision.

To compute the gravitational acceleration for a target particle the tree algorithm decides, according to a geometric or an acceleration-based criterion [22], whether to "walk" tree down to the individual particles (the so-called leaves of the tree) or to stop at tree nodes (i.e. larger regions of space containing a set of particles; see section 2.1.2). This operation allows to speed up gravity calculation because it is not necessary to compute the gravitational interaction between all particles pairs. Indeed, for particles which are farther away only the interaction between the target particle and a tree node must be evaluated. However, evaluating the gravitational force between a particle and a tree node breaks the (anti-)symmetry of the force calculation. As a direct consequence of this fact, the momentum is not conserved to machine precision and the CM (which was initially stationary) will have a net force acting on it. It is for this reason that we are forced to redefine the origin of our reference frame for each snapshot of the simulation.

Nevertheless, it should be stressed that the error induced on the momentum conservation by the tree gravity calculation is in any case negligible. In fact, the errors in momentum conservation are small and they add only a tiny amount at each time step. Furthermore, in the tree algorithm implementation of AREPO, these errors are uncorrelated and for a sufficiently high number of time steps they then tend to cancel out. Therefore, even tough momentum is not conserved at machine precision, the CM will not vary much its initial position and velocity. In the analysis that follows, we nevertheless took care of these small motions of the center of mass[1] in each simulation snapshot by centering all particles positions and velocities relative to the position and the velocity of the CM at that specific instant in time.

---

[1] The typical (random) velocity of the center of mass is $\sim 0.1\,\mathrm{km\,s^{-1}}$, to be compared with gas velocities of the order of $\sim 100\,\mathrm{km\,s^{-1}}$.

4.2 Galactic-scale vertical gas motions

The first approach of interest was aimed at understanding some kinematic properties of the gas, which, as a result of stellar feedback (in particular SN explosions), can locally vary its structure and be ejected from the main body of the galaxy. This represents an important aspect of this thesis work, as we are interested in understanding the physical processes generating gas outflows/inflows on a galactic scale and in characterizing the key properties of such flows of gas.

We begin by studying the total gas mass distribution with respect to the gas velocity along z, above and below the galactic plane, for different ranges of the z coordinate. In particular, coordinates are centered in such a way that for $z = 0$ the gas is in the middle point of the galactic plane, while both the disk and the bulge of the galaxy are in the region with $|z| \leq 2$ kpc. This was done precisely because in this way it is possible to discern which components of the gas in motion along the z-axis are oriented in the incoming/outgoing direction both above and below the galactic plane (as we will see in Fig. 4.1). The value $|z| \leq 2$ kpc is arbitrarily chosen, but we note that this region is large enough to contain the bulk of gas in the star forming disk of the galaxy, while at the same time it is close enough to the disk that allows us to study the flows of gas from and towards the galactic plane in the vicinity of the galaxy itself.

We expect that the gas in proximity of disk region ($|z| < 2$ kpc) has a different kinematics in the vertical direction than the gas that is outside the disk region ($|z| > 2$ kpc). Specifically, as we will see in Fig. 4.3, the cold gas remains mostly concentrated around the disc, while hot gas at higher speeds $|v_z| > 300\,\mathrm{km\,s^{-1}}$) is the component that can be found at larger distances ($|z| \gg 2$ kpc) from the galactic plane.

In order to better understand the kinematics of the gas in its vertical motion and its mass distribution at different heights from the disc, we generate an histogram of the Probability Density Function (PDF from now on) of the gas mass with respect to the gas velocity v_z along the z-axis. The expected graph is a sort of bell-shaped curve in which the most probable velocity v_z of gas particles is around zero. Namely most of the gas is close to the galactic plane (x, y plane in the frame of reference chosen for our analysis).

We point out that histograms are a useful way to show trends and results of continuous numerical data set[2].

---

[2] Histograms are constructed starting from the subdivision of the range of values that assumes a

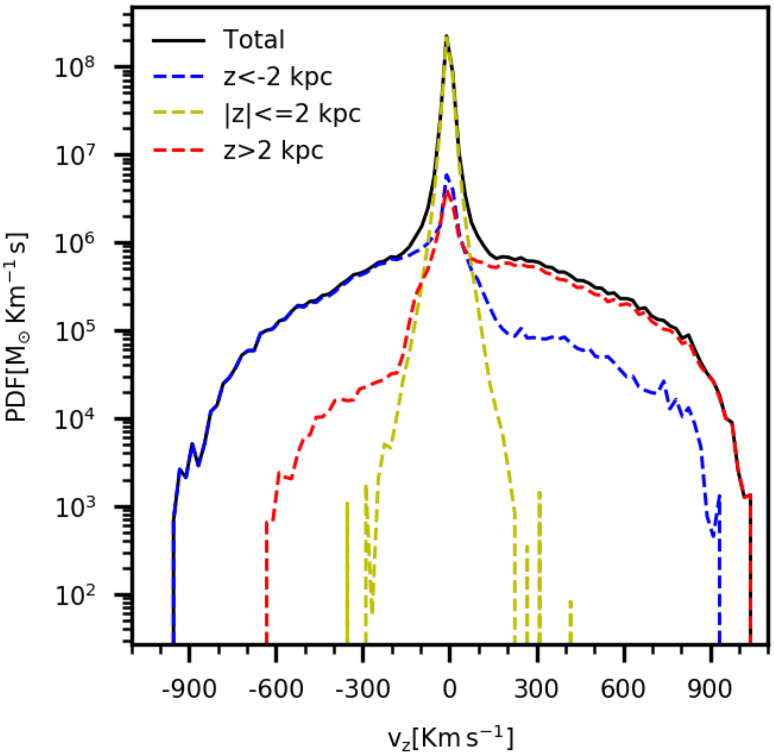

Figure 4.1: Histogram of gas mass-weighted PDF as a function of gas velocity perpendicular to the disc plane v_z. The area under the black curve represent the total gas mass distribution, whereas the other curves select different gas regions near ($|z| \leq 2$ kpc; yellow), above ($z > 2$ kpc; red) and below ($z < -2$ kpc; blue) the galactic plane. The histogram is taken at simulation time $t = 0.7$ Gyr. All curves have a peak at $v_z = 0$ and most of the gas mass stays near the galactic plane. At this specific time, there are evident episodes of gas inflow and outflow as shown by red and blue lines.

We report in Fig. 4.1 the histogram relative to snapshot number 100 that corresponds to a time of about 0.7 Gyr from the beginning of the simulation. By looking at the black curve, which represents all the simulated gas, we notice that the total distribution is approximately symmetric and, as mentioned before, that the most probable velocity along z is zero. To study the gas that is inflowing towards the galaxy or outflowing from it, we must first select whether it is located above ($z > 0$) or below ($z < 0$) the galactic plane. Indeed, gas with $z > 0$ is outflowing from the galaxy if it has a *positive* vertical velocity whereas gas that is inflowing has *negative* v_z. The opposite is true for gas located below ($z < 0$) the galactic plane.

The red line shows us that above the disk the bulk of gas is still close to the xy plane (namely $v_z \sim 0$), but a notable component is flowing out from the galaxy (namely it is above the disk with positive velocity v_z). There is also a smaller component of gas that flows onto the disk which is represented by the red branch on the left with $v_z < 0$. An analogous behaviour of gas outflow and inflow is present below the disk as shown by the blue curve. The amount of outflow below and above the disk is about the same. The yellow curve displays the distribution of gas which we have characterized as belonging to the galaxy – here inflow and outflow are considerably less prevalent, that is the width of the distribution is narrower – and most of the gas remains close to the disk.

All three peaks are centered at the zero point of the v_z and so we deduce that most of the gas, even if it is expelled from the galaxy, has not enough speed to leave its gravitational potential well. This indicates that the gas is ejected from the disk and subsequently re-enter into it, starting a galactic-scale circulation. However, part of the gas can also assume large speed values and it is never re-accreted.

Returning to the distribution curves, it is evident that the gas close to the galactic plane with speed $|v_z| < 100\,\mathrm{km\,s^{-1}}$ represents the dominant component in terms of mass abundance. This is because in that velocity region the yellow curve (which represents the amount of gas close to the disc) coincides with the black curve, which represents the total amount of gas and peaks at $v_z = 0$. It is also important to note that the yellow curve is

---

continuous variable in a series of intervals (or bins), and then counting the number of values in the data set that fall in each bin. In particular, it is the area under the curve contained in an interval of the variable that indicates the frequency of occurrences for each bin. How wide a bin should be in size depends on the actual data distribution and the goals of the analysis to be carried out. In particular, one need to make sure that the bins are not too small or too large.

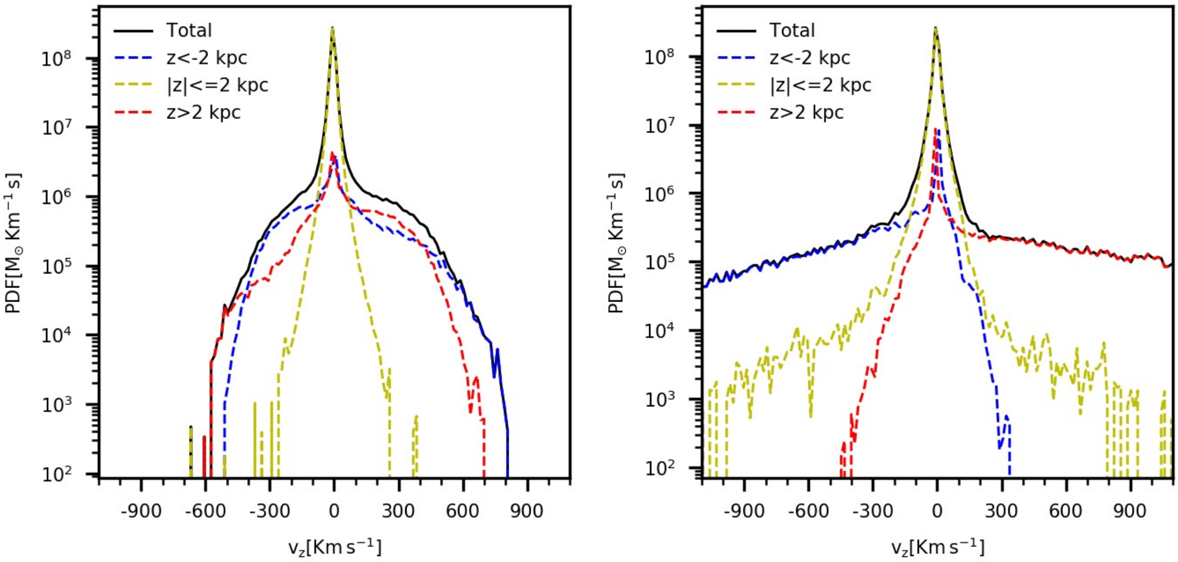

Figure 4.2: Histograms of gas mass-weighted PDF as a function of v_z, the gas velocity perpendicular to the disc plane. The area under the black curve represent the total gas mass distribution, whereas the other curves select different gas regions near ($|z| \leq 2$ kpc; yellow), above ($z > 2$ kpc; red) and below ($z < -2$ kpc; blue) the galactic plane. The histogram on the left panel is taken at simulation time $t = 0.91$ Gyr, whereas on the right panel $t = 0.35$ Gyr from the beginning of the simulation. All curves have a peak at $v_z = 0\,\mathrm{km\,s^{-1}}$ and most of the gas mass stays near the galactic plane in both panels. If we compare these histograms with the one presented in Fig. 4.1, we can easily deduce that: in the left panel gas inflow and gas outflow phenomena are less evident as shown by the narrower width in velocity of the gas distribution above and below the disc plane (red and blue lines, respectively), whereas in the right panel the range in velocity is noticeably wider, specifically indicating a clear phenomenon of gas outflow at very high velocity ($|v_z|$ in excess of $500\,\mathrm{km\,s^{-1}}$).

symmetrical with respect to the zero point of the speed, whereas the red and blue curves are asymmetrical. This is indicative that, in this specific snapshot, a net outflow of gas is present both above the disc plane (as shown by the red curve for positive velocity) and below the plane (as shown by the blue curve for negative velocity). Indeed, the snapshot used to produce this graph was explicitly chosen to emphasize the outflow of gas from the galaxy system, but we point out that this scenario may change during the temporal evolution of the system, that is by choosing another snapshot where the star formation activity and the associated feedback can be lower or higher.

We analyze this aspect in Fig. 4.2. The key difference between the scenarios, shown in Fig. 4.1 and in Fig. 4.2 at different time-step of the simulation, consists in the width of the velocity range that the gas can reach. The velocity width is indicative of the strength of the outflow and inflow phenomena: both phenomena are stronger if the amount of gas is distributed over a wide range of $|v_z|$. In particular, the right panel of Fig. 4.2 shows that gas outflow is less intense with respect to the snapshot depicted in the left panel because the velocities reached by the ejected gas clearly exceed a speed of $|v_z| > 500\,\mathrm{km\,s^{-1}}$ from galaxy. Therefore a mass of gas of $\sim 2 \times 10^5\,\mathrm{M_\odot}$ is lost from the galaxy with no possibility of re-entry into the system. This effect is directly related to the stellar feedback. In particular, at that time that an intense stellar formation event has occurred in the system and that caused a rise in the rate of SNII explosions. This eventually lead to a very pronounced gas ejection episode.

By choosing a cut in temperature it is possible to separate the contribution to the total gas mass of the different gas phases (cold $T \leq 10^4\,\mathrm{K}$, warm $10^4\,\mathrm{K} < T < 10^6\,\mathrm{K}$, and hot $T \geq 10^6\,\mathrm{K}$). Moreover, with a suitable cut in v_z, it is possible to single out the components of gas inflow and outflow, as shown in Fig. 4.3. On the left panel, gas outflow is coming out above the galaxy if v_z is positive and takes negative values if gas is coming out below the disk mid-plane. On the other hand, on the right panel, the negative values of v_z represents the components of gas inflow entering above the galactic plane, whereas positive values represents gas inflow entering below the mid-plane.

As the left panel of Fig. 4.3 shows, there is an episode of gas outflow from the simulated galaxy at this specific simulation time[3], which corresponds to about 0.7 Gyr.

---

[3] This simulation time was arbitrarily chosen as a representative snapshot of the phenomenon of interest, but outflows are present in many others snapshots, see for instance Fig. 3.3.

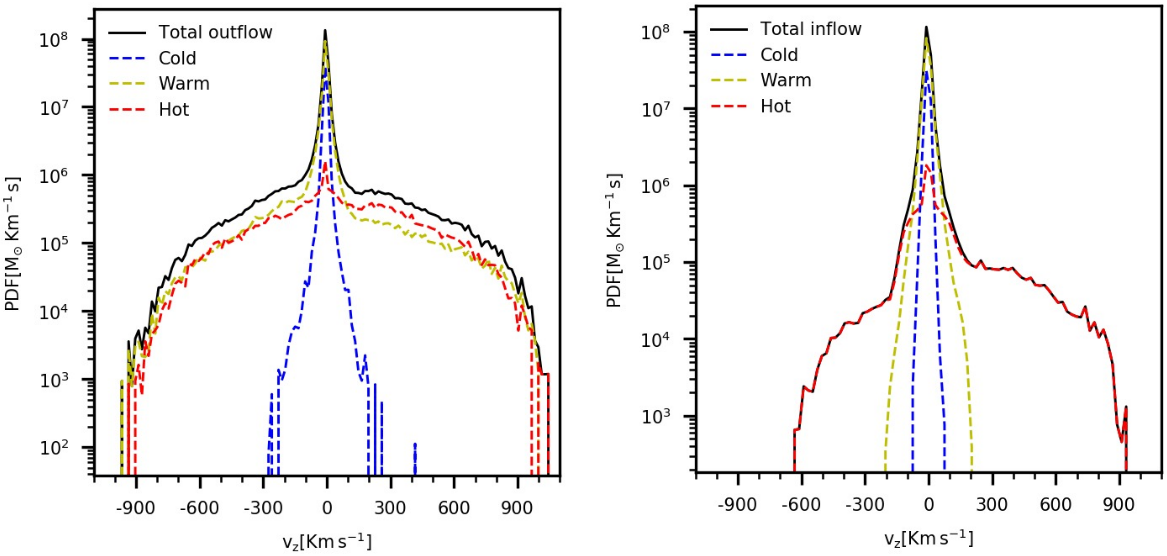

Figure 4.3: Histograms of gas mass-weighted PDF compared to the gas velocity perpendicular to the disc plane. Outflow/Inflow gas phases at cold (blue), warm (yellow) and hot (red) phases (see the figure discussion for the definition of these three gas phases) are evident in the right and left panels, respectively. On the left panel, we have selected the velocities of gas along the z-axis with the outgoing direction both above and below the galactic plane, thus highlighting only the outflowing gas. Instead, on the right panel, we have selected the velocities v_z which entering both above and below the galactic plane, thus highlighting a inflowing gas mainly occurring below the mid-plane of the galactic disc as shown by the trend of the curves for positive value of v_z.

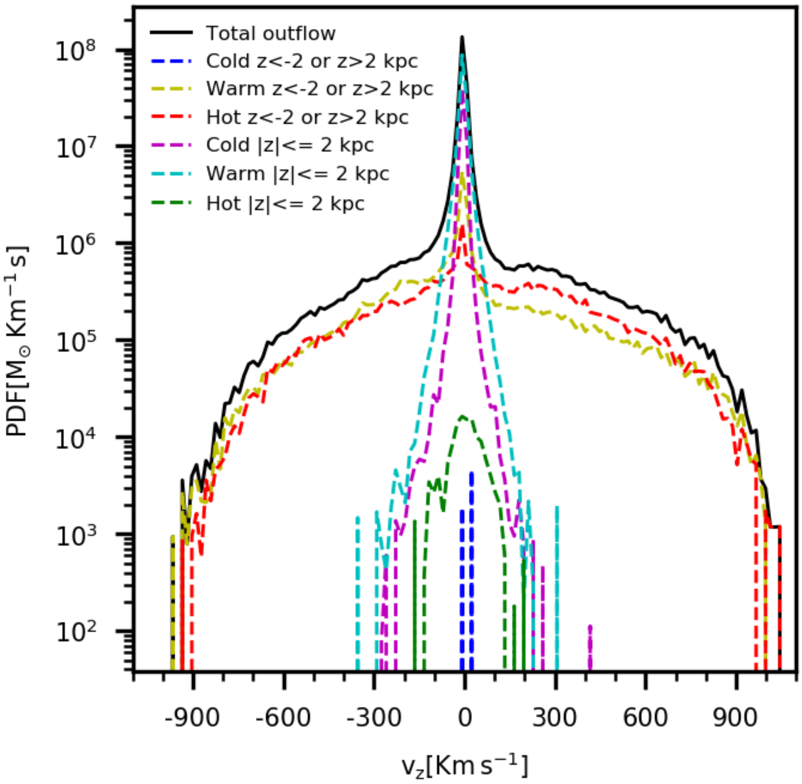

Figure 4.4: Histogram of gas mass-weighted PDF as a function of v_z, the gas velocity perpendicular to the disc plane, for outflowing gas. Gas phases close to the galaxy, in a range of $-2 \leq z \leq 2$ kpc, are represented by violet (cold gas), turquoise (warm gas) and green (hot gas) lines, whereas gas phases outside the galaxy for $z < -2$ kpc and $z > 2$ kpc are displayed by blue (cold gas), yellow (warm gas) and red (hot gas) lines, respectively. The curves of the distributions show that most of the gas mass stays near the galaxy disc at low velocity along the coordinate z, primarily in the cold and warm phases. High velocity components of warm (yellow) and hot (red) gas are outflowing from the galaxy. We would like to note that the mass of outflowing is a few orders of magnitude smaller than the gas mass near the galactic disc.

However, the outflow is not very abundant in terms of mass with respect to the total gas mass at low speeds ($|v_z| < 50\,\mathrm{km\,s^{-1}}$) in the vicinity of the galaxy. In particular, being the graph in a logarithmic scale and as a function of the gas mass, the height peaks at zero imply that most of the gas abundance remains concentrated in the vicinity of the disc ($-2 \leq z \leq 2$ kpc) and at relatively low speed ($|v_z| < 50\,\mathrm{km\,s^{-1}}$). On the other hand, the "wings" of the distribution imply that the gas can assume sufficiently high vertical velocity values to be ejected from the disc plane and, if the speed is high enough, to escape from the gravitational attraction of the galaxy. The expelled gas is not very abundant in terms of mass. Indeed its total mass turns out to be about $8 \times 10^5\,\mathrm{M_\odot}$ for the warm gas (yellow curve), $6 \times 10^5\,\mathrm{M_\odot}$ for the hot gas (red curve), and $5 \times 10^4\,\mathrm{M_\odot}$ for the cold gas (blu curve) in a velocity range of $|v_z| > 100\,\mathrm{km\,s^{-1}}$. The cold gas represented by the blue curve has a much tighter distribution around $v_z = 0$ than the other curves. This implies that for supernova feedback is difficult to accelerate cold gas to large velocities (the bulk of the cold gas phase is found in the velocity range $|v_z| < 100\,\mathrm{km\,s^{-1}}$). As a consequence the cold gas that is ejected from the mid-plane remains relatively close to the disc as a part of a galactic fountain flow. Finally, all the peaks of the different curves are centered at the zero point of the speed v_z and only a part of hot (red curve) and warm (yellow curve) gas are ejected from the disc with speed close to or greater than the current estimate of Milky Way local escape speed at $\sim$ 8 kpc from the Galactic Center ($|v_z| > 500 - 600\,\mathrm{km\,s^{-1}}$, see [78]).

The right panel of Fig. 4.3 shows the trend of gas inflowing towards the galaxy in terms of mass abundance for the different phases. Compared to the right panel of the same figure, there is an asymmetry in the trend of the red curve (hot gas) that indicates, in this specific snapshot, an inflow of gas mass under the plane (positive values of v_z) that is greater than the incoming gas above the plane (negative values of v_z).This returns the information that more gas is recycled above the galactic plane, revealing an asymmetry between the galactic fountain cycle above and below the galaxy mid-plane. At low speeds ($|v_z| < 100\,\mathrm{km\,s^{-1}}$) the mass of the different gas phases are comparable, especially for cold (blue curve) and warm (yellow curve) gas. Indeed, these distributions in terms of velocity v_z are narrow distributions peaked at $v_z = 0$ indicating that most of the incoming gas is already concentrated in the vicinity of the galactic disk. The distribution of the velocity of the incoming hot gas (red curve) has much wider wings than the other curves.

This indicates that some of the inflowing gas may reach very high velocities. However, it must be recalled that this inflowing hot phase at high velocity only represent a minor fraction of the total gas mass. Finally, by comparing the left panel in Fig. 4.3 with the panel in Fig. 4.4, it can be appreciated that most of the gas mass is located in the region of the disc between $-2 \leq z \leq 2$ kpc having v_z component close to zero point of the velocity, as highlighted by the peaks of the different curves. The Fig. 4.4 in fact represents the same histogram of the left panel in Fig. 4.3 in which, however, we have made a cut in height for the different gas phases located in a region close to ($-2 \leq z \leq 2$ kpc) and far ($|z| > 2$ kpc) from the disc, and having a velocity in a direction consistent with an outflow from the galactic plane.

Particularly noteworthy in Fig. 4.4 is that the bulk of mass of the cold (violet curve) and warm (turquoise curve) gas lie in the region close to the galactic disc and has a narrow velocity range ($|v_z| < 80\,\mathrm{km\,s^{-1}}$). This implies that most of the cool gas is not ejected from the galaxy as a result of the outflow phenomena in this specific snapshot (~ 0.7 Gyr), as can be inferred from the blue curve representing the amount of cold gas outside the disc region ($|z| > 2$ kpc). Moreover, from the red and green curves representing the hot gas media, it can be seen that most of this phase is found at high speeds outside the disc region (red curve), whereas only a small amount of hot gas is detected near the disc plane in a limited speed range (green curve). The warm gas outside the disc region (yellow curve) also follows a behaviour to very similar to that of the hot gas (red curve).

All these pieces of evidence shown by the trends of the various curves suggest that SN feedback accelerates the different gas phases in a different way. In particular, with regard to this specific snapshot representative of the system, we can conclude that most of the gas impacted by the SN stellar feedback is typically found in a warmer phase (yellow and red curves) and it is in fact found in greater abundance outside the disc region (although we point out that a more substantial component of warm gas phase is present inside the disc, as shown by the peak of the turquoise curve).

On the contrary, we can note that typically most of the cold gas remains confined in the disc region (purple curve) and that the cold gas outflow component outside the disk region (blu curve) ejected by the SN feedback is manifestly smaller in terms of mass abundance and it has a very low ($v_z < 50$ $\mathrm{km\,s^{-1}}$) vertical speed.

As we will see in the next sections, in order to better investigate the properties of galactic-scale gas outflow phenomena and to generally deepen the vertical kinematics of gas media near the galactic disk, we will focus our analysis on the connection between the star formation occurring in the disk, SNs explosions, and the injection of energy and momentum imparted to the gas by stellar feedback.

4.3 Per Aspera ad Astra: star formation evolution and its connection to gas ejection

In this section we will discuss the possible information that can be extracted from the study concerning the star formation that takes place during the whole temporal evolution of the system. For instance, we expect possible changes in time from the point of view of the radius within which a certain percentage of SF occurs in the disc, the Star Formation History (SFH) of the simulated MW-like galaxy and the SFR surface Density (SFRD) as a consequence of amount the fuel available (basically cold and dense gas) in the system in order to generate new stars and the associated stellar feedback (SN explosions). The latter is then the main driver of the gas circulation between the galaxy and its halo and directly impacts the evolutionary trends of the various graphs related to star formation that we will discuss in this section. We are strongly interested in these aspects because we expect a connection between the mechanisms generating galactic-scale outflows and the availability of gas in the star-forming disk. Such gas is needed to sustain the galaxy star formation activity, which is ultimately behind the feedback processes driving the outflows.

There are many observational indications that the MW has formed stars with an almost roughly constant rate over the last 10 billion years [82] [83]. In our model, we describe an idealized MW-like galaxy without an external gas supply, whereby the only available fuel for the galaxy to make stars is through the gas within the disk (under certain conditions of density and temperature). In this way, the galaxy will consume the most of its gas in a few dynamical times around its z-axis ($\sim$ a few Gyrs), since there is no other fresh gas to sustain star formation for a longer period of time.

To analyze our expectations about the effects of outflow and inflow gas on the creation of stars inside the various regions of the galactic disk during its temporal evolution (conversely, we are also testing the effects of star formation on the generation of gas

outflows), we decided to display the radius variation within which a given percentage of the SFR occurs into the galaxy during the entire simulation time. We chose to define the radius within which 70% of the star formation is contained (namely $R_{(70\%)SFR}$) and we calculate it for all snapshots of the run simulation, as shown in Fig. 4.5.
In order to compute this, we decided to analyze the evolutionary trend of the $R_{(70\%)SFR}$ radius SFR-weighted as a function of time t covering all the temporal evolution, snapshot by snapshot, of the simulation.

The plot in Fig. 4.5 is constructed with equal size bins, which are consecutive and non-overlapping intervals of the t variable. This kind of study gives us back as first information that during the temporal evolution of the galaxy, 70% of the stellar formation takes place mostly within a radius of $4.5 - 5$ kpc from the galactic center. For the realization of the Fig. 4.5 we first recovered the distance of all the gas cells within a certain radius limit set at 40 kpc from the galactic center using the planar coordinates associated with the gas components of the system. In other words, we have basically estimated this radius as $R = \sqrt{x^2 + y^2}$.
Subsequently, we selected only actively star-forming gas cells and we considered only those located within a radius containing 70% of the global star formation rate at each snapshot. In particular, we have considered all the SFR occurred within a 40 kpc radius cut from the center, so to be sure to consider all the stellar formation occurred in the galactic system during the simulation run. Following the evolution of the curve from the beginning of the simulation to the first 100 Myrs, it is possible to notice that the radius $R_{(70\%)SFR}$ initially follows an increasing trend and this is strictly related to the initial conditions of the simulated galaxy, in which the gas cools inside-out in the disc, thus creating stellar particles at increasingly greater distances from the galactic center.
As time progresses, the decreasing trends of the curve indicate that the stellar formation activity is potentially disturbed by the multiple events of SN explosions, whose feedback generates gas outflows leading to a gas escape from the star forming disc. Instead, an increasing trend of the curve may indicate that during a given time period the galaxy is increasing its gas supply for star formation (as a result of the possible phenomena of inflow, i.e. gas recycling) and that the activity of SNe is reduced or less efficient in injecting energy and momentum into the ISM.
For instance, by comparing the Fig. 4.5 with the edge-one projections of the gas column

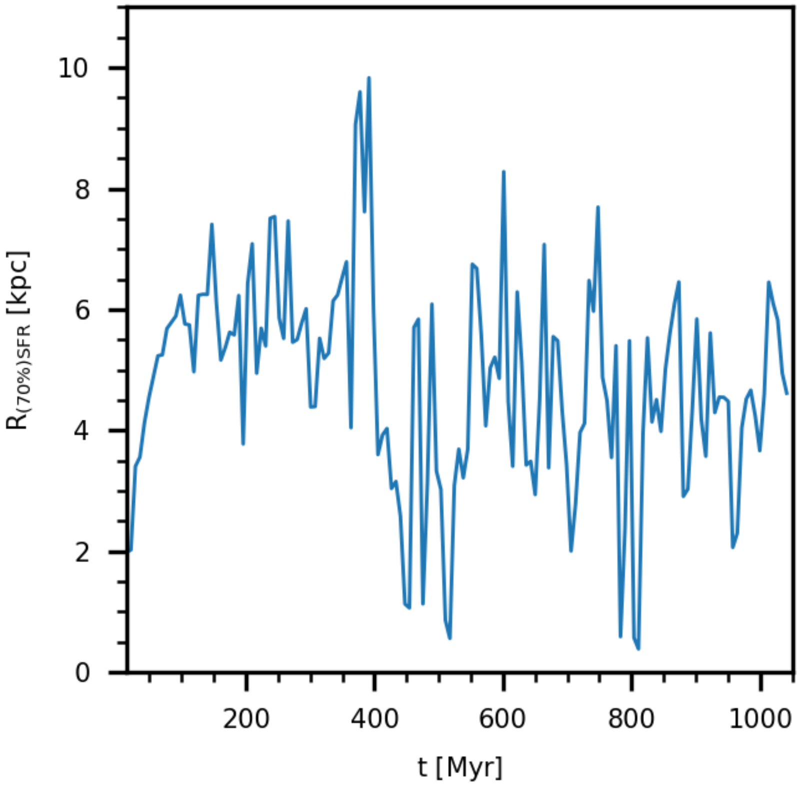

Figure 4.5: Evolution of the $R_{(70\%)SFR}$ radius as a function of the simulation time t. The trend of the curve indicates that the radius within which 70% of the star formation occurs remains almost constant with a value of about $4.5 - 5$ kpc. However, substantial variations of $R_{(70\%)SFR}$ are evident as a result of the dynamic evolution of the galaxy and the stellar feedback. In particular, we would like to note, for instance, how the curve changes radically in a temporal range between $350 \leq t \leq 450$ Myrs switching from a sharp peak (in which $R_{(70\%)SFR} \simeq 10$ kpc) to a depression with a radius $R_{(70\%)SFR} \simeq 1$ kpc. The growth of the curve before the peak indicates that the 70% of the stellar formation happened along most of the extent of the galaxy in an apparently undisturbed way. Whereas subsequently the steep decrease of the curve indicates that an intense phenomenon of gas outflow has occurred following the explosion of multiple SNs. More time has to pass before the gas in the disc reaches the right conditions of density and temperature (or is accreted by the galaxy as a result of the inflow gas phenomena) to still form stars at larger radii from the galactic center.

density in Fig. 3.3, it is possible to observe in the time interval $0.14 < t < 0.29$ Gyr (time covered by the panels of Fig. 3.3) as the curve trend present two consecutive decreases just in correspondence of the outflow phenomena visible in the edge-on panels of the galaxy. The same reasoning can be applied for the other decreasing trends of the curve and in particular to the steep slopes present in the center of the graph in a time range between $390 \leq t \leq 560$ Myrs, where powerful outflow phenomena have occurred as a result of SN feedback. This temporarily stops part of the stellar formation phenomenon in some regions of the galaxy and drastically reduces the value of $R_{(70\%)SFR}$.

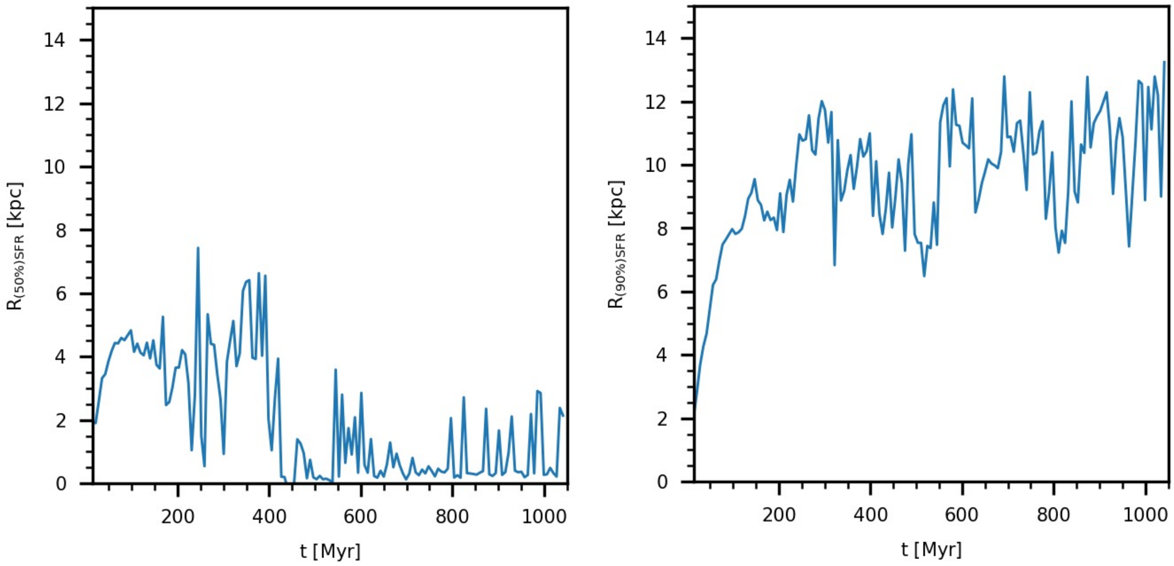

Figure 4.6: Evolution of the $R_{(50\%)SFR}$ and $R_{(90\%)SFR}$ radii SFR-weighted as a function of the simulation time t. The left panel shows the variation of the radius in which is contained 50% of the stellar formation during all the time range of the simulation, while the right panel shows the variation of the radius within which is contained 90% of the stellar formation. From the comparison of the two plots, it is evident that the two curves follow a similar trend in the earliest snapshots of the simulation, but very rapidly the two trends differ and globally the profile on the left side will follow a decreasing trend, whereas the one on the right side will follow an increasing trend with the progress of the simulated time. From the comparison of the two trends it is interesting to note the the disk is star-forming even at great distances (~ 14 kpc) from the galactic center. However, it is evident from the left panel that after about $400 - 500$ Myrs most of the cold gas ends up in the innermost regions of the galaxy, where actually 50% of the entire star formation occurs.

It is clearly possible to make different choices of the radius within which a certain amount of SFR is contained in the galaxy during the time evolution of the simulation. Similar to what we discuss in Fig. 4.5, we report in Fig. 4.6 two evolutionary trends in terms of $R_{(50\%)SFR}$ (left panel) and $R_{(90\%)SFR}$ (right panel). Starting from the left panel, we can deduce that, during the temporal evolution of the system, 50% of the stellar formation happens in regions more and more close to the center of the galaxy, and in fact, the trend of the curve tends to decrease with the progress of time until settling to an average constant trend in the last $200 - 300$ Myrs of the simulation with an average radius of ~ 1 kpc. This last statement could indicate the fact that the galaxy after a previous tumultuous evolutionary period (following the continuous cooling cycle of the star-forming gas, frequent explosions of SN, generations of outflows that sweep away the gas and the subsequent recycling of a part of it following the inflow gas phenomenon) settles on a more regular trend from the point of view of the star formation rate and the rate of SN explosions.

Specifically, from current estimates of these values for galaxies like MW, we expect the star formation rate to settle at $1 - 2\,\mathrm{M}_{\odot}\,\mathrm{yr}^{-1}$ and the rate of SN explosions to be about $1-2$ SN per century (see [85] and [86]). Nowadays it is known that the only gas contained within MW-like galaxies that form stars, without considering the external contribution of additional fuel sources supporting SF, tends to exhaust in about a few Gyr at a typical SFR of $\sim 1\,\mathrm{M}_{\odot}\,\mathrm{yr}^{-1}$ (see [37]). So we expect a similar behavior for our simulated galaxy as we will discuss in Fig. 4.7, but in general we know that galaxies like the Milky Way have sustained a star formation rate about constant for almost the lifetime of their existence, so there must be other channels that the galaxy can use to get fresh gas useful to sustain SF for a longer time.

Returning to Fig. 4.6, from the increasing trend of the curve of the right panel we can deduce instead that, as the time of the simulation progresses, the galaxy creates stars in a $R_{(90\%)SFR}$ radius that tends to be greater, involving in this process the galactic disk in all its extent. Similar to what we discussed in Fig. 4.5, also in this case we can attest that the decreasing trends of the curve indicate that the stellar feedback channels have played an important role in the expulsion or heating of the gas in the disc, thus leading to a concentration of most of the star formation activity in a region close to the galactic center.

We point out to the reader that the figures discussed so far in this section do not give

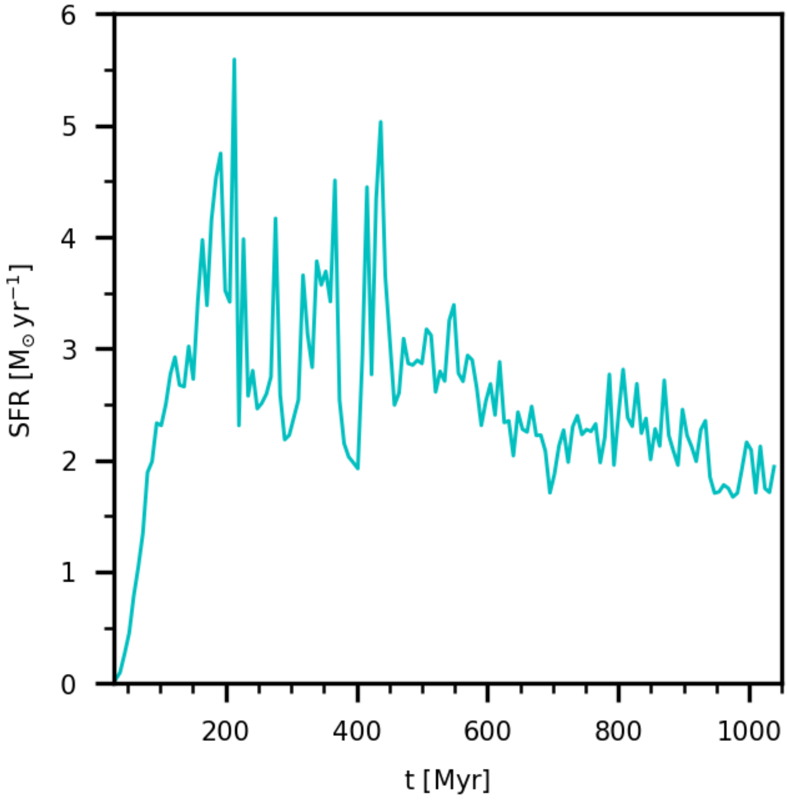

Figure 4.7: Evolution of the SFR as a function of the simulation time t. The amount of SFR is strictly related to the availability of gas in the galaxy that can be converted into stars. The latter is regulated by the phenomena of inflow/outflow gas on a galactic scale. In particular, the deep depressions present in the profile around $200 \leq t \leq 500$ Myrs indicate that a powerful outflow phenomena have swept away gas potentially useful to create stars, rapidly reducing the SFR by a factor of 2 or more.

any indication about the number of stars created for each snapshot considered and that therefore the increase/decrease of the R_{SFR} radius does not necessarily correspond to an increase or decrease of the number of stars formed in a certain time range. For instance, if we compare two distinct values of $R_{(70\%)SFR}$ in two different snapshots of the simulation, it is possible that to a small value of $R_{(70\%)SFR}$ corresponds a total SFR very intense near the center and outside that radius have a much lower SF (because possibly the average densities of the cold gas are not high enough to generate stars). Obviously the opposite of this scenario is true.

However, we would expect that these profiles may change according to the presence of powerful gas outflow phenomena, or following the SFR, or as a function of the so-called star formation rate density (i.e. Σ_{SFR}, which we will define later in the discussion). With regard to this we have decided to deepen the analysis in this direction trying to evaluate further trends between gas outflows and star formation.

To analyze the evolution of the star formation rate of the simulated galaxy, we present in Fig. 4.7 a plot of the SFR in units of $\mathrm{M}_\odot\,\mathrm{yr}^{-1}$ as a function on the t time covered by all 150 snapshots of the simulation. As expected the galaxy initially creates stars at an ever increasing rate. This is mainly due to the initial conditions discussed in the chapter 3 in which the gas initially placed at a temperature of 10^4 K rapidly cools down and "collapses" into the disk, eventually converting part of its amount into stars as time progresses. The substantial spikes in the curve around at 200 Myrs show this trend. The decreasing trend of the curve (especially when the slope is manifestly steep) indicates instead that the SF in the galaxy drops as a consequence of the generation of gas outflows resulting from the effects of SN feedback. Remarkable variations of this trend are appreciable in the region of the graph between $200 \leq t \leq 500$ Myrs. After this period the galaxy tends to settle down, the amount of cold and dense gas available for star formation becomes increasingly less and the profile fluctuates around $\sim 2\mathrm{M}_\odot\,\mathrm{yr}^{-1}$, similar to what is estimated today for star-forming MW-like galaxies (see for instance [86]).

To highlight the connection between star formation and gas outflows we decided to produce an evolutionary plot of the star formation rate surface density (SFRD) in units of $M_\odot\,\mathrm{yr}^{-1}\,\mathrm{kpc}^{-2}$ that occurs within a radius of $R_{(70\%)SFR}$ as a function of the time covered by the various snapshots of the simulation in Fig. 4.8. The star formation rate density (namely Σ_{SFR}) is an integral constraint averaged within a radius within which the galaxy has a certain percentage of SFR at any given snapshot. Specifically, we derived this quantity for each snapshot as

$$\Sigma_{SFR}(R_{(70\%)SFR}) = \frac{SFR}{\pi\, R^2_{(70\%)SFR}}\ . \tag{4.1}$$

Therefore the profile in Fig. 4.8 shows the temporal evolution of the amount of stellar formation density occurring in the galaxy within a radius $R_{(70\%)SFR}$. There are two factors that can increase or decrease Σ_{SFR}: one is related to the variation of the radius $R_{(70\%)SFR}$ and one related to SFR during the temporal evolution of the galaxy. In fact, it is possible to notice from a comparison between Fig. 4.8 and Fig. 4.5 and Fig. 4.7 that to a growth of Σ_{SFR} corresponds a decrease in $R_{(70\%)SFR}$ and an increase in SFR at the same time. This is evident from the peaks in the Fig. 4.8 and the corresponding decreases/increases in Fig. 4.5 and Fig. 4.7 respectively, in the time intervals $400 \leq t \leq 550$ Myrs and $750 \leq t \leq 850$ Myrs. On the other hand, the

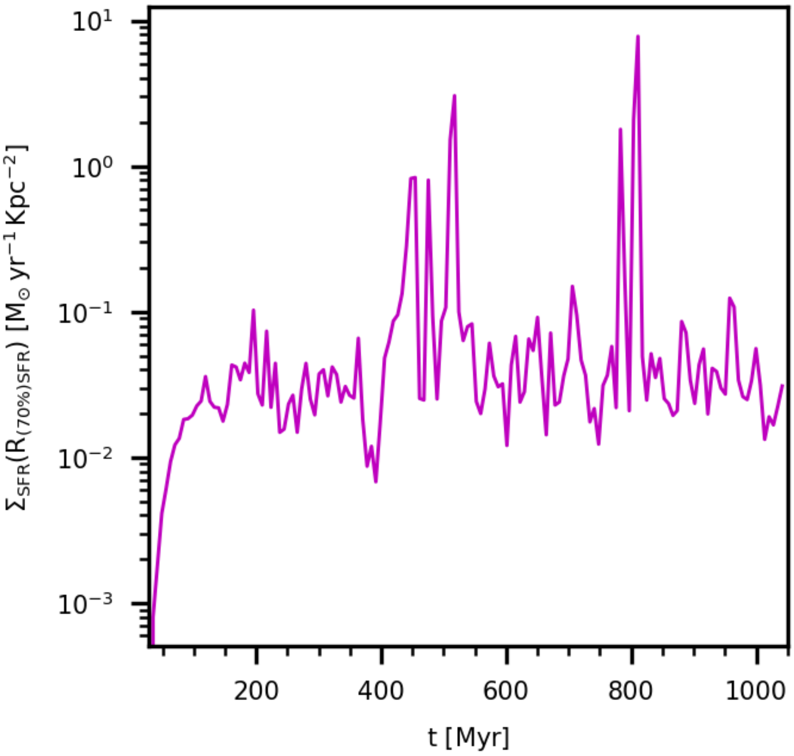

Figure 4.8: Star formation rate surface density within the radius $R_{(70\%)SFR}$ (that is the radius enclosing 70% of the total star formation rate of the galaxy) as a function of time of the simulated MW-like galaxy. The line show the instantaneous star formation rate density, calculated as the sum of the SFRs of each individual gas cell compared to the area within which 70% of the stellar formation takes place at a given time t (see equation (4.1)). The large peaks around 500 Myrs and 800 Myrs indicate that at those ages the galaxy exhibits regions where the stellar formation is very concentrated. By looking at the trend of the curve in Fig. 4.5 at the same intervals of time, we can realize that these peaks correspond to small values ($\sim 0.5 - 1$ kpc) of the radius $R_{(70\%)SFR}$, indicating that outflow phenomena have efficiently ejected gas from the star-forming disk thus limiting the stellar formation only in some confined areas of the galaxy (particularly in the central regions).

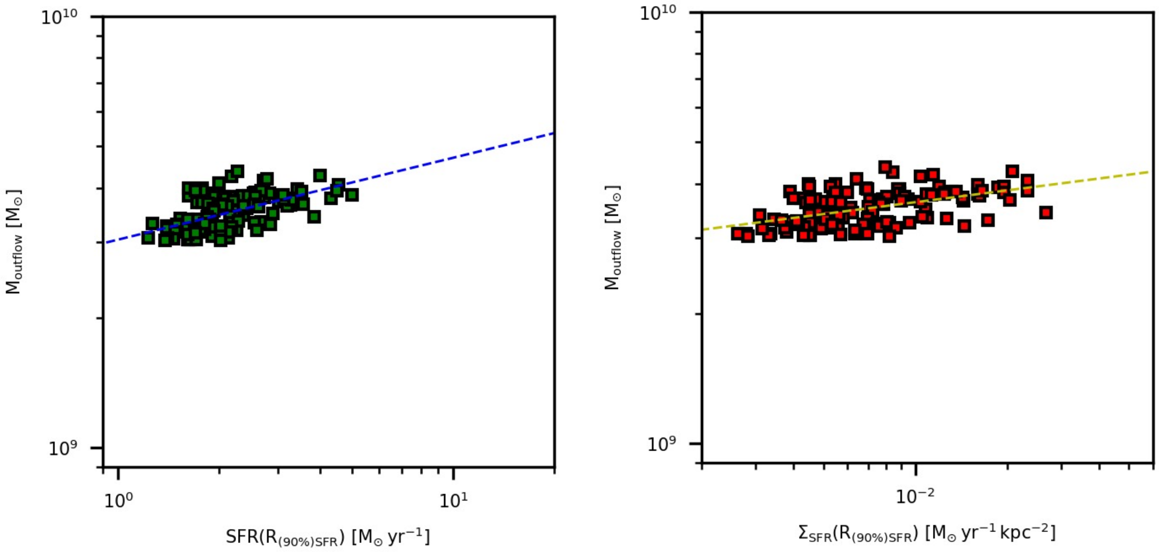

Figure 4.9: Scatter plot of the amount of gas mass outflow within a height of the disc of $|z| < 5$ kpc with respect the SFR (left panel) and the SFRD (right panel) that the simulated galaxy yields at each temporal snapshot within a radius where 90% of the star formation takes place. Both panels show an approximately linear relationship (in log-log space, shown with dashed lines in the panels) between the two quantities (see main text for details). These results also suggest that there is no critical value of SFR or SFRD above which the mass of the outflowing gas abruptly increases.

curve behaviour in the other zones of the plot 4.8 remains roughly constant at a level of $2\times10^{-2} < \Sigma_{SFR} < 4\times10^{-2}$ M$_\odot$ yr^{-1} kpc^{-2}, indicating that thanks to supernova feedback SF reaches a regulated state. In particular, this suggests that the amount of gaseous material that is ejected from the star-forming disk is approximately compensated by the amount of gas that re-enters in the mid-plane of the galaxy.

Once we obtained the information on the evolutionary trend of the $SFR(R_{(70\%)SFR})$ and $\Sigma_{SFR}(R_{(70\%)SFR})$, it was not difficult to derive the information about $SFR(R_{(90\%)SFR})$ and $\Sigma_{SFR}(R_{(90\%)SFR})$ over time with minimal modifications of the previous analysis. This was useful in order to find a possible relationship that would connect the $SFR(R_{(90\%)SFR})$ (or $\Sigma_{SFR}(R_{(90\%)SFR})$) with the evolution in time mass of outflowing gas located at a height from the plane of the disk equal to $|z| < 5$ kpc[4]. The idea is to search for a possible correlation that highlighted the existence of a certain critical value of $SFR(R_{(90\%)SFR})$ (or $\Sigma_{SFR}(R_{(90\%)SFR})$) above which gas outflow episodes would occur in the galaxy. Following this line of reasoning, we decided to generate a scatter plot for these quantities

---

[4] We preferred to use 90% of the total SFR of the galaxy to account for the large majority of the star formation activity within the disk.

that we show in Fig. 4.9.

In the left panel is reported the relation between the mass of outflowing gas located at a height from the plane of the disk equal to $|z| < 5$ kpc as a function of SFR (left panel), whereas the right panel shows the same relation in terms of the SFR density. The green squares (left panel) and the red squares (right panel) in the graphs represent the values assumed by these quantities for each simulation snapshot, and they approximately tend to be arranged along a linear relationship in log-log space (shown as dashed lines in the figure). The least square fit returns the following relations

$$\log\left(\frac{M_{outflow}}{M_\odot}\right) = 9.48 \,+\, 0.19 \,\log\left(\frac{SFR}{M_\odot\,\mathrm{yr}^{-1}}\right) \,, \tag{4.2}$$

and

$$\log\left(\frac{M_{outflow}}{M_\odot}\right) = 9.74 \,+\, 0.09 \,\log\left(\frac{SFRD}{M_\odot\,\mathrm{yr}^{-1}\,\mathrm{kpc}^{-2}}\right) \,, \tag{4.3}$$

in terms of SFR and SFRD, respectively. This preliminary analysis do not suggest the existence of any threshold value for a possible SFR_{crit} or $SFRD_{crit}$ above which conditions for gas outflows are present in the system. In future work, it could be very interesting to compare this kind of results with other studies related to other simulations of galaxies of this type, or observational constraints (see for instance [87]).

Finally, another interesting model test that we decided to carry out, in order to quantify the validity of the model used, was to verify the ability to regulate in time the star formation activity that takes place within the simulated galaxy. To do this we decided to relate the $\Sigma_{SFR}(R_{(90\%)SFR})$ with the projected density of the gas Σ_{gas} localized within a height from the disk plane equal to $0 < |z| < 5$ kpc (and the condition $R < 50$ kpc to consider all the SF occurred into the galaxy over time) and comparing this relationship with the Kennicutt-Schimdt relation [88]

$$\Sigma_{SFR}(R_{(90\%)SFR}) \;=\; 2.5 \times 10^{-4} \left(\frac{\Sigma_{gas}}{1 M_\odot\,\mathrm{pc}^{-2}}\right)^{1.4 \pm 0.15} \quad [\mathrm{M_\odot\,yr^{-1}\,kpc^{-2}}] \,. \tag{4.4}$$

The idea is to compare the trend of the simulated data with the one expected by the observations (see also [68]).

In Fig. 4.10 we report this comparison generating a scatter plot in which the colored lines represent the Kennicutt-Schmidt relation with different slopes (green correspond to a slope of 1.4, yellow to 1.25, and red 1.55), while the orange squares represent the trend of the simulation. What emerges is a good comparison between the feedback

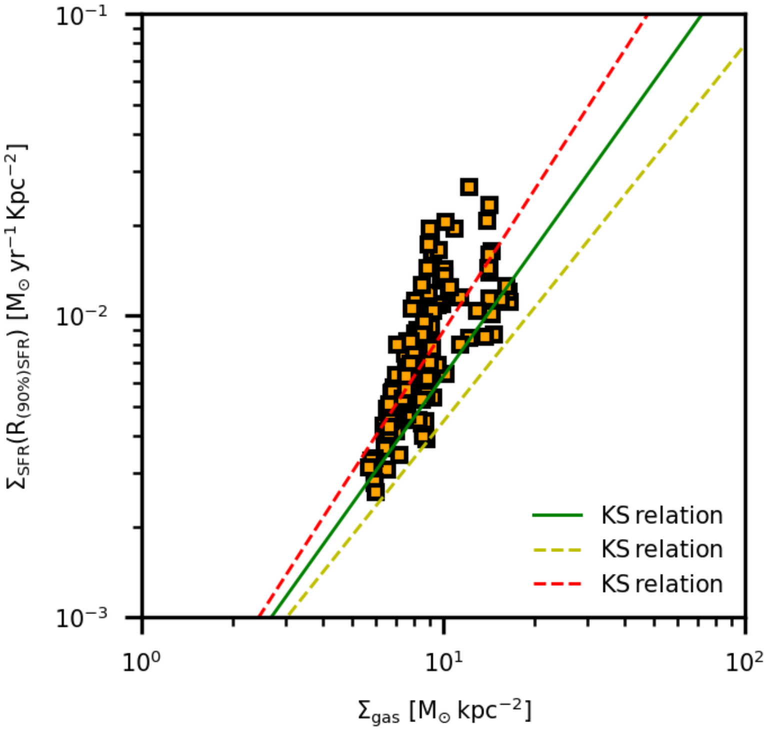

Figure 4.10: Comparison between the simulation results in terms of $\Sigma_{SFR}(R_{(90\%)SFR})$ as a function of Σ_{gas} (considering a region near the disc between $0 < |z| < 5$ kpc) and the Kennikutt-Schmidt relation based on the observation of a sample of MW-like SF-galaxies, in order to verify the goodness of the model utilized in the regulation of the phenomenon of SF. The green line and the two dashed lines (red and yellow) are obtained using equation 4.4 observationally derived in [88] varying the slope in the range 1.4 ± 0.15. The disposition of the orange squares represents instead the trend of the simulation results. A good agreement between simulation results and the observations can be inferred from this comparison.

model used in the simulation and the original sample of star-forming galaxies analyzed by Kennicutt. In fact, even if the disposition of the orange squares turns out to be steeper than the observational slopes, the obtained values are consistent with the KS relation. The deviation of the squares from the straight lines undoubtedly depends on the model used and could be indicating that the feedback in our simulation is slightly less efficient than it should be in regulating star formation in the galaxy. Notwithstanding this slight tension, this comparison is further confirmation of the soundness of the SMUGGLE model used for the implementation of the different physical processes that occur in the simulation during its temporal evolution.

4.4 SN rates and energy/momentum injection into the gas in the disc

In this section of the thesis we will mainly focus on the mechanical effects generated by the stellar feedback from SN on the gas present in the galaxy disc. In particular we analyze the trend of the SN explosion rate (both type-Ia and type-II) in the whole simulation time, the injected energy and momentum imparted to the gas in its vertical motion with respect to the galaxy plane, and the efficiency with which this happens. This analysis is very important precisely because the SN events are one of the most incisive mechanisms at the origin of gas outflows from galaxies [84].

To better understand how SN generate galactic-scale gas outflows, firstly we have chosen to compute a 1D histogram of the "z-component" of kinetic energy (i.e. $E_z = \frac{1}{2}\, m\, v_z^2$, with m being the gas mass) of the gas and compare it with the typical energy released by the SN explosion (that is $E_{SN} = 10^{51}$ erg), in order to actually single out which fraction of the energy released by SN explosions went into the vertical motion of the gas. To do this, we consider the number of SNs that occurred within a specific snapshot, for instance the snapshot 100 that corresponds to an instant of time of ~ 0.7 Gyr from the beginning of the simulation (this instant was also selected for other figures such as Fig. 4.1), in which we are confident that a gas outflow phenomenon is present on a galactic scale. The resulting histogram (shown in the left panel of the Fig. 4.11) has been realized extracting the component of the velocity along z-axis associated to the mass of gas present in the system – subtracting also the average velocity as discussed in the section 4.1. We then evaluated the kinetic energy E_z associated to each gas cell and we generated a histograms weighed by gas mass for all gaseous cell (black curve) and for different temperature cuts (colored curves) to distinguish different gas phases.

As highlighted by the different curves in Fig. 4.11 (left panel), in this specific snapshot, the contributions of the various gas phases tend to remain in terms of energy E_z below the value of the energy injected by a single SN event which is $\sim 10^{51}$ erg, which is taken as reference. This is shown by the peak around $\sim 10^{49}$ erg of the cold (blue curve) and warm (yellow curve) phases. However, a non-negligible amount of warm and hot (red curve) gas, exhibits a kinetic energy along the z-axis about a factor of 100 above the typical energy release from a single SN explosion, indicating that these gas phases can receive a substantial amount of energy from stellar feedback.

Focusing on the different curves of the figure, we have that the black curve represents the entire amount of gas mass with velocity component v_z outflowing from the plane of the galaxy, while in the other curves we made cuts in temperature to highlight the cold ($10^2 < T < 2 \times 10^3$ K), warm ($2 \times 10^3 \leq T < 4 \times 10^5$ K) and hot ($T \geq 4 \times 10^5$ K) gas components. It is worth noting that below $E_z \leq 10^{51}$ erg (i.e. the typical energy injected into the gas by a single SN event) there are the highest values assumed by the blue and yellow curves indicating that most of these gas remains possibly confined in the galactic disk having not enough energy to escape from it. Instead, above $E_z > 10^{51}$ erg only the hot and warm phases are present with a significant mass, whereas the curve of the cold gas declines much faster.

To accentuate the trends of the different curves we have decided to make a further cut of the gas outflow mass above a certain height from the disc plane, so as to highlight the amount of gas that is already inside ($0 \leq |z| \leq 2$ kpc) and outside ($2 \leq |z| \leq 10$ kpc) the disc region in the same snapshot, as shown in Fig. 4.12. The panels on the left and on the right side of the Fig. 4.12, show that the trend of the curves deviate appreciably from the plot previously analyzed (Fig. 4.11, left panel). In fact in this way we are able to easily distinguish the amount of gas that at ~ 0.7 Gyr is contained within the disk region or not. In particular, from the left panel we deduce that most of the gas contained in the disc region is in a cold and (mainly) warm state, while the hot phase is much less present even if, on average, it has higher kinetic energies.

Looking instead at the right panel, we can immediately see that outside the disk region there is very little high-energy cold gas ($\sim 10^{48} - 10^{50}$ erg) possibly ejected as a result of feedback from SN. Moreover, a higher amount of hot and (mainly) warm gas is significantly present outside the galactic disc.

The procedure used to generate the right panel of the Fig. 4.11 is the same followed for the evaluation of the kinetic energy, but in terms of the amount of the momentum I_z of gas cells is imparted to the vertical direction. In particular, we point out that the z component of the momentum $I_z = m\, v_z$ arising as the result of stellar feedback is a quantity easier to estimate than the planar momentum components. This is because, unlike the latter, it is not affected by the rotation of the disc and therefore it is necessary to subtract only the average motion gas motion that (as we have seen in section 4.1)

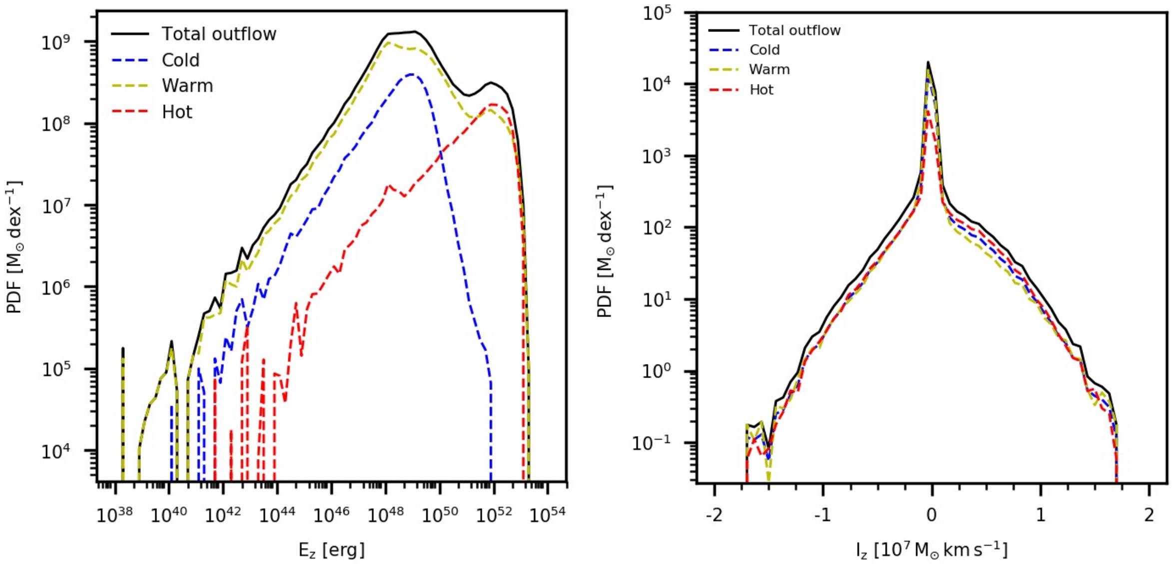

Figure 4.11: 1D histograms of the gas mass-weighted PDF as a function of the z-axis component of kinetic energy E_z (left panel) and momentum I_z (right panel), respectively. Both panels are evaluated at the snapshot 100 which corresponds to a time of ~ 0.7 Gyr. All gas cells having an outflowing velocity component are considered as shown by the black curves. To these cells temperature cuts were applied to differentiate between the three gas phases: cold (blue curve), warm (yellow curve), and hot (red curve). The left panel gives us an idea of the E_z energy associated with the various phases of gas and shows the presence of a peak at around $\sim 10^{49}$ erg for the warm and cold gas. This indicates that most of the gas has a E_z which is 2 orders of magnitude below the typical energy released by a single SN explosion (i.e. 10^{51} erg). However, a substantial amount of hot and warm gas is present around a value of $E_z \sim 10^{52}$ erg showing that, at this simulation time, stellar feedback was able to inject an energy about a factor of 10 times those injected by a SN event. The right panel shows that most of the multi-phase gas is in a state of equilibrium, being the different curves peaked at the zero point of the momentum I_z. Anyway, the wide range of values assumed by I_z (i.e., $|I_z| < 10^8\,\mathrm{M_\odot\,km\,s^{-1}}$) indicates that a fraction of the momentum imparted by the SNae is acquired by the various phases of gas (as a reference the typical momentum I_z imparted by a single event of SN is equal to $4-5\times10^5\,\mathrm{M_\odot\,km\,s^{-1}}$, [89]).

turns out to be $\sim 0.1\,\mathrm{km\,s^{-1}}$ only. We chose this component of the momentum to see if the model is actually able to drive outflows of gas outside the disk plane, in analogy with the analysis of E_z. The typical (terminal) momentum imparted by a single event of SN typically corresponds to $\sim 4 - 5 \times 10^5\,M_\odot\,\mathrm{km\,s^{-1}}$ (see e.g. [89]). So, observing the plot we note that the values assumed by the component of the momentum along z-axis of gas (of the order of $|I_z| \leq 10^7\,M_\odot\,\mathrm{km\,s^{-1}}$) represents the momentum typically released by hundreds of SN explosions. The peak of the curve at the zero point of the momentum I_z indicates that most of the gas present in the inner part of the galactic system tends to be in equilibrium, whereas the components of gas which have a substantial amount of I_z ($> 5 \times 10^6\,M_\odot\,\mathrm{km\,s^{-1}}$) are probably expelled from the galactic plane. We mention that the trend of the vertical component of the momentum is is similar to what we discussed for the PDF of the gas mass as a function of v_z presented in Fig. 4.1.

To conclude our analysis we now focus on the properties of main mechanism of expulsion of gas outside the galactic plane, i.e. SN explosions. As shown in the right panel of Fig. 4.12 the amount of gas outside the disc region is not abundant in terms of mass and this suggests that not all the energy produced by SN explosions ends up in the vertical motion of the gas. To further show that this is the case, we have decided to visualize the temporal trend of the number of SN (of both types) that explode during the simulation (as shown in fig. 4.13). We have then used this information to determine the efficiency of energy input from SNae into the vertical motion of the gas. We will present this aspect later in fig. 4.16.

Before commenting the figure, we would like to point out that the SMUGGLE model is not implemented to directly give details like the spatial information of the number of SNae exploded at each snapshot of the simulation. Indeed, we can basically access the information about the cumulative number of exploded SN. Specifically, the output of our simulation records only the cumulative number of SN exploded for each stellar particle at a given (snapshot) time. Therefore the only information we can access is bounded to the count of number of SNs exploded inside the star particles for every snapshot. Since the temporal difference between two consecutive snapshots is about 7 Myrs, it is possible to know how many SN exploded during that time frame, but the exact time of the explosion cannot be resolved.

With this information we can actually track the number of SN events occurred be-

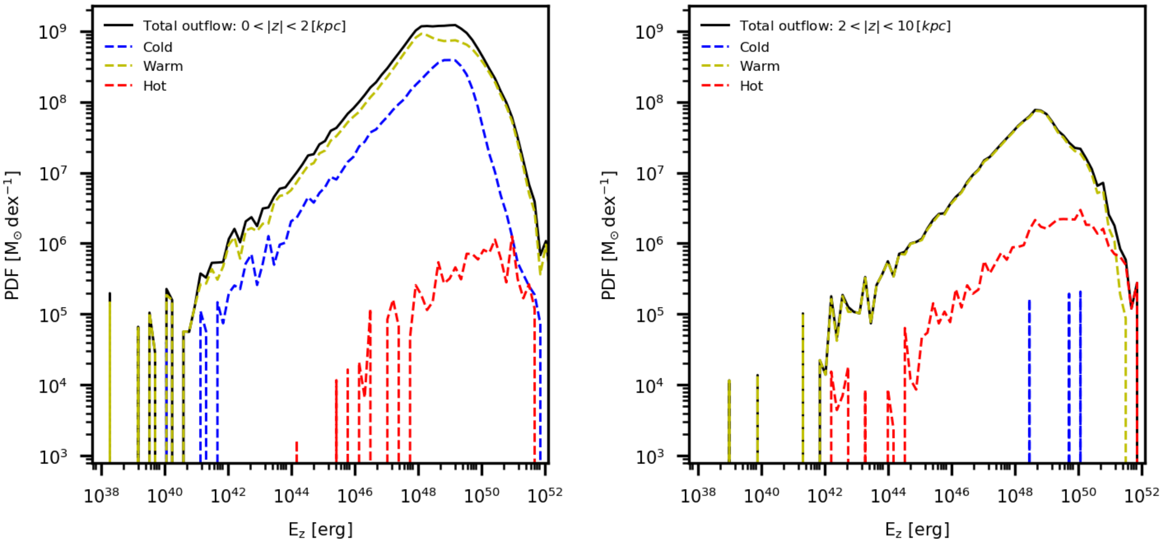

Figure 4.12: 1D histograms of the gas mass-weighted PDF as a function of the z-axis component of kinetic energy E_z referred to the snapshot 100. For the meaning of the line styles and colour, please refer to Fig. 4.11. In this figure we have selected the mass of gas present in a region inside the disc ($|z| \leq 2$ kpc; left panel) and outside the disc region ($2 \leq |z| \leq 10$ kpc; right panel), having velocity v_z outflowing from the galactic plane. We also made different cuts in temperature to distinguish gas phases. On the left panel the figure highlights that most of the gas near the disc region has kinetic energies along the z-axis below the energy threshold released by a single SN (i.e., $E_z < 10^{51}$ erg). On the right panel we can easily see that only warm (yellow curve) and hot gas (red curve) have energies above the energy threshold released by a SN explosion, indicating that a fraction of this hotter gas may have a boost sufficient to leave the galactic system. The cold gas (blue curve) is mainly located in the disc region, but however, a little fraction is situated outside the disc, this can be attributable to feedback from SN which, following the explosion, was able to sweep away this gas component even at great distances from the galactic plane.

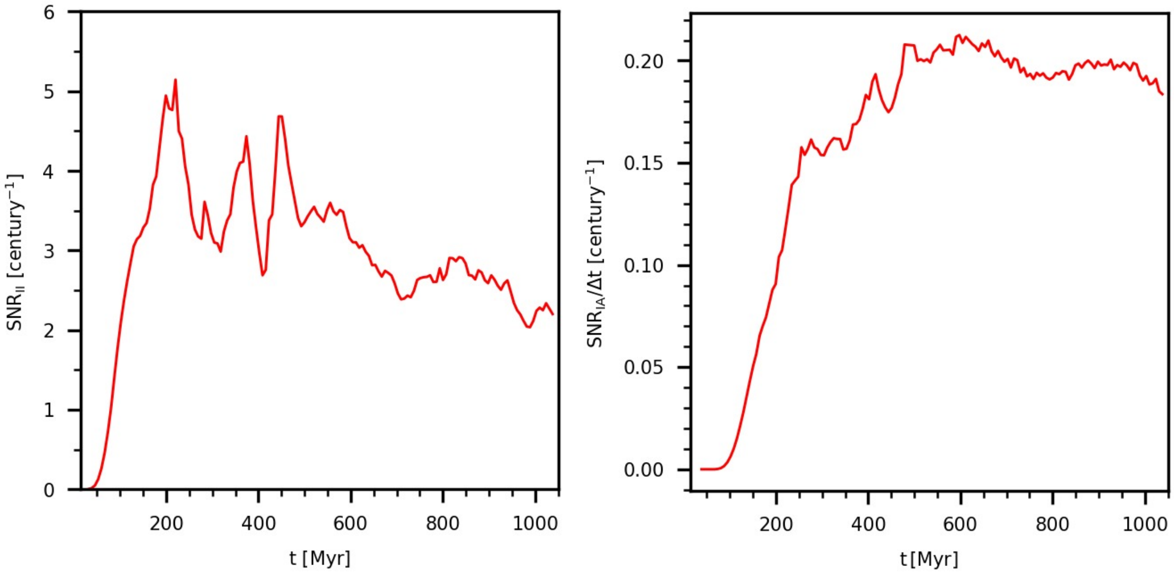

Figure 4.13: Temporal evolution of SN type-II (left panel) and type-Ia (left panel) explosion rate. Looking at the left panel, the SNR_{II} evolution shows that initially the galaxy as a result of fervent stellar formation activity generates more SN events per century as shown by the rising trends and higher peaks of the curve at a time < 500 Myrs. The steep slopes of the curve in this region of the graph indicates that the SN feedback generates outflow phenomena which make gas unavailable for SF, ultimately resulting producing a smaller number of SN events. As time progresses the curve tends to decrease, the variations of the peaks are less pronounced and the galaxy settles to a level equal to ~ 2 SN per century. Looking at the right panel, the SNR_{Ia} trend shows that the galaxy takes about 500 Myrs before settling at a higher generation level of these phenomena. The curve maintains an ever increasing trend until it flattens at a time > 500 Myrs to a value of about 2 SNIa per millennium. As a result, we expect these events (much rarer than SNIIs) contribute significantly less in terms of energy/momentum transferred to the gas in the simulation.

tween consecutive snapshots i and $i-1$ by simply subtracting the cumulative number of SN which exploded from the beginning of the simulation until the i snapshot with those exploded until the $i-1$ snapshot. So, we calculate the SN rate explosions in units of yr^{-1} by subtraction of the cumulative number of SN between two consecutive snapshots and dividing this result by the time interval between the two snapshots ($\sim$ 7 Myrs). In this way, it is possible to produce two distinct graphs of the SN rate exploded in the simulation, distinguishing between the SNII and SNIa as shown in Fig. 4.13.

The curve of the left panel in Fig. 4.13 shows the temporal evolution of the explosions rate of SNII per century. The steep growth of the curve in the first 200 Myrs (culminating with the highest peak of the curve at $\sim$ 5 SN per century), is linked to the peak localized in a very similar time range of the SFR (Fig. 4.7). Following an intense star formation activity of SF, we anticipate a consequent high number of SN exploded as type-II. However, we expect that between the creation of a new star particle and the total number of SNII explosions within it, there will be a time shift of about 40 Myrs, as discussed in section 3.3, and so we also expect that the peaks of the curves of the two graphs in question will tend to be shifted by this amount of time. So, when the curve in the left panel of Fig. 4.13 follows an increasing trend, the star formation rate will decrease as a consequence of SN feedback, which generates powerful outflow phenomena sweeping away a non-negligible fraction of the gas that can be used for SF. On the other hand, a decrease of the curve indicates that SN activity decreases, so a part of the expelled gas falls back into the galactic plane and it eventually available again for SF.

In particular, we know (see [10]) that on average the cold gas expelled from the galactic plane as a result of SN feedback takes $\sim$ 100 Myrs before falling back into the disk (which corresponds to a dynamical time of the galaxy around its center). The exact period of time in which the gas falls back onto the disc depends on the scale height that the gas reaches before re-entering the galaxy. Moreover, as a result of the galactic rotation this ejected gas will not fall back to exactly the same point from which it was ejected, as it retains the angular momentum imparted by the disc's rotation thus deflecting its trajectory and falling back to other regions of the disk. Where the accreting gas impacts on the disc is very important because this affects the galaxy metal evolution. However, we emphasize that for simplicity in the simulation analyzed in this work the generation of new metals is not included. Moreover, we recall that the metallicity of

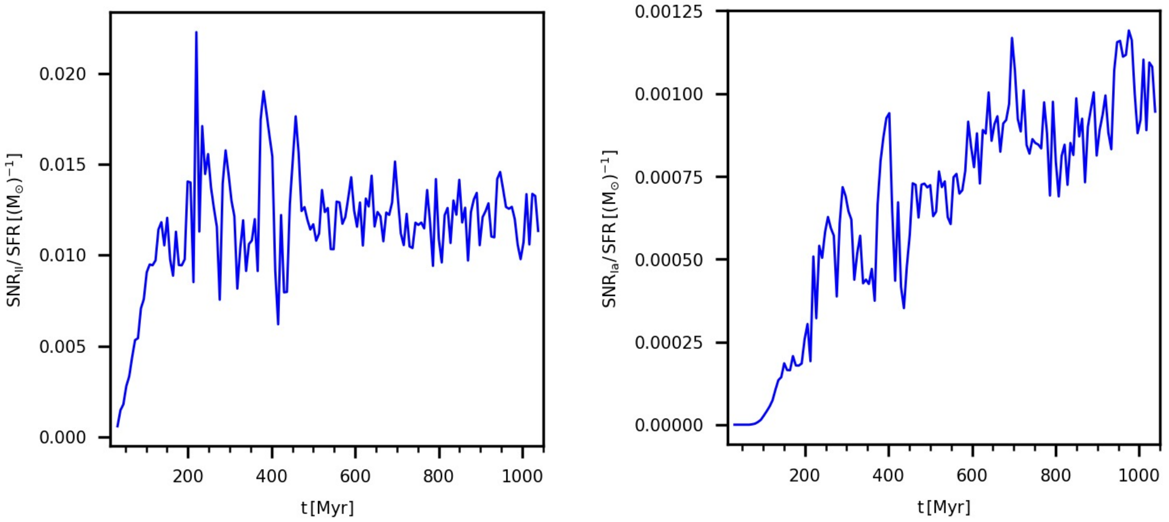

Figure 4.14: Evolutionary trends of the number of SNII (left panel) and SNIa (right panel) exploded per unit stellar mass formed as a function of time. The jumps in the curves are occurring because of the stochastic sampling of SN events implemented in SMUGGLE. The resulting trends and are in agreement with the findings obtained in [18] (Appendix A).

the gas present in the disc is fixed to solar metallicity, while the gas outside the galaxy has an extremely low ($Z \sim 0$) metallicity (see section 3.3). These choices were made because the simulated galaxy is isolated and therefore including the creation of metals would have generated new stars with artificially high metallicity. This shortcoming of the model will be addressed in future work.

Returning to the left panel of the Fig. 4.13, as time progresses, the trend of the red curve generally tends to decrease (as a consequence of the exhaustion of star-forming gas in the galaxy) until it settles at ~ 1 Gyr from the beginning of the simulation at a rate of ~ 2 SN per century^{-1}. This trend is consistent with observations as the expected SNII explosion rate for MW-like galaxies is around $1-2$ SN per century (see [85], [86]). The same procedures have been performed to track the rate of SNIa explosions, in which, as shown by the trend of the curve on the right panel in Fig. 4.13, there is an increase in the number of these rarer events as the simulation time progresses, until it settles at ~ 1 Gyr at about $1-2$ SNIa events per millennium. The rarity of these events reflects into a contribution in terms of energy and momentum imparted to the ISM of the galaxy much lower than the more frequent SNII explosions.

After the estimation of the explosion rate of SNII and SNIa over time, we relate these two quantities with the star formation rate calculated earlier in order to obtain

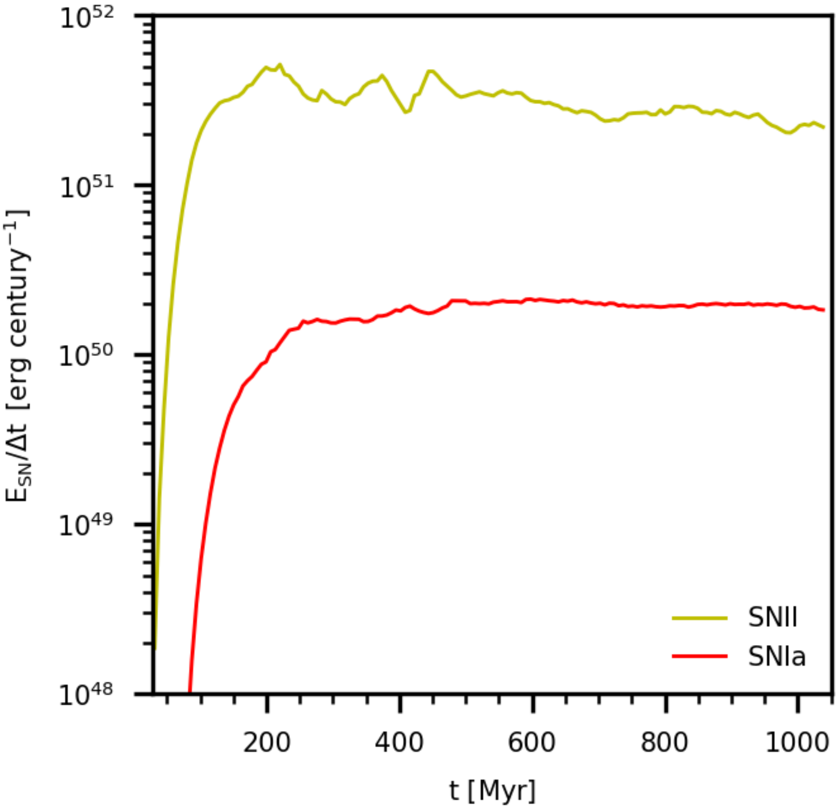

Figure 4.15: Evolutionary trends of the SNII (yellow curve) and SNIa (red curve) energy injection rate as a function of time. Comparing the trend of the two curves we can observe how the energy contribution released to the gas by these two channels of stellar feedback has a time delay of about 40 Myrs. In particular, we deduce from the trend of these curves that the main mechanism behind the gas outflow phenomena present in the galaxy, is linked to the SNII events as they inject a rate of energy into the gas that is more than 10 times greater than the contribution made by the SNIa.

the number of SN events per solar mass as a function of time. With regard to the previously obtained results, we expect the value obtained from SNR/SFR (in units of $M_{\odot}^{-1}$) to be of the order of 0.01 $M_{\odot}^{-1}$ and approximately constant for SNII and of the order of 0.001 $M_{\odot}^{-1}$ with an increasing trend with time for SNIa. These trends are mainly given by the choice of the IMF discussed in section 3.3 and the compatibility between the results obtained and those expected reinforce the basic soundness of the simulation model adopted, as shown in the Fig. 4.14.

With regard to what we have just discussed, we expect that there will also be a greater contribution from type-II than type-Ia SNae in terms of the amount of energy injected to the gas. The graph shown in Fig. 4.15 actually confirms this trend. In the figure is presented the evolutionary trend of the rate of energy injection of SNae as a function of time for both SN types. We do so simply by using the information linked to the number of SN exploded in successive snapshots, multiplying this quantity by the typical energy released by a single SN event ($E_{SN} = 10^{51}$ erg) and dividing the value obtained by the time that passes between successive snapshots (~ 7 Myrs). In particular, we note that the yellow curve related to the rate of energy injection by SNII explosions quickly increases (in less than 100 Myrs from the beginning of the simulation) until it settles at about $\sim 3 \times 10^{51}\,\mathrm{erg\,century^{-1}}$, indicating that this kind of SN events start exploding efficiently as soon as the first stellar particles are created in the simulation. The red curve showing SNIa rates shows a less steep rise before settling at a constant level of energy injected rate $\sim 1 \times 10^{50}\,\mathrm{erg\,century^{-1}}$ at a time > 250 Myrs. As evidenced by the different heights reached by the curves in the graph, the amount of energy injected into the galaxy's gas by the SNIa is about one order of magnitude lower than the contribution made by SNII explosions.

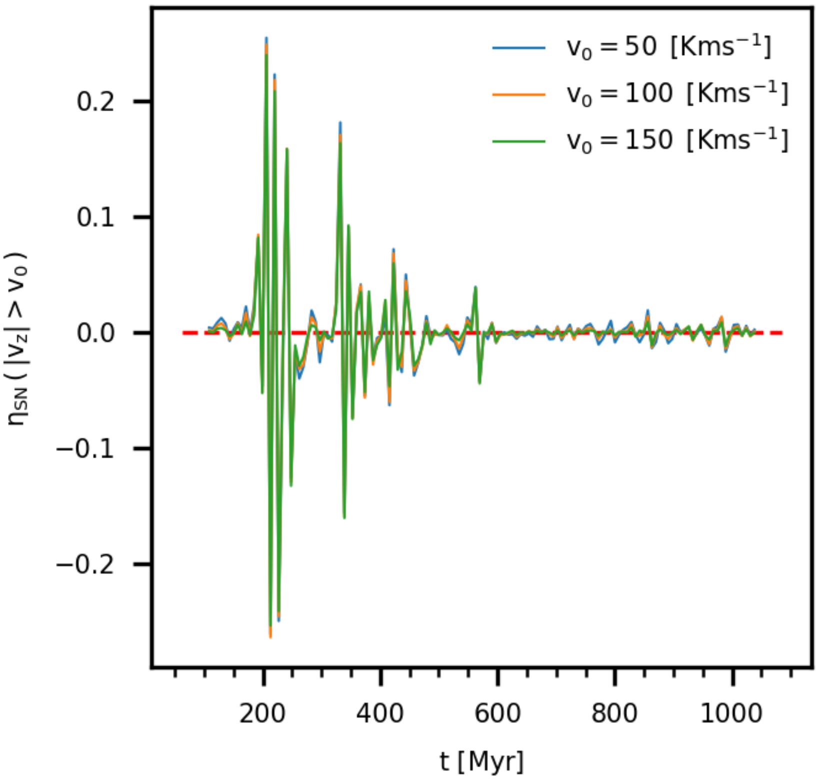

Figure 4.16: Evolutionary trend of SN energy release efficiency over time. We selected gas cells having a velocity component $|v_z|$ exiting from the galactic plane but located near the galaxy at a height from the disk $|z| < 2$ kpc. We also made three different velocity cuts, namely, $|v_z|$ greater than $50\,\mathrm{km\,s^{-1}}$ (blue curve), $100\,\mathrm{km\,s^{-1}}$ (orange curve), $150\,\mathrm{km\,s^{-1}}$ (green curve), in order to consider the gas having a non-negligible kinetic energy component E_z attributable to the energy released by SN feedback. Once the simulation is started, the galaxy begins to form stars at an increasing way generating an increasing number of SN events, until in the time interval between $150 < t < 600$ Myrs substantial peaks are evident. These indicate a high retention efficiency ($\sim 10 - 20\%$) of the SN feedback energy and suggest the presence gas outflow phenomena outside the galactic plane. The negative values assumed by η_{SN} mean that the gas has a kinetic energy E_z lower than in the previous time, indicating that feedback activity is low or inefficient at transferring energy to the gas. As the galaxy ages, over $t > 600$ Myrs, the fuel in the galaxy begins to run out and all phenomena (SF, SN, outflow/inflow gas) tend to smooth out. In fact, all curves oscillate around the zero point of the eta_{SN} efficiency, indicating that the galaxy has settled into a state of equilibrium in which it is more difficult for the gas to be ejected out of the galactic plane at large distances and therefore the ejected remains tendentially closer to the disk region.

In light of this result we decided to investigate the evolutionary trend of SN efficiency (see below for the definition of this concept) in Fig. 4.16. By SN efficiency we mean the fraction of the energy released by SN events that is actually retained in the vertical motion of the gas (essentially the kinetic energy E_z) during the life time of the simulated galaxy. We choose to combine both SN types because, as discussed in Fig. 4.13 and Fig. 4.15, we expect that the main energy/momentum contribution injected into the ISM by stellar feedback is mainly attributable to SNII events, whereas the contribution of SNIa is much lower but not completely negligible.

To obtain the figure, we initially chose a threshold speed v_0 and we selected all the gas cells above and below the galactic plane in a region near the disk (i.e. $|z| < 2$ kpc) having a perpendicular component of the velocity $|v_z|$ larger than this velocity threshold (i.e. with $v_z > v_0$ or $v_z < -v_0$). Then, we calculate the total kinetic energy $E_z(|v_z| > v_0\,,\,t)$ associated to these gas cell components (similar to what we discussed in the graphs in Fig. 4.11 and Fig. 4.12) for each snapshot of the simulation, and we compared the total energy E_z with the energy released by the SNs which exploded at each snapshot ($E_{SN}(t) = N_{SN}10^{51}$ erg) at any snapshots.

To estimate the SN explosion efficiency η_{SN} at each time, we need to consider that our code records only the cumulative number of SN exploded from the start of the simulation to a generic i snapshot considered. So, to recover the information about the total energy released by multiple SN events which occurred at a specific time, we need to subtract the cumulative number of SN exploded between two consecutive snapshots (similarly to what was discussed for the graphs in Fig. 4.13), and multiply it by the typical energy released by a single SN event, i.e. $\Delta E_{SN}(t) = E_{SN}(s_i) - E_{SN}(s_{i-1}) = (N_{SN}(s_i) - N_{SN}(s_{i-1}))\,10^{51}$ erg. Comparing the variation in the vertical "component" of the total kinetic energy of gas $E_z(|v_z| > v_0, t)$ with $\Delta E_{SN}(t)$ we obtain the SN explosion efficiency $\eta_{SN}(|v_z| > v_0\,,\,t)$ for a generic snapshot i as follows

$$\begin{aligned}\eta_{SN}\left(|v_z| > v_0, t_i\right) &= \frac{\Delta E_z(|v_z| > v_0\,,\,t)}{\Delta E_{SN}(t)} = \\ &= \frac{E_z(s_i) - E_z(s_{i-1})}{E_{SN}(s_i) - E_{SN}(s_{i-1})} = \\ &= \frac{E_z(s_i) - E_z(s_{i-1})}{[\,N_{SN}(s_i) - N_{SN}(s_{i-1})\,]\,10^{51}} \qquad (4.5)\end{aligned}$$

where $\eta_{SN}(|v_z| > v_0\,,\,t_i)$ is a dimensionless number that depends exclusively on tje velocity threshold v_0 we assumed. This simple calculation (equation (4.5)) is performed for each snapshot of the simulation in order to reconstruct the variation of the efficiency of energy release into the ISM by SNae over time. We choose three different values for the quantity v_0 that are equal to 50, 100 and 150 $\mathrm{km\,s^{-1}}$.

By looking at Fig. 4.16, it is evident that the three coloured curves, which identify the different v_0 velocity cuts, tend to coincide, indicating that the gas receives approximately the same energy input from SN feedback regardless of the v_z velocity cut. The height of the peaks at a time < 600 Myrs indicates that the SN were considerably more efficient in producing gas outflows in the first half of the simulation. In other words, the peaks are an indication of a period of relatively high star formation and of a consequent SN energy release that is efficiently retained by the gas.

The decreasing trend of the curves generally indicate that temporarily the SN activity is less present, thus resulting in a less feedback energy that can be coupled to the gas. Indeed, the negative values assumed by η_{SN} indicate that in those time intervals the gas effectively loses kinetic energy along z. In these evolutionary phases of the galaxy, a smaller number of these explosive events are expected to be found. As time progresses the galaxy has consumed a significant fraction of its gas. Therefore, SN events and gas outflow are less present and all curves oscillate around the zero point of the efficiency η_{SN} with an amplitude of $\sim 0.01 - 0.02$. This is attributable to the decrease in kinetic energy of the E_z gas that falling back into the disk is no longer relaunched, as SN events in the galaxy decrease out as the star-forming fuel becomes depleted. Even when SN feedback is particularly effective, no more than $\sim 20\%$ of the injected supernova energy is retained as kinetic energy by the vertical motion of the gas.

All in all, the values obtained for the efficiency of SN feedback are in a range of values $\eta_{SN} < 0.2$), i.e. an efficiency in the transfer of energy from SN to the ISM of $< 20\%$, in line with other studies [95]. On the other hand, we expect this efficiency to largely depend on the conditions in which SNae exploded (e.g. if the energy injection occurred in a single event or in multiple and close SN events). The analysis of the factors that can impact the values of η_{SN} is certainly an interesting avenue to explore as a a possible follow-up investigation of this thesis work.

In analogy with the procedure used to generate the evolutionary trend of SN energy retention efficiency η_{SN}, we also decided to determine the I_z momentum efficiency im-

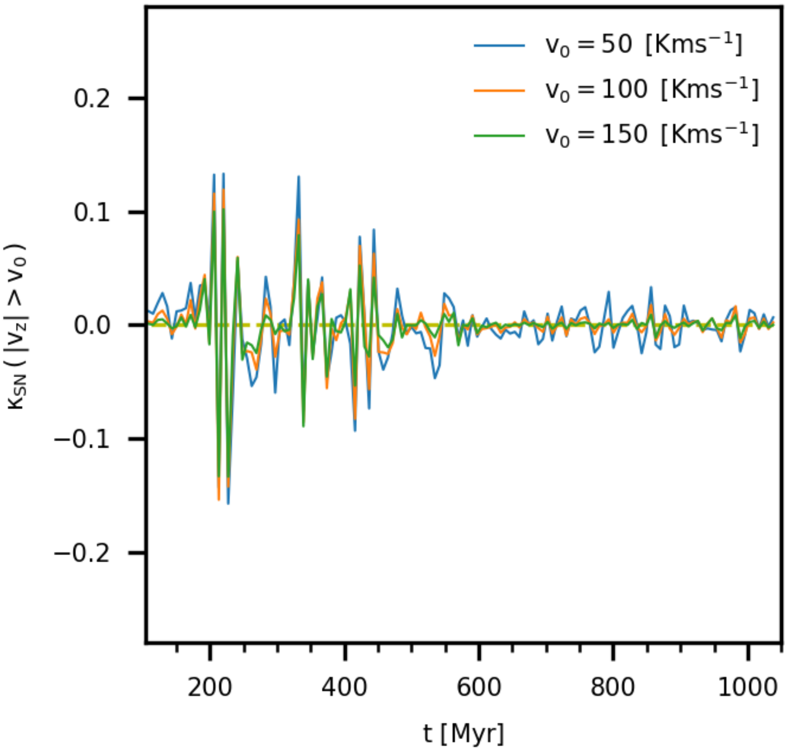

Figure 4.17: Evolutionary trend of SN momentum efficiency κ_{SN} as a function of time. We selected gas cells having a velocity component $|v_z|$ exiting from the galactic plane but located near the galaxy at a height from the disk $|z| < 2$ kpc. We also made three different velocity cuts, namely, $|v_z|$ greater than $50\,\mathrm{km\,s^{-1}}$ (blue curve), $100\,\mathrm{km\,s^{-1}}$ (orange curve), $150\,\mathrm{km\,s^{-1}}$ (green curve), in order to consider the gas having a non-negligible momentum component I_z attributable to the momentum imparted by SN feedback. Similarly to the arguments reported in Fig. 4.16, the efficiency of the momentum imparted to the gas is large ($\sim 10-15\%$) in the first ~ 500 Myrs where the galaxy is especially active on all the fronts discussed in this work: SF, SN events and gas outflows on a galactic scale. Looking at the pronounced spikes in the graph (indicators of powerful outflow gas phenomena), we can see the presence of deep depressions as well in which κ_{SN} assumes negative values indicating that the galaxy needs time to reacquire the gas needed to create new stars and therefore generate SN explosions. As simulation time progresses, the efficiency oscillates around zero at values of a few percent, in analogy with what has been discussed in Fig. 4.16.

parted to the gas in the galaxy by SN feedback. Once again we considered all gas cells having a v_z velocity component in a region close to the galactic disk ($0 < |z| < 2$ kpc), made the same cuts in velocity v_0 as in Fig. 4.16 and calculated at each snapshot the I_z momentum associated to these gas components. Given that the SMUGGLE model has been structured in such a way to store the cumulative value of the momentum imparted by all the SN exploded in the simulation as a function of time, we have then derived the momentum contribution imparted by all the SN exploded in each snapshot (by subtracting the cumulative momentum value between two consecutive snapshots) and compared this to I_z momentum of the gas with $|v_z| > v_0$. In Fig. 4.17, we report the evolutionary trend of this SN momentum efficiency, in which the three different colored patterns indicate 3 cuts in velocity made to select the gas component of interest, and which correspond to the trends colored in blue for $|v_z| > 50\,\mathrm{km\,s^{-1}}$, in orange for $|v_z| > 100\,\mathrm{km\,s^{-1}}$ and in green for $|v_z| > 150\,\mathrm{km\,s^{-1}}$. Specifically, the highest peaks in the graph located in a time interval of $150 < t < 600$ Myrs, indicate that the gas acquired momentum I_z from the SN efficiently ($\sim 10 - 15\%$), indicating that the explosion of multiple SN events (generated by a more fervent SF activity in these temporal phases of the simulation) can generate gas outflows from the galactic plane. The negative values of κ_{SN} signal instead that in those temporal phases the galaxy had a lower supply of gas to generate new stars and therefore new SN events and the vertical momentum of the outflowing gas decreases consequently. We conclude by noting that the differences in the values of κ_{SN} for different velocity cuts are small, but more pronounced than in the SN energy efficiency case.

Chapter 5

Conclusions

The numerical modelling of the different components that make up a galaxy as a whole is very ambitious, because of the number of resolution elements that are needed to accurately represent a galaxy is very large and requires a non-negligible computational power and costs. In addition, the vast dynamic range and the multi-scale nature of the physical phenomena that play a key role in the characterization of these giants of the cosmos, make numerical modelling even more challenging. However, in the last decades enormous progress has been made in the execution of simulations about the formation and the evolution of galaxies thanks to more innovative numerical techniques that are able to deal with an increasing number of elements of the system and an increasing amount of data that can be analyzed at even more accurate levels of resolution. These methods have become increasingly important as a theoretical tool for investigating regimes that cannot be approached with analytical methods, but rather involve a non-linear and complex treatment of various physical processes. In addition, numerical simulations represent a powerful tool to test a wide range of theoretical galaxy formation and evolution models by comparing with observational data.

In our work, we specifically analyzed an idealized simulation of a Milky Way-like galaxy in a time interval of ~ 1 Gyr, placed in conditions of isolation within a dark matter halo (represented by a static gravitational potential), but excluding the presence of a galactic corona or a cosmological gas inflow. The choice of these simplified initial conditions for the galaxy allows us to simplify the study conducted in this thesis which analyzes the mechanisms at the basis of the gas outflows phenomena on a galactic scale, mainly due to SN feedback [84], examines the persistence of star formation activity within the galaxy for a simulated time of ~ 1 Gyr, and looks for possible connections between galactic outflows and star formation.

The numerical simulation of the galaxy analyzed in this work has been executed with the moving-mesh AREPO code [17] and performed with the use of the galaxy formation physics SMUGGLE model [18]. The latter is a model that, thanks to an explicit treatment of stellar feedback and star formation and the description of the multiphase gas in the ISM, produces gas outflows on a galactic scale self-consistently. However, as a result of the use of these numerical approaches and the choices made to set the initial conditions, the simulated galaxy investigated in this work does not include of many important physical processes (such as magnetic fields, photoionization of gas by old stars, cosmic rays (CRs) dynamics and its effects on the gas, to name the most prominent) and can offer only an approximate the description of the processes that take place below in the smallest resolved scale (i.e. pc-resolution scale [91]). In any case, the SMUGGLE model is able to effectively provide a physical prescription to describe the various gas components that make up the ISM of the galactic system in its different phases (cold, warm, and hot) and take into account a good spectrum of stellar feedback channels that actively concur in the structuring of the galaxy.

The aim of the thesis was to characterize the properties of galactic-scale outflows generated by stellar feedback. In particular, we have analyzed the key characteristics implemented in the SMUGGLE model regarding the main stellar feedback channels and focused on the injection into the gas by supernova explosions. This feedback channel is considered the fundamental mechanisms underlying the substantial variations in the structure of multiphase gas and the generation of powerful galactic-scale outflows in Milky Way-like galaxies.

From a first analysis of the dynamics of the gas in its vertical motion with respect to the galactic plane (Sec. 4.2), both within a region close to the star-forming disk (i.e. $|z| < 2$ kpc) and outside it (i.e. $|z| > 2$ kpc), we have verified that the simulation, taking a temporal snapshot representative of the state of the galactic system, was fully able to generate a multi-phase structure in the gas (in terms of temperature and mass abundance) that could be distinguished between and inflowing and outflowing gas components once appropriate cuts in velocity v_z were made. What emerges from this study is that most of the cold and warm phase of gas lies in the region of the disc in a range of about $|v_z| < 100\,\mathrm{km\,s^{-1}}$, while the hot phase is much smaller in terms of mass abundance and has a broad distribution in terms of v_z. Outside the disc region, a wide range of velocities ($100 < |v_z| < 1000\,\mathrm{km\,s^{-1}}$) can be reached by the warm and hot gas phases. Given these high speeds we expect that a fraction of this gas will be lost from the system as a result of a powerful outflow episode (the escape velocity being $v_e > 500 - 600\,\mathrm{km\,s^{-1}}$ at about the solar radius). However, the bulk of the ejected gas reaches lower speeds and will eventually fall back onto the galaxy disk.

Continuing our analysis, we have widened our study on the evolutionary trend of galaxy properties from the point of view of the phenomenon of star formation (Sec. 4.3) and the contribution of energy and momentum of SN feedback (both from the SNII and SNIa channels) to the gas in the galactic system (Sec. 4.4). In particular, we verified that the SMUGGLE model is to yield a star formation rate of $\sim 2\,\mathrm{M_\odot\,yr^{-1}}$ in accordance with current observational evidence for MW-like galaxies ([85], [86].), that the SF is present in the galaxy for in a time of $\sim$ 1 Gyr and that on average 50% SFR is contained in the innermost regions of the galaxy (within a radius of a few kpc) especially after $t >$ 500 Myrs. In addition, we also studied the evolution of the star formation rate surface density within different radii (nominally $R_{(x\%)SFR}$, where $x\%$ of the total star formation activity occurs). For the radius $R_{(x\%)SFR}$ we combined with the projected gas density $\Sigma_{gas}(R_{(90\%)SFR})$, and we were able to reproduce the Kennicutt-Schmidt relation, thus analyzing an important comparison between the results of the SMUGGLE model and the observations. Finally, we looked for a possible connection between the $\Sigma_{SFR}(R_{(90\%)SFR})$ and the mass of outflow gas contained within a height from the disk plane of $|z| <$ 5 kpc. The idea was to look for a relationship that would highlight a possible critical value for the star formation rate density above which gas outflows would be produced. The results showed that a weak trend is present, but did not find a threshold value. However, the results are only preliminary and further studies are needed for confirmation. We intend to pursue this interesting line of investigation in future work.

Equally interesting was the analysis of SN feedback and in particular the study of the efficiency with which this feedback channel injects“vertical” kinetic energy (E_z) energy and vertical momentum (I_z) to the gas in the disk and the subsequent generation of a galactic fountain flow resulting from this energy/momentum injection (Sec. 4.4). In this regard, we have produced several evolutionary trends to show the rate of SN explosions of both types over time, in which it appears that the simulation has been able to reproduce the values expected from the observations for galaxies such as the Milky Way – $\sim 2-3$ SNII per century and ~ 2 SNIa per millennium (see Fig. 4.13) – confirming once again the basic soundness of the SMUGGLE model. From the point of view of the energy released by SN events in the ISM, it is clearly evident that the main input channel is represented by the more frequent SNII compared to the rarer SNIa events. More specifically, SNII explosions inject energy into the gas in the disk at a rate that is ~ 10 larger than in the SNIa case. So the SNII represent the primary stellar feedback channel at the origin of gas outflows emerging from the disk plane in the simulation, especially in the first 500 Myrs where the fuel available to the galaxy to produce new progenitor stars of these SN is greater, and as show by the evolutionary trends, the galaxy exhibits a fervent activity of SF, SNII events and a more pronounced galactic-fountain cycle. Finally, we tried to understand, following the release of energy E_z by the SNs of both types, how efficiently this SN energy was retained by the gas in the galaxy as a function of time. To derive this evolutionary trend, we have selected the "component" of the kinetic energy associated to the motion along the z-axis of gas near the galactic disk ($|z| < 2$) and compared the values obtained to the energy released by all the SN exploded in each specific snapshot of the simulation. The intense gas outflow episodes occurring in the first 500 Myrs since the start of the simulation are justified by a quite large SN energy retention efficiency by gas components exiting the disc plane. This efficiency turns out to be of $\sim 10-20\%$, consistent with other studies (see, e.g., [95]). The same analysis was followed for the momentum efficiency along the z-axis I_z imparted to the gas by SN feedback, and resulted in a value of $\sim 15\%$ for the efficiency during the first 500 Myrs. It is at this stage of evolution that intense gas outflows, driven by SN explosion, occur in the simulation. Instead, with the aging of the galaxy this efficiency (as the energy efficiency of SN injected into the gas) oscillate around the zero point, suggesting that the fuel in the disk has been consumed or expelled from the system and that the galaxy has settled on a roughly constant (and lower) SF and SN explosion rate limiting the gas circulation on scales increasingly close to the disk region.

We point out that further and more in-depth analyses are possible with this type of simulations to better characterize the properties of the galactic-scale gas circulation generated by stellar feedback. For example, a more detailed study of gas kinematics is possible by generating two-dimensional histograms for all gas velocity components according to their position (i.e. position-velocity plot) in the galaxy at each time step. The results obtained could then further refined by studying of the cold gas kinematics via mock HI 21 cm observations. Basically this entails the generation of artificial HI cubes that can be smoothed with the angular resolution of a typical observation in order to measure the rotation curve of the galaxy at different heights from the disk plane and compare results to observations of nearby galaxies [96]. Another idea could be to investigate the typical gas densities reached by the different phases of the gas present at various heights from the disc plane and analyzing the resulting kinematics. This would allow us to to better understand the vertical structure, properties and kinematics of gas outside the disc plane, and therefore have a more complete understanding of the phenomenon of gas circulation on galactic scales.

Interesting problems emerge around the study of the gas cycle in star-forming galaxies, for example how various feedback channels can reproduce the observations of the so-called extra-planar gas [90]. The gas cycle in galaxies is also important at cosmological scales in the formation an evolution of disks (and galaxies in general), as well as the validation of the theoretical presence of a cosmological inflow gas (see [92], [94]), that supports and justifies the current observations regarding the constant rate of star formation by MW-like galaxies for almost their entire life-time. Concerning the latter point, the isolated galaxy analyzed in this work certainly shows that the absence of a sort of dynamic balance between gas outflows (that deplete the system of gas, that is potential fuel for star formation) and gas inflows from the outside (that supply the disk with a fresh supply of gas) leads the galaxy to rapid aging as it produces stars at an ever lower rate in just 1 Gyr. In future works it is conceivable to extend this idealized galaxy simulation to investigate more complex configurations that will consider processes that are currently neglected – such as cosmological gas inflow or the presence of a gas atmosphere around the galaxy (i.e. a galactic corona model) – and their influence on the global gas circulation. More specifically, the investigation of relations connecting gas outflows generated by SN events to the processes of star formation occurring in the disk might shed more light on the link between galaxies and their halos and their co-evolution in time. Indeed, more detailed numerical simulations, that possibly extend the applicability of the SMUGGLE model to the cosmological context as well, are actually needed to deepen our theoretical knowledge of the physical processes shaping the formation and evolution of galaxies.

Bibliography

[1] Weinberg S., Cosmology, Oxford University Press, (2008)

[2] Planelles S. et al., Large-Scale Structure Formation: From the First Non-linear Objects to Massive Galaxy Clusters, Science & Space Review **188**, 93, (2015)

[3] Planck Collaboration, XI. CMB power spectra, likelihoods, and robustness of parameters, A&A **594**, A11 , (2015)

[4] Rix H., W. Bovy J., The Milky Way's stellar disk: Mapping and modeling the Galactic disk, AAR 21:61, (2013)

[5] White S.D.M., Rees M. J., Core condensation in heavy halos: a two-stage theory for galaxy formation and clustering, MNRAS **183**, 341-358 (1978)

[6] Springel V., Frenk C. S., White S. D. M., The large-scale structure of the Universe, Nature **440**, 1137-1144 (2006)

[7] Borgani S., Krastov A., Cosmological simulations of galaxy clusters, **astro-ph/0906.4370**, (2009)

[8] Mayer L., Foreword: ASL Special Issue on Computational Astrophysics, astro-ph/0906.4485v1, (2009)

[9] Segers M. C. et al., Recycled stellar ejecta as fuel for star formation and implicationsfor the origin of the galaxy mass–metallicity relatio, MNRAS **456**, 1235–1258, (2016)

[10] Marasco A., Fraternali F., Modelling the HI halo of the Milky Way, A&A **525**, A134 (2011)

[11] Sanchez A. J. et al., Star formation sustained by gas accretion, arXiv:1405.3178, (2014)

[12] Nelson D. et al., The impact of feedback on cosmological gas accretion, arXiv:1410.5425, (2014)

[13] Madau P. et al., THE STAR FORMATION HISTORY OF FIELD GALAXIES, ApJ **498**: 106-116, (1998)

[14] Bregman J. N., THE GALACTIC FOUNTAIN OF HIGH-VELOCITY CLOUDS, ApJ **236**: 577-591, (1980)

[15] Shimizu T. T. et al., The multiphase gas structure and kinematics in the circumnuclear region of NGC 5728, MNRAS **000**, 1–29, (2019)

[16] Agertz O. et al., Fundamental differences between SPH and grid methods, MNRAS **380**, 963–978 (2007)

[17] Springel V., E pur si muove: Galilean-invariant cosmological hydrodynamical simulations on a moving mesh, MNRAS **401**, 791–851 (2010)

[18] Marinacci F. et al., Simulating the interstellar medium and stellar feedback on a moving mesh: Implementation and isolated galaxies, MNRAS **000**, 1–29 (2019)

[19] Springel V., Di Matteo T., Hernquist L., Modelling feedback from stars and black holes in galaxy mergers, MNRAS **361**, 776–794 (2005)

[20] Hopkins P. F., Quataert E., Murray N., The structure of the interstellar medium of star-forming galaxies, MNRAS **421**, 3488–3521 (2012)

[21] Chabrier G., The galactic disk mass budget. I. Stellar mass function and density, ApJ **554**, 1274-1281 (2001)

[22] Springel V. et al., The cosmological simulation code GADGET-2, MNRAS **364**, 1105–1134 (2005)

[23] Toro E. F., Riemann solvers and numerical methods for fluid dynamics, chapter1: the equations of fluid dynamics, 2nd edition (1999)

[24] Wendt J. F., Computational fluid dynamics, **chapter 2**, 3rd edition (2010)

[25] Schoenberg I. J., Contributions to the problem of approximation of equidistant data byanalytic functions: part A, Q. Appl. Math. IV 45-99, (1946)

[26] Frenk C.S. et al., The Santa Barbara Cluster Comparison Project: A comparison of cosmological hydrodynamics solutions, ApJ **525**, 554-582, (1999)

[27] Stone J. M., Gardiner T. A., ATHENA: A NEW CODE FOR ASTROPHYSICAL MHD, ApJ Supplement Series **178**: 137-177, (2008)

[28] Teyssier R., Cosmological hydrodynamics with adaptive mesh refinement. A new high resolution code called RAMSES, A&A **385**, 337-364, (2002)

[29] Bryan G. L., ENZO: AN ADAPTIVE MESH REFINEMENT CODE FOR ASTROPHYSICS, ApJ Supplement Series **211**: 19 (52pp), (2014)

[30] Wadsley J. W., Veeravalli G., Couchman H. M. P., On the treatment of entropy mixing in numerical cosmology, MNRAS **387**, 427-438, (2008)

[31] Price D. J., Modelling discontinuities and Kelvin-Helmholtz instabilities in SPH, astro-ph/0709.2772v3, (2008)

[32] Vogelsberger M., Marinacci F., Torrey P., Puchwein E., Cosmological simulations of galaxy formation, Technical Reviews, Vol. 2, (2020)

[33] Dolag K. et al., Simulation techniques for cosmological simulations, astro-ph/0801.1023v1, (2008)

[34] Barnes J., Hut P., A hierarchical O(N log N) force-calculation algorithm, Nature **324**, 446, (1986)

[35] Springel V., Yoshida N., White S. D. M., GADGET: A code for collisionless and gasdynamical cosmological simulations, New Astron. **6**, 79, (2001.b)

[36] Hideki Yahagi, Yuzuru Yoshii, N-Body Code with Adaptive Mesh Refinement, ApJ **558**, 463-475, (2001)

[37] Marinacci F., Dynamics of the halo gas in disc galaxies, Tesi di dottorato di ricerca in astronomia, (2011)

[38] Del Zanna et al., ECHO: a Eulerian conservative high-order scheme for general relativistic magnetohydrodynamics and magnetodynamics, Volume **473**, Number 1, (2007)

[39] Binney J., Tremaine S., Galactic Dynamics, 2nd edition, (2008)

[40] Trangenstein J. A., Numerical Solution of Hyperbolic Partial Differential Equations, Contemporary Physics, Volume **52**-Issue 6 (2011)

[41] Wadsley J. W. et al., Gasoline2: A Modern SPH Code, MNRAS **000**,1–15, (2017)

[42] Gingold R. A., Monaghan J. J., Smoothed particle hydrodynamics: theory and application to non-spherical stars.,MNRAS **181**,375-389, (1977)

[43] Springel V., Smoothed Particle Hydrodynamics in Astrophysics, Annu. Rev. Astron. Astrophys. **48**: 391–430, (2010)

[44] Monaghan J. J., Lattanzio J. C., A refined particle method for astrophysical problems , Astronomy and Astrophysics (ISSN 0004-6361), vol. **149**, (1985)

[45] Nelson R. P., Papaloizou J. C. B., VARIABLE SMOOTHING LENGTHS AND ENERGY CONSERVATION IN SMOOTHED PARTICLE HYDRODYNAMICS, MNRAS Vol. **270**, (1994)

[46] Price1 D. J., Monaghan J.J., An energy conserving formalism for adaptive gravitational force softening in SPH and N body codes, MNRAS **000**, 1-13, (2006)

[47] Monaghan J. J., SMOOTHED PARTICLE HYDRODYNAMICS, Annu. Rev. Astron. Astrophys. **30** : 543-74, (2005)

[48] Hopkins P. F., A new class of accurate, mesh-free hydrodynamic simulation methods, MNRAS **450**,53–110, (2015)

[49] Hopkins P. F., A general class of Lagrangian smoothed particle hydrodynamics methodsand implications for fluid mixing problems, MNRAS **428**,2840–2856, (2013)

[50] Cha S. H., Whitworth A.P., Implementations and tests of Godunov-type particle hydrodynamics, MNRAS **340**, 73-90, (2003)

[51] Ritchie B. W., Thomas P. A., Multiphase smoothed-particle hydrodynamics, MNRAS **323**, 743, (2001)

[52] Tittley E. R., Pearce F. R., Couchman H. M. P., Hydrodynamic drag in cosmological simulations, ApJ **561**, 69, (2001)

[53] Nelson D. et al., Moving mesh cosmology: tracing cosmological gas accretion, MNRAS **429**, 3353–3370, (2013)

[54] Vogelsberger M. et al., Moving mesh cosmology: numerical techniques and global statistics, MNRAS **425**, 3024–3057, (2012)

[55] Pais M. et al., The effect of cosmic ray acceleration on supernova blast wave dynamics, MNRAS **478**, 5278 (2018)

[56] Evrard A. E., Beyond N-body-3D cosmological gas dynamics, MNRAS **235**, 911, (1988)

[57] Bagla J. S., TreePM: A code for Cosmological N-Body Simulations, J. Astrophys. Astr. **23**, 1–14, (2002)

[58] Wadsley J. W., GASOLINE2: a modern smoothed particle hydrodynamics code, MNRAS **471**, 2357–2369, (2017)

[59] Weinberger R. et al., The Arepo public code release, ApJ: arXiv:1909.04667, (2019)

[60] Hernquist L., ANALYTICAL MODEL FOR SPHERICAL GALAXIES AND BULGES,ApJ **356**: 359-364, (1990)

[61] Frank J., Navarro C. S., White F., A UNIVERSAL DENSITY PROFILE FROM HIERARCHICAL CLUSTERING, ApJ **490**: 493-508, (1997)

[62] Boekholt T., Zwart S. P., On the Reliability of N-body Simulations, arXiv:1411.6671, (2014)

[63] Krumholz M. R., Tan J. C., SLOW STAR FORMATION IN DENSE GAS: EVIDENCE AND IMPLICATIONS, ApJ **654**, 304, (2007)

[64] Vogelsberger M. et al., A model for cosmological simulations of galaxy formation physics, MNRAS **436**, 3031–3067, (2013)

[65] Asplund M. et al., The Chemical Composition of the Sun, A&A, **47**, 481, (2009)

[66] Portinari L. et al., Galactic chemical enrichment with new metallicity dependent stellar yields, A&A **334**, 505, (1998)

[67] Thielemann F. K. et al., The physics of type Ia supernovae, MNRAS Volume **48**, Issues 7–8, (2004)

[68] Marinacci F. et al., The mode of gas accretion on to star-forming galaxies, MNRAS **404**, 1464, (2010)

[69] Leitner S. N., Kravtsov A. V., FUEL EFFICIENT GALAXIES: SUSTAINING STAR FORMATION WITH STELLAR MASS LOSS, APJ, **734**: 48 (13pp), (2011)

[70] Maoz D. et al., The delay-time distribution of Type Ia supernovae from Sloan II, MNRAS **426**, 3282–3294, (2012)

[71] Agertz O. et al., TOWARD A COMPLETE ACCOUNTING OF ENERGY AND MOMENTUM FROM STELLAR FEEDBACK IN GALAXY FORMATION SIMULATIONS, ApJ **770**: 25 (26pp), (2013)

[72] Li et al., Quantifying Supernovae-driven Multiphase Galactic Outflows, ApJ **841**, 101, (2017)

[73] Chevalier R. A. et al., The Evolution of Supernova Remnants. Spherically Symmetric Models, ApJ **188**, 501-516, (1974)

[74] McKee C. F., Ostriker J. P., A theory of the interstellar medium - Three components regulated by supernova explosions in an inhomogeneous substrate, ApJ **218**, 148-169, (1977)

[75] Hopkins P. et al., How to model supernovae in simulations of star and galaxy formation, MNRAS **477**, 1578, (2018b)

[76] Cioffi D. F. et al., Dynamics of radiative supernova remnants, ApJ **334**, 252, (1988)

[77] Hopkins F. P. et al., From the top down and back up again: star cluster structure from hierarchical star formation, MNRAS **480**, 800, (2018c)

[78] Piffl T. et al., The RAVE survey: the Galactic escape speed and the mass of the Milky Way, A&A **562**, A91, (2014)

[79] Collette A., Python and HDF5, Publisher(s): O'Reilly Media, Inc., (2013)

[80] VanderPlas J., Python Data Science Handbook, Publisher(s): O'Reilly Media, Inc., (2016)

[81] Tosi S., Matplotlib for Python Developers, Publisher: Packt Publishing, (2009)

[82] Cignoni et al., Recovering the star formation rate in the solar neighborhood, A&A **459**, 783–796, (2006)

[83] Twarog B. A., The chemical evolution of the solar neighborhood. II - The age-metallicity relation and the history of star formation in the galactic disk, ApJ **242**: 242-259, (1980)

[84] Vasiliev E. O., Launching of hot gas outflow by disc-wide supernova explosions, MNRAS Vol. **486**, Issue 3, (2019)

[85] Diehl R. et al., Radioactive ^{26}Al from massive stars in the Galaxy, Nature **439**, 45, (2006)

[86] Robitaille T. P., Whitney B. A., THE PRESENT-DAY STAR FORMATION RATE OF THE MILKY WAY DETERMINED FROM SPITZER-DETECTED YOUNG STELLAR OBJECTS, AJLs **710**: L11–L15, (2010)

[87] Marasco A. et al., HALOGAS: the properties of extraplanar HI in disc galaxies, A&A **631**, A50, (2019)

[88] Kennicutt R. C., THE GLOBAL SCHMIDT LAW IN STAR-FORMING GALAXIES, ApJ **498**: 541-552, (1998)

[89] Cioffi D. F. et al., Dynamics of Radiative Supernova Remnants, ApJ **334**, 252, (1988)

[90] Fraternali F., Binney F. F., A dynamical model for the extraplanar gas in spiral galaxies, MNRAS **449**, 449–466, (2006)

[91] Kannan R. et al., Efficacy of early stellar feedback in low gas surface density environments , MNRAS Vol. **491**, Issue 2, (2018)

[92] Nelson D. et al., Moving mesh cosmology: tracing cosmological gas accretion, MNRAS **429**, 3353–3370, (2013)

[93] Inoue A. K., Kamaya H., Intergalactic dust and its photoelectric heating, MNRAS **478**, 4 (2018)

[94] Ceverino D. et al., Gas inflow and metallicity drops in star-forming galaxies, MNRAS **457**, 2605–2612, (2016)

[95] Efstathiou G., A model of supernova feedback in galaxy formation, MNRAS **317**, 697-719, (2000)

[96] Oosterloo T. et al., THE COLD GASEOUS HALO OF NGC 891, ApJ **134**: 1019-1036, (2007)

[97] Wada K., Norman C. A., THE GLOBAL STRUCTURE AND EVOLUTION OF A SELF-GRAVITATING MULTIPHASE INTERSTELLAR MEDIUM IN A GALACTIC DISK, ApJ **515**: L13–L16, (1999)

[98] Kim C. G., Ostriker E. C., Numerical Simulations of Multiphase Winds and Fountains from Star-forming Galactic Disks. I. Solar Neighborhood TIGRESS Model, ApJ, **846**, 133, (2018)

[99] Agertz O. et al., Towards a complete accounting of energy and momentum from stellar feedback in galaxy formation simulations, ApJ **770**, 25 (2013)

[100] Springel V., Hernquist L., Cosmological smoothed particle hydrodynamics simulations: a hybridmultiphase model for star formation, MNRAS **339**, 289–311 (2003)